

IEET

International Electrical Engineering Transactions

Vol. 4 No. 1 (6)
January - June, 2018
ISSN 2465-4256



An online publication of the EEAAT
Electrical Engineering Academic Association (Thailand)
www.journal.eaat.or.th



IEET – International Electrical Engineering Transactions

This journal is an online publication of the EEAAT, Electrical Engineering Academic Association (Thailand). IEET is published twice a year, i.e., the first issue is for January – June and the second issue is for July – December.

EEAAT Journal Committee

Athikom Roeksabutr (Chairman)
Apirat Siritaratiwat
Kosin Chamnongthai
Prayoot Akkaraekthalin

IEET Editors

Somchai Hiranvarodom
Boonyang Plangklang

IEET (International Electrical Engineering Transactions) is published twice a year. Original contributions covering work in all aspects of electrical science, technology, engineering, and applications will be peer-reviewed by experts before publication. Topics of interest include the following: electrical power, electronics, telecommunication, control and system, sensor and measurement, optical technology, computer, information and communication technology (ICT), signal processing, social network tools and applications (apps), engineering education and other related fields.

For online submission of all manuscripts, correspondences, and letters, please visit
www.journal.eeaat.or.th

IEET Editorial Office

EEAAT - Electrical Engineering Academic Association (Thailand)
Room 409, F-Building, 140 Cheum-Sampan Rd.
Nong Chok, Bangkok, Thailand 10530
Tel: +662-988-3655 ext 2216 Fax: +662-988-4026

PAPERS

Condition Evaluation for Step-Up Power Transformer in Power Plant Using Electrical Test Data	Songbun Naksuwan Thanapong Suwanasri Suphon Kumpalavalee Cattareya Suwanasri	1
Development of Measurement System using Various Spectroscopic Methods for Integration into 3D Laser Scanner Projector	Ryohei Niwase Keisuke Fukuda	7
Investigation of Hot Air Production from Fluidized Bed Kiln with Biomass of Rice Husk	Winai Chanpeng Phairoach Chunkaew	10
Collection of Variable Datas Affected Electricity Generation of PV – Array with FIO Board STM 32F4	Akeratana Noppakant Jirasak Songboonkaew	14
Optimal Mixture Experiment Design Using Neural Network	Dussadee Buntam Wachirapond Permpoonsinsup Prayoon Surin	19
Single-carrier-based Pulsewidth Modulation Strategy for Grid-connected Three-level NPC Converter Based on Voltage-oriented Control	Watcharin Srirattanawichaikul Suttichai Premrudeepreechacharn Yuttana Kumsuwan	24
Design and Analysis of a Single-Phase Hybrid Renewable Energy System	Jirasak Songboonkaew Akeratana Noppakant	31
Illumination Control System by LDR for Energy Efficient Buildings	SAKRAEE RAWEEKUL	36
A Study on Conductor Loss Measurement of Microstrip Line	Yusuke Kusama Yusuke Yokoi Robert Weston Johnston	40
Convergence Analysis of Adaptive Reduced-Rank Affine Projection Algorithm	Suchada Sitjongsataporn	47
High Voltage - Pulse Electric Field of Microorganism Elimination	Sanya khunkhao Aphichata Thongrak Wanchai Chankaipol	54

Condition Evaluation for Step-Up Power Transformer in Power Plant Using Electrical Test Data

Songbun Naksuwan, Thanapong Suwanasri
and Suphon Kumpalavalee

Electrical and Software System Engineering, The Sirindhorn
International Thai-German Graduate School of Engineering
King Mongkut's University of Technology North Bangkok
1518 Pracharat 1 Rd., Bangsue, Bangkok, Thailand
songbun.naksuwan@gmail.com, thanapongs@kmutnb.ac.th

Cattareya Suwanasri
Electrical and Computer Engineering,
Faculty of Engineering

King Mongkut's University of Technology North Bangkok
1518 Pracharat 1 Rd., Bangsue, Bangkok, Thailand
cattareya.s@eng.kmutnb.ac.th

Abstract—This paper proposes a method for condition evaluation for step-up power transformer in power plant using electrical test data and visual inspection for general condition. The transformer components consist of winding, magnetic core, insulating oil in main tank, insulating oil in on-load tap changer, bushing, and surge arrester. The conditions of these transformer components have been evaluated by using the scoring and weighting technique to obtain the health indices of these components. Subsequently, these known component health indices are used to calculate the overall health index of power transformer. This developed method is further developed by using the dynamic programming to obtain a web application software tool. This software can facilitate previous complex and costly preventive maintenance to condition-based maintenance.

Keywords— electrical test; power transformer; condition evaluation, power plant

I. INTRODUCTION

In the supply network, power transformer is a core equipment in electrical power system as it plays important role in transmitting and distributing power to load. Unfortunately, power transformer is an expensive equipment. Failure of power transformer because of aging and degradation [1] as well as abnormal operating condition could lead to a wide damage area, long interrupting time and huge impact to system reliability. Moreover, number of power transformer and maintenance data are non-systematic disrupted. Therefore, asset management focusing on power transformer maintenance is necessary [2]. The problem is that a large number of power transformer data are scattering and difficult to collect into centralize data for effective management because some data are in paper-based and manual collecting. Thus, it is difficult to obtain transformer information, record, edit or update any data as well as testing results during maintenance. Moreover, the method to determine conditions of power transformers as "Health Index" is not applied in order to perform the proper maintenance with power transformer in generating plant, which has been operated under large and continuous load current. Therefore, this paper present a method for condition evaluation for step-up power transformer in power plant using electrical test data and visual inspection for general condition. The

process starts from gathering the power transformers data to one organized centralized database of both technical data and maintenance data. Then, the analysis part is implemented using IT support as development of dynamic web application software to support the condition-based maintenance.

II. DATA STRUCTURE OF POWER TRANSFORMER

In order to evaluate the condition of power transformer, it is imperative to classify the major components. The components of power transformer can be seen in Fig. 1. The major component of power transformer can be classified into six components consisting of winding, bushing, magnetic core, main tank, on load tap changer (OLTC) and surge arrester.

Next, each component would be evaluated the condition by analyzing the electrical testing results such as insulation resistance and PI test, power factor (PF) test, turn ratio test, winding resistance test, single phase impedance test, three phase impedance test, excitation current test, core insulation test and visual inspection. Lastly, the evaluated condition of each components will be combined together to be overall health index of power transformer.

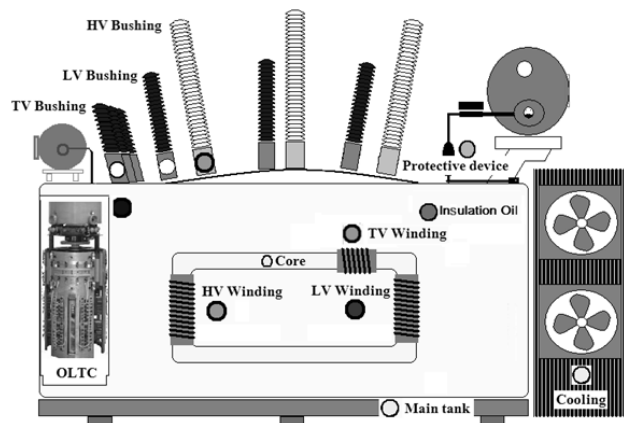


Fig. 1. Power transformer components

A. Maintenance and Electrical Tests Data

Normally, the measurement for electrical tests data [3] are tested when the power transformer are de-energized or off-line for complete test and diagnosis. For winding, the performed tested are insulation resistance and PI test, power factor (PF) test, turn ratio test, winding resistance test, single phase test, three phase test and excitation current test. For bushing, main tank, OLTC and surge arrester, the performed tested are power factor (PF) test and visual inspection. For magnetic core, the performed testing is core insulation resistance test.

III. DATABASE OF ELECTRICAL TEST OF POWER TRANSFORMER

For power transformer asset management, the information technology should be integrated with electrical power engineering knowledge for improving efficiency in electrical asset management. Thus, dynamic programing and web application play important role in this work to assemble database installation, data dispensation, user interface, analyzing data for condition evaluation, and result display. Database is an integration of electrical test data from each component of power transformer into central database. Client can operate the database by web application on browser. Dynamic programing could make it easy to add, edit, select or delete the required data from the database. Nowadays, language codes for website programing are diverse such as PHP, HTML, JAVA Script and etc. In this paper, PHP language is selected to develop a website for power transformer condition with MySQL as database program because of the open source software and easy for self-learning of the program developer. The developed web application can be used via web browser on computer or mobile web browser. Therefore, client can access the database by use internet from anywhere and anytime as shown in Fig. 2.

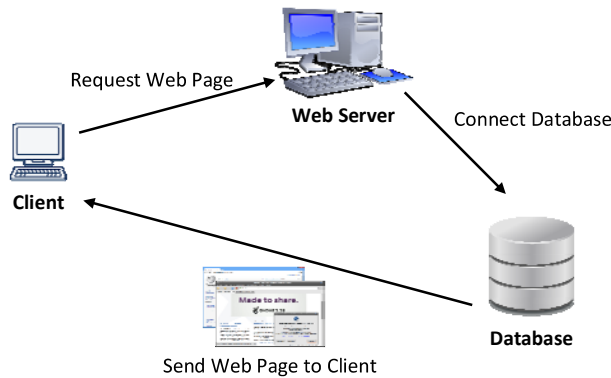


Fig. 2. Dynamic programing and web application for database management and power transformer assessment.

IV. COMPONENT TESTING AND EVALUATION CRITERIA

The inspection methods for condition assessment of power transformer consist of insulation resistance test and PI test, power factor (PF) test, turn ratio test, winding resistance test, single phase impedance test, three phase impedance test,

excitation current test, core insulation test, and visual inspection. The details of each testing and condition criteria are explained in this section. For condition and its scoring, the condition of each test can be categorized in to three conditions including “good” scored as “5”, “acceptable” scored as “3” and “poor” scored as “1”, but except visual inspection that has only “good” scored as “5” and “poor” scored as “0” score.

A. Insulation Resistance and PI Test

For insulation resistance and PI test, they can be categorized to three testing methods including core insulation test, insulation resistance test, and polarization index (PI) test. The insulation resistance and PI test are used for detecting the condition of power transformer insulation. For the core insulation test, it is performed by measuring the resistance between magnetic core inside power transformer and ground. For the PI test, the tests is performed on high voltage (HV) winding, low voltage (LV) winding and tertiary voltage (TV) winding. The PI is calculated by comparing the measured resistance at minute 10 ($R_{10Min.}$) to resistance at minute 1 ($R_{1Min.}$) by using Eq. (1). The example on testing results for PI calculation is shown in Table I. However, for insulation resistance test, it is performed by measuring only $R_{1Min.}$. The assessment criteria for insulation resistance and PI test are shown in Table II. Some of power transformers have no tertiary voltage winding so that the PI of TV winding is zero.

$$PI = \frac{R_{10Min.}}{R_{1Min.}} \tag{1}$$

TABLE I. POLARIZATION INDEX (PI) TEST ON TRANSFORMER WINDING

Insulation	$R_{1 Min.} (M\Omega)$	$R_{10 Min.} (M\Omega)$	PI
HV	1010	3150	3.12
LV	990	2850	2.88
TV	0	0	0

TABLE II. CRITERIA FOR INSULATION RESISTANCE AND PI TESTS

Criteria	Score			Weight (w_i)
	Good =5	Acceptable =3	Poor =1	
Core Insulation (MΩ)	> 100	10-100	< 10	5
$R_{1 Min.} (M\Omega)$	> 1000	-	< 1000	5
PI	> 2	1-2	< 1	3

B. Power Factor (PF) Test

Power factor test is aimed to check the integrity of insulation and watt loss in each component. Power factor test can be performed with 5 components including HV winding, LV winding, bushing, surge arrester and insulation oil (main tank and OLTC). In this test, there are three measurements such as PF ($\tan\delta$) test, capacitance measurement and watt loss measurement (for surge arrester only).

The example of power factor testing results of 5 transformer components are shown in Table III. For the capacitance measurement, the evaluation is to compare the

measured value with the commissioning value defined as percent deviation from commissioning ($\%DEV_{cap}$), which can be calculated by Eq. (2).

The examples on capacitance test and $\%DEV_{cap}$ calculation are given in Table IV. The example on watt loss test and leakage current test of surge arrester are shown in Table V. The assessment criteria of power factor test are shown in Table VI.

$$\%DEV_{cap} = \frac{|C_{Test} - C_{Factory}|}{C_{Factory}} \times 100 \quad (2)$$

where C_{Test} is capacitance from testing result (pF) and $C_{Factory}$ is capacitance from factory test (pF).

TABLE III. % PF TESTED ON HV, LV AND OTHER COMPONENTS

Component	% PF (tanδ)		
	$C_{HL}+C_H$	C_{HL}	C_H
HV at 10kV	0.139	0.108	0.264
LV at 5kV	$C_{LH}+C_L$	C_{LH}	C_L
	0.177	0.098	0.249
Bushing at 10kV	Phase A	Phase B	Phase C
	0.24	0.228	0.246
Surge Arrester at 10kV	Phase A	Phase B	Phase C
	0.147	0.129	0.121
Insulation Oil	Main Tank	OLTC	
	0.07	0.06	

TABLE IV. CAPACITANCE TEST AND $\%DEV_{cap}$ CALCULATION

Component	Capacitance (pF)					
	$C_{HL}+C_H$		C_{HL}		C_H	
HV	$C_{Factory}$	C_{Test}	$C_{Factory}$	C_{Test}	$C_{Factory}$	C_{Test}
		14800	14650	11740	11660	3058
$\%DEV_{Cap}$	1.013		0.681		2.224	
LV	$C_{LH}+C_L$		C_{LH}		C_L	
	$C_{Factory}$	C_{Test}	$C_{Factory}$	C_{Test}	$C_{Factory}$	C_{Test}
	24370	24370	15706	11680	12644	12690
$\%DEV_{Cap}$	0		25.633		0.364	
Bushing	Phase A		Phase B		Phase C	
	$C_{Factory}$	C_{Test}	$C_{Factory}$	C_{Test}	$C_{Factory}$	C_{Test}
	587.5	575.86	590.5	577.59	593.8	579.4
$\%DEV_{Cap}$	1.981		2.186		2.425	
Surge Arrester	Phase A		Phase B		Phase C	
	$C_{Factory}$	C_{Test}	$C_{Factory}$	C_{Test}	$C_{Factory}$	C_{Test}
	45.36	47.24	43.89	41.42	42.61	38.85
$\%DEV_{Cap}$	4.144		5.627		8.824	
Insulation Oil	Main Tank			OLTC		
	$C_{Factory}$	C_{Test}	$C_{Factory}$	C_{Test}	$C_{Factory}$	C_{Test}
	146.987	139.660	144.582	138.505		
$\%DEV_{Cap}$	4.984			4.203		

TABLE V. WATT LOSS AND LEAKAGE CURRENT TEST ON SURGE ARRESTER AT 10 KV

Surge Arrester	Phase A	Phase B	Phase C
Watt loss (mWatt)	59	61	61
Leakage Current (mA)	5.979	5.979	4.354

TABLE VI. CRITERIA FOR POWER FACTOR TEST

Criteria	Score			Weight (w_i)
	Good =5	Acceptable =3	Poor =1	
% PF (tanδ)	< 0.5	0.5-1	> 1	4
% PF (tanδ) for insulating oil	< 0.5	-	> 0.5	2
Watt loss (mWatt)	< 150	-	> 150	2
$\%DEV_{Cap}$	< 10%	10%-20%	> 20%	3

C. Turn Ratio Test

Turn ratio test is used to evaluate power transformer winding that might be short turn or open winding circuit due to corrupt insulation or deform of winding. Rated turn ratio ($Ratio_{rated}$) and percentage deviation of turn ratio ($\%DEV_{ratio}$) can be calculate by Eq. (3) and Eq. (4)

$$Ratio_{rated} = \frac{V_{pri,rated}}{V_{sec,rated} \sqrt{3}} \quad (3)$$

$$\%DEV_{ratio} = \frac{|Ratio_{rated} - Ratio_{phase}|}{Ratio_{rated}} \times 100 \quad (4)$$

where $V_{pri,rated}$ is rated primary voltage (V), $V_{sec,rated}$ is rated secondary voltage (V) and $Ratio_{phase}$ is individual phase turn ratio.

The examples for calculating $Ratio_{rated}$ and $\%DEV_{ratio}$ are shown in Table VII and Table VIII. The assessment criterion for evaluating the condition of transformer winding from the turn ratio test is shown in Table IX.

TABLE VII. $Ratio_{rated}$ CALCULATION

Tap	Voltage		$Ratio_{rated}$
	HV	LV	
Max	129105	11000	6.780
Center	123000	11000	6.460
Min	116850	11000	6.130
No.1	126366	11000	6.632
No.2	120183	11000	6.308

TABLE VIII. $\%DEV_{ratio}$ CALCULATION

Tap	Ratio _{rated}	Phase A		Phase B		Phase C	
		Ratio _{phase}	$\%DEV_{ratio}$	Ratio _{phase}	$\%DEV_{ratio}$	Ratio _{phase}	$\%DEV_{ratio}$
Max	6.780	6.797	0.26	6.791	0.17	6.794	0.21
Center	6.460	6.471	0.17	6.467	0.12	6.467	0.11
Min	6.130	6.146	0.26	6.141	0.19	6.142	0.19
No.1	6.632	6.633	0.02	6.632	0.00	6.630	0.04
No.2	6.308	6.308	0.01	6.303	0.07	6.304	0.05

TABLE IX. CRITERION FOR TURN RATIO TEST

Criterion	Score			Weight (w_i)
	Good =5	Acceptable =3	Poor =1	
$\%DEV_{ratio}$	< 0.1	0.1-0.5	> 0.5	5

D. Winding Resistance Test

Winding resistance test is used to check the loosen connections, broken strands and high contact resistance in the tap changers. The equation for conversion the measured resistance (in case of resistance measurement not measure at reference temperature) is given in Eq. (5), where T_s is desired reference temperature ($^{\circ}\text{C}$), T_k is temperature, at which the winding resistance was measured ($^{\circ}\text{C}$), T_m is copper's temperature (234.5°C) or aluminum's temperature (225°C) R_m is the measured resistance (Ω) and R_s is the resistance at desired reference temperature (Ω). The equation for calculating percentage deviation of winding resistance ($\%DEV_{wr}$) is given Eq. (6), where R_{max} is the maximum R_s of considered tap (Ω) and R_{min} is the minimum R_s of considered tap (Ω).

For example, the resistance measurement results of HV and LV windings at reference temperature are shown in Table X. Subsequently, all the calculated results as percent deviation of winding resistance of each phase or $\%DEV_{wr}$ are shown in Table XI. The assessment criterion for winding resistance test is presented in Table XII.

$$R_s = R_m \frac{T_s + T_k}{T_m + T_k} \quad (5)$$

$$\%DEV_{wr} = \frac{|R_{max} - R_{min}|}{R_{min}} \times 100 \quad (6)$$

TABLE X. R_s AT REFERENCE TEMPERATURE (20°C)

Winding		R_s (Ω)				
		Tap Max	Tap Center	Tap Min	Tap No.1	Tap No.2
HV	H1-H0	0.2865	0.2470	0.2890	0.2518	0.2420
	H2-H0	0.2879	0.2499	0.2883	0.2544	0.2446
	H3-H0	0.2863	0.2469	0.2875	0.2518	0.2420
LV	X1-X0	0.2001				
	X2-X0			0.2004		
	X3-X0					0.1999

TABLE XI. $\%DEV_{wr}$ OF WINDING RESISTANCE TEST

$\%DEV_{wr}$	Tap Max	Tap Center	Tap Min	Tap No.1	Tap No.2
HV	0.56	1.22	0.53	1.01	1.09
LV			0.3		

TABLE XII. CRITERION FOR WINDING RESISTANCE TEST

Criterion	Score			Weight (w_i)
	Good =5	Acceptable =3	Poor =1	
$\%DEV_{wr}$	< 1%	1%-5%	> 5%	5

E. Single Phase Impedance Test

Single phase impedance or leakage impedance test is used to detect winding movement or deformation due to short circuit current or mechanical forces during installation or transportation. The equation for calculating the percentage of deviation of leakage impedance ($\%DEV_{\phi}$) is Eq. (7). Where

$R_{\phi max}$ and $R_{\phi min}$ are the maximum and minimum leakage impedance of considered tap (Ω), respectively. The example of single phase impedance test is shown in Table XIII. The criterion of single phase impedance test is shown in Table XIV.

$$\%DEV_{\phi} = \frac{|R_{\phi max} - R_{\phi min}|}{R_{\phi min}} \times 100 \quad (7)$$

TABLE XIII. $\%DEV_{\phi}$ OF SINGLE PHASE IMPEDANCE TEST

Phase	$R_{winding}$ (Ω)				
	Tap Max	Tap Center	Tap Min	Tap No.1	Tap No.2
Phase A	51.45	43.38	34.35	44.45	42.17
Phase B	51.83	43.77	34.79	44.69	42.87
Phase C	51.2	43.2	34.13	44.3	42.32
$\%DEV_{\phi}$	1.230%	1.319%	1.933%	0.880%	1.659%

TABLE XIV. CRITERION FOR SINGLE PHASE IMPEDANCE TEST

Criterion	Score			Weight (w_i)
	Good =5	Acceptable =3	Poor =1	
$\%DEV_{\phi}$	< 0.5%	0.5%-3%	> 3%	3

F. Three Phase Impedance Test

Three phase impedance or short circuit impedance test is used to detect winding movement that may occur due to fault current or mechanical force during transportation. The equation for calculating the percentage short circuit impedance ($\%Z_{cal}$) and percentage deviation of short circuit impedance ($\%DEV_{sc}$) are Eq. (8) and Eq. (9), respectively.

$$\%Z_{cal} = \frac{(\sum Z_{sc}) \times P}{60V_{Tap}^2} \quad (8)$$

$$\%DEV_{sc} = \frac{|Z_{NP} - Z_{cal}|}{Z_{NP}} \times 100 \quad (9)$$

where $\sum Z_{sc}$ is summation of measured short circuit impedance of considered tap (Ω), P is rated power (VA), V_{Tap} is tap voltage (V), Z_{NP} is percentage of short circuit impedance from factory test in nameplate. The examples of three phase impedance testing results are shown in Table XV. The calculations of Z_{cal} and $\%DEV_{sc}$ are shown in Table XVI. The assessment criterion of three phase impedance test is shown in Table XVII.

TABLE XV. THREE PHASE IMPEDANCE TEST OF 50 MVA POWER TRANSFORMER FOR Z_{sc} CALCULATION

Tap	Winding H1-H2			Winding H2-H3			Winding H3-H1		
	V	I	Z_{sc}	V	I	Z_{sc}	V	I	Z_{sc}
Max	166.7	2.005	83.142	165.1	2.007	82.262	165.5	2.004	82.585
Center	130.8	2.000	65.400	130.1	2.009	64.759	129.6	2.000	64.800
Min	102.7	2.003	51.273	101.9	2.003	50.873	102.0	2.001	50.975

TABLE XVI. Z_{cal} AND $\%DEV_{sc}$ CALCULATION

Tap	Tap Voltage (kV)	Nameplate	Calculation (Z_{cal})	$\%DEV_{sc}$
Max	126.5	12.98	12.91	0.539
Center	115	12.35	12.28	0.566
Min	103.5	12.08	11.91	1.407

TABLE XVII. CRITERION FOR THREE PHASE IMPEDANCE

Criterion	Score			Weight (w_i)
	Good =5	Acceptable =3	Poor =1	
$\%DEV_{sc}$	< 3%	-	> 3%	2

G. Excitation Current Test

Excitation current test is used to locating defects in the magnetic core structure, winding shifting, turn-to-turn insulation failure or problem within the tap changer. The equation for calculating percentage deviation of excitation current ($\%DEV_{ext}$) is Eq. (10) where I_{com} is commissioning current from factory test (mA) and I_{ϕ} is the measured phase current (mA). The example of excitation current test is shown in Table XVIII. The calculation of $\%DEV_{ext}$ is shown in Table XIX. The criterion of excitation current test is shown in Table XX.

$$\%DEV_{ext} = \frac{|I_{com} - I_{\phi}|}{I_{com}} \times 100 \quad (10)$$

TABLE XVIII. I_{ϕ} FROM EXCITATION CURRENT TEST

Phase	Tap Max	Tap Center	Tap Min
H1-H2 (Phase A)	2.02	2.359	3.103
H2-H3 (Phase B)	1.677	1.972	2.539
H1-H2 (Phase A)	2.072	2.417	3.198

TABLE XIX. $\%DEV_{ext}$ CALCULATION

Phase	Tap Max	Tap Center	Tap Min	
A	I_{com} (mA)	2.1	2.6	3.12
	I_{ϕ} (mA)	2.020	2.359	3.103
	$\% DEV_{ext}$	3.809	9.269	0.545
B	I_{com} (mA)	1.69	1.9	2.49
	I_{ϕ} (mA)	1.677	1.972	2.539
	$\% DEV_{ext}$	0.769	3.789	1.968
C	I_{com} (mA)	2.06	2.41	3.23
	I_{ϕ} (mA)	2.072	2.417	3.198
	$\% DEV_{ext}$	0.583	0.291	0.991

TABLE XX. CRITERION FOR EXCITATION CURRENT TEST

Criterion	Score			Weight (w_i)
	Good =5	Acceptable =3	Poor =1	
$\%DEV_{ext}$	< 1%	1%-10%	> 10%	3

H. Visual Inspection

Visual inspection is an initial diagnosis to check the general condition of power transformer components by sense

of human or simple tool. The criteria for visual inspection are shown in Table XXI.

TABLE XXI. CRITERIA FOR VISUAL INSPECTION

No.	Inspection check list	Score		Weight (w_i)
		Good	Poor	
1	Porcelain condition	Normal	Abnormal	5
2	Oil leakage	Normal	Abnormal	5
3	Oil level	Normal	Abnormal	5
4	Oil and winding Temp	Normal	Abnormal	5
5	Self-protection	Normal	Abnormal	5
6	Surface painting	Normal	Abnormal	5
7	Foundation, earthing	Normal	Abnormal	5
8	Dehydrating breather	Normal	Abnormal	5
9	Terminal box	Normal	Abnormal	5
10	Bolt and nut connection	Normal	Abnormal	5
11	On load tap changer	Normal	Abnormal	5

V. HEALTH INDEX EVALUATION

The method to determine health index of power transformer using scoring and weighting technique [4], [5] is shown in fig. 3. The health index can be separated for each major components. The health index is determined from electrical testing results by using weighing and scoring techniques as well as Analytical Hierarchy Process (AHP). Then, the components' health indices ($\%HI_{component}$) are used to determine overall health index ($\%HI_{TR}$) of power transformer.

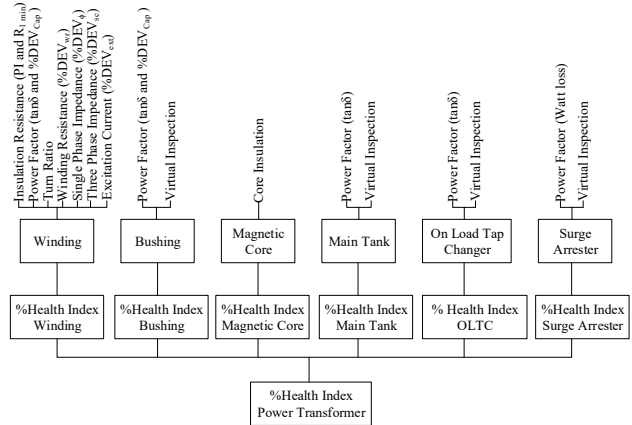


Fig. 3. Health index calculation diagram of power transformer.

TABLE XXII. HEALTH INDEX WEIGHT OF COMPONENTS

Component	$\%HI_{component}$	$\%Weight (\%w_i)$	$\%HI_{TR}$
Winding	$\%HI_{Winding}$	30%	100%
Bushing	$\%HI_{Bushing}$	20%	
Magnetic core	$\%HI_{Magnetic Core}$	20%	
Main tank	$\%HI_{Main Tank}$	10%	
OLTC	$\%HI_{OLTC}$	10%	
Surge Arrester	$\%HI_{Surge Arrester}$	10%	

The percentage weight of health index of each component can be divided as shown in Table XXII. The equation to calculate percentage health index of each component ($\%HI_{component}$) and percentage health index of overall power transformer ($\%HI_{TR}$) is Eq. (11) and Eq. (12), respectively. Where s_i is score of the test method, w_i is weight of test method, s_{max} is maximum score of each test method of each component. $\%w_j$ is percentage weight of each component. n is number of testing methods of each component while m is number of components.

$$\%HI_{component} = \frac{\sum_{i=1}^n (s_i \times w_i)}{s_{max} \times \sum_{i=1}^n w_i} \times 100 \quad (11)$$

$$\%HI_{TR} = \sum_{j=1}^m \frac{\%HI_{component,j} \times \%w_j}{100} \quad (12)$$

$\%HI_{component}$ and $\%HI_{TR}$ of power transformer of six power transformers are shown in Table XXIII. The $\%HI_{component}$ of each component is calculated from different electrical testing methods for different component by using Eq. (11) while the $\%HI_{TR}$ can be determined by using Eq. (12). The condition setting in conditional color band of transformer for showing overall health index as given in Table XXIV. The power transformers having worst overall health index are TR1 and TR4, respectively. For TR4, it has the worst health index (74.77%) due to high winding resistance ($\%DEV_{wr} = 6.7\%$) and high power factor on bushing ($\tan \delta = 1.16$). For TR1, it has the second worst health index (78.46%) due to poor power factor ($\tan \delta = 1.30$) on bushing and due to oil leakage (abnormal oil leakage) in main tank and low oil level.

TABLE XXIII. HEALTH INDEX OF EACH COMPONENT AND AN OVERALL HEALTH INDEX OF POWER TRANSFORMER

Power Transformer	TR1	TR2	TR3	TR4	TR5	TR6
$\%HI_{Winding}$	84.36%	72.51%	83.42%	64.22%	93.82%	80.22%
$\%HI_{Bushing}$	41.00%	88.00%	88.00%	45.00%	100.00%	82.00%
$\%HI_{Magnetic Core}$	100.00%	100.00%	60.00%	100.00%	100.00%	100.00%
$\%HI_{Main Tank}$	57.00%	95.00%	85.00%	85.00%	95.00%	85.00%
$\%HI_{OLTC}$	92.50%	92.50%	100.00%	100.00%	100.00%	92.50%
$\%HI_{Surge Arrester}$	100.00%	100.00%	100.00%	80.00%	100.00%	100.00%
$\%HI_{TR}$	78.46%	88.10%	83.13%	74.77%	97.65%	88.23%

TABLE XXIV. CONDITION FOR POWER TRANSFORMER OVERALL HEALTH INDEX

$\%HI_{TR}$	Condition
95%-100%	Good
80%-94%	Acceptable
< 80%	Poor

VI. CONCLUSION

The technical data and electrical test data during off-line major inspection of power transformer in generating power station have been systematically recorded into the central database. The electrical test consists of insulation resistance test, power factor test, turn ratio test, winding resistance test, single phase impedance test, three phase impedance test and excitation current test. The electrical test together with visual inspection have been analyzed by using scoring and weighting technique to calculate the health index of power transformer components such as winding, bushing, magnetic core, insulating oil in main tank, insulating oil in on-load tap changer and surge arrester. The known health index of each component is used further to calculate the overall health index of power transformer. With this overall health index, the proper maintenance can be setup according to the actual condition.

REFERENCES

- [1] Muhr M., "Aging and degradation, their detection and monitoring and asset management", International Symposium on Electrical Insulating Material, 2008
- [2] Balzer G., et al., "Strategies for Optimizing the Use of Substation Assets" Cigre Session B3-01, 2004
- [3] IEEE-Std 62-1995. "IEEE Guide for Diagnostic Field Testing of Electric Power Apparatus-Part 1: Oil Filled Power Transformers, Regulators, and Reactors", 2005.
- [4] Brian Sparling, Jacques Aubin, "Determination of Health Index for Aging Transformer in View of Substation Asset Optimization", Proceedings of the 2010 International Conference on Condition Monitoring and Diagnostic, Japan.
- [5] Naderain A., Cress S., Piercy R., Wang F., Service J., "An Approach to Determine the Health Index of Power Transformers", IEEE International Symposium on Electrical Insulation, 2008

Development of Measurement System using Various Spectroscopic Methods for Integration into 3D Laser Scanner Projector

Ryohei Niwase, Keisuke Fukuda

Advanced Course in Industrial and Systems Engineering
National Institute of Technology, Kagawa College, NITKC
Takamatsu, JAPAN

Nobuhiro Tsumori

Department of Electro-Mechanical Systems Engineering
National Institute of Technology, Kagawa College, NITKC
Takamatsu, JAPAN
E-mail: n.tsumori@t.kagawa-nct.ac.jp

Abstract— We propose integrating various spectroscopic methods and components into conventional 3D laser scanner as a measurement system of 3D surface construction and substance identification. The system enables real-time simultaneous detection, analysis and visualization of invisible pollutants on the surface of objects. To realize this system, dedicated spectrometer and circuits were designed, implemented and evaluated. As results of evaluation, we confirmed the spectrometer and circuits were functional and suitable for the system.

Keywords— Substance identification, Spectroscopy, LIDAR, FPGA

I. INTRODUCTION

For substance identification in environmental monitoring, various spectroscopic methods using laser light (e.g. photoluminescence spectroscopy, Raman scattering spectroscopy, fluorescence correlation spectroscopy and absorption spectroscopy) had been developed and widely used. We propose integrating these spectroscopic methods into conventional 3D laser scanner like a LIDAR (laser imaging detection and ranging) [1-4]. This proposed system is specialized for short-range, real-time and simultaneous measurement of 3D surface construction and substance identification. It is supposed to be portable and to be used in the range of less than 10 m. Measurement results can be projected onto the measurement field by laser scanning. By using this system, invisible pollutants on the surface of objects can be detected, analyzed and visualized by real-time.

In this paper, we designed and implemented a spectrometer and circuits toward integration into 3D laser scanner. Also, we evaluated the performance of the spectrometer and circuits by fluorescent measurement. These spectrometer and circuits can be used for another equipment [5].

II. DEDICATED SPECTROMETER

For real-time and simultaneous measurement, optical components of a dedicated spectrometer were specifically designed shown in Fig. 1 and implemented shown in Fig. 2. Optical components including convex lens and concave mirror were used for converging and collimating incident light. A pinhole was used as a spatial filter. For wavelength dispersion,

reflective ruled diffraction grating (600 grooves/mm, blaze angle of $8^{\circ} 37'$, dimensions of 12.7 mm x 12.7 mm) was embedded. As optical detector, charge-coupled device (CCD) image sensor (Toshiba TCD2953CF) was embedded. Wavelength range of the spectrometer is 400 nm to 1000 nm. Circuits of CCD clock buffer and analog-front-end for CCD signal were implemented close to the CCD. These components were specifically designed for integrating to 3D laser scanner.

III. CIRCUITS ON FPGA

A. FPGA board

Any electric circuits for measurements including data processing were implemented on field-programmable gate array (FPGA). FPGA is a kind of gate-array IC which enables implementation of reconstructable digital-circuits. By using FPGA, it is possible to attain high-speed measurement by sequential processing and additional configuration of control-circuits of the 3D laser scanner and the other equipment. As FPGA board for the implementation, we used Altera MAX10 Development Kit (Rev. C) having 10M50DAF484C6GES (Logic Element: 50 k, M9K Memory: 1,638kbit).

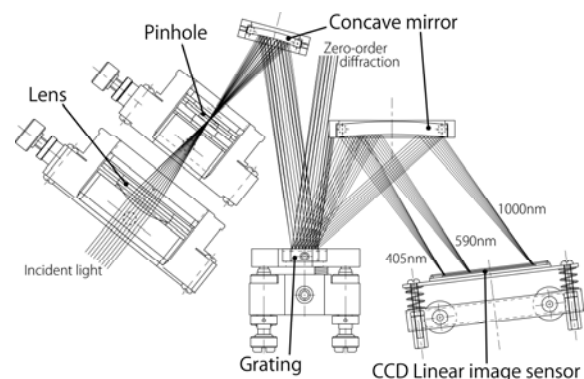


Fig. 1. Design of the spectrometer



Fig. 2. Implemented spectrometer

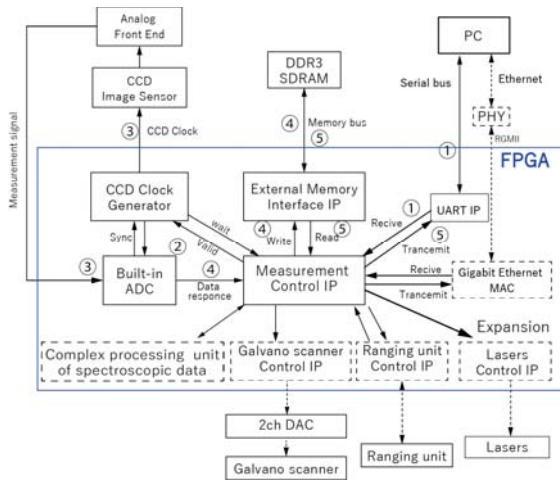


Fig. 3. Operation transition of measuring circuits

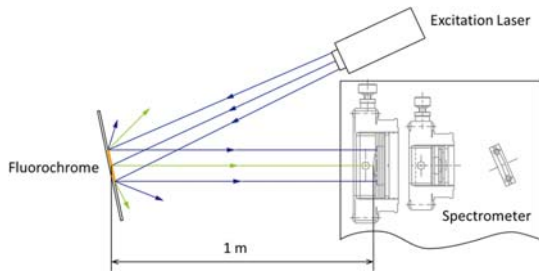


Fig. 4. Set-up of evaluation measurement

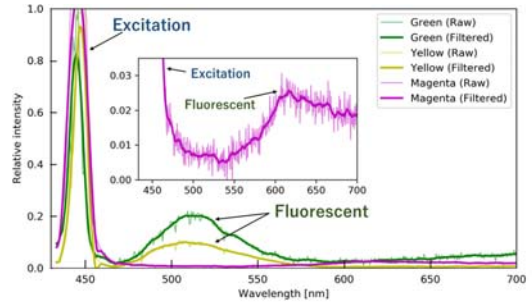


Fig. 5. Obtained spectra of fluorescent

TABLE 1. Capacity of number of logical cells of the FPGA board

Circuits	Number of logical cells	Use rate [%]
Measurement Control IP	392	0.788
CCD Clock Generator	67	0.135
Built-in ADC control IP	123	0.245
External Memory Interface IP	6277	12.6
UART IP	192	0.389
Total used cells	7051	14.2
Unused cells	42709	85.8
All cells	79760	100

B. Operation transition of measuring circuits

Operation transition of implemented measuring circuits were shown in Fig. 3. At first, measurement control intellectual property core (IP) receive the start-control signal from the computer via serial bus or ethernet. Then measurement control IP enables CCD clock generation circuit and analog to digital (A/D) converter. Every time the clock changes, the analog shift register inside the image sensor is shifted, and analog signals for each pixel are sequentially output. The signal data converted for each pixel by the A/D converter is sequentially written to the external memory. After completing all measurements, measurement data is send to the computer while reading the measurement data from the beginning of the external memory through external memory IP.

IV. EVALUATION

A. Measurement of fluorescent spectra

The spectrometer and circuits were evaluated by measurement of four fluoresent spectra which were from three kinds of fluorochrome (green, yellow, magenta) induced by laser light having wavelength of 450 nm with experimental set-up shown in Fig. 4. Any fluoresent light was detected by CCD through the spectrometer from the distance of 1 m. As results, appropriate spectra shown in Fig. 5 were obtained by the dedicated spectrometer and the circuits on the FPGA board. We confirm that the circuits on the FPGA board controlled the CCD and processed sequentially the spectroscopic data.

B. Capacity of the FPGA board

Table 1 shows sufficient capacity of the FPGA board to implement other circuits for controlling other equipment including 3D laser scanner and for complex processing of spectroscopic data surrounded by dashed line in Fig. 3.

V. CONCLUSION

We developed a spectroscopic measurement system for integration into 3D laser scanner. A dedicated spectrometer and measurement circuits on FPGA were implemented. As results of evaluation, functionality of the system was confirmed.

REFERENCES

- [1] T. Tomida, N. Nishizawa, K. Sakurai, H. Sukanumata, S. Tsukada, S. M. Song, H. D. Park and Y. Saito, "Performance Characteristics of Compact Mobile LIFS (Laser-Induced Fluorescence Spectrum) Lidar," EPJ Web of Conferences, vol. 119, 2016, pp.17009-17012.
- [2] T. Tomida, N. Nishizawa, T. Fujii, and Y. Saito, "Automotive LIFS LIDAR for Substance identification and 3D spatial observation," Proc. 33th laser sensing symposium, Tokyo, JAPAN, 2015, pp.104-107.
- [3] Y. Saito, "Laser-induced fluorescence spectroscopy/technique as a tool for field monitoring of physiological status of living plants," Proc. SPIE, Vol. 6604, 2007, pp. 66041W-1 -11.
- [4] K. Hitomi, S. Yamagishi, H. Yamanouchi and Y. Yamaguchi, "Detection of Spilled Oil Using a Compact Fluorescence Lidar," J. the Visualization Society of Japan, vol. 22, 2002, pp. 149-153.
- [5] K. Fukuda, R. Niwase, N. Tsumori, "Development of auto-tracking pollution detection system by using various spectroscopic methods," E-proceedings of EMSSES2018, Kyoto, JAPAN, 2018, EN1005

Investigation of Hot Air Production from Fluidized Bed Kiln with Biomass of Rice Husk

Winai Chanpeng

Department of Mechanical Engineering
Rajamangala University of Technology Thanyaburi
Pathumthani, Thailand
winai.c@en.rmutt.ac.th

Phairoach Chunkaew

Department of Mechanical Engineering
Rajamangala University of Technology LannaTak
Tak, Thailand
phairoac9@gmail.com

Abstract—Objective of this research is to construct a hot air production from fluidized bed kiln with rice husk's biomass and to test the performance of its. The main part of the hot air production consists of a fluidized bed kiln, an air chamber, a biomass fuel feeder set, a blower motor of fluidized bed kiln, an air blower, fire burn pocket, cyclone and a control box. The vertical kiln of fluidized bed kiln has 0.23 m in diameter and 2 m of height. The fluidized bed kiln make from steels. New concept of this study use the heat inside the fluidized bed kiln in order to transfers to the surface of it. Air around the fluidized bed kiln will be float up and the air blower will fill the air up until temperature of the air reach the set point. Then the inverter will be commanded to output the signal in order to drive the feeder motor and blower motor of fluidized bed kiln. Motors operate at high speed while the air temperature dose not reached the temperature set point and operate at low speed while the air temperature reaches the temperature set point. Experiments are performed under conditions 170 °C of air temperature with flow rate of 0.0715 kg s⁻¹ during 180 minutes. The biomass of rice husk is selected as the heat source. The thermal efficiency is analyzed and found that the thermal efficiency was 25.82±11.70 %.

Keywords—rice husk, fluidized bed kiln, hot air producer, biomass

I. INTRODUCTION

Fluidized beds are widely used for drying particulate or granular solids in agricultural and food industries. They promote excellent mixing and have high effective heat and mass transfer coefficients. The fluidized bed technique is used in many applications in chemical process, drying and combustion. Technology fluidized kiln is applied in combustion process by using small biomass fuel. It can burn the biomass fuel which is high moisture content.

Sustainable development is an important matter worldwide. Combustion is a thermo chemical process that converts fuel into a hot flue gas which is used to produce heat. Mostly, hot air was applied to use in drying process. The hot air which was generated by electric hot wire was easy to use but this method had more payment. Chunkaew *et al.* (2017)[1] modified hot air dryer using waste heat from a 200 liter kiln by using wood with drying bananas. At drying temperature of 60 °C, the optimal condition is an air velocity of 1.8 ms⁻¹. This research, the fuel wood is big size and must use fixed bed kiln. Nowadays, Thailand has more waste biomass from agriculture production

such as rice husk, sawdust, coconut shell, corncob, scraps of wood, wood from fruit decoration and leaf. In drying process, the main source which is used the most energy comes from the air temperature heating rate.

Biomass energy is the most important alternative energy source for Thailand. Rice husk is the hard protecting coverings of grains of rice. In addition, in order to protecting rice during the growing season, rice husk can be used as a building material, a fertilizer, an insulation material and a fuel [2]. Use of rice husk as fuel is modified to generation of process steam generation for co-generation power plant [3]. Rice husk heating value of each country is different. The rice husk heating value of Taiwan is 17.4 MJ kg⁻¹[4], the rice husk heating value of Brunei is 16.10MJ kg⁻¹[5] and the rice husk heating value of China is 13.40 MJ kg⁻¹[6]. Minimum fluidization velocity (U_{mf}) of the rice husk combustion is 0.3 ms⁻¹ at reactor temperature 642 to 849 °C [7]. In addition, rice husk ash applications are modified in concrete, silica powders, activated carbon and insulator [8].

The objective of this research is to modify a fluidized bed kiln in order to use the rice husk and test kiln performance of thermal efficiency.

II. MATERIALS AND METHODS

A. Hot air production from fluidized bed kiln with waste biomass

- Fluidized bed kiln with waste biomass

Figure 1 shows details of fluidized bed kiln.

-A feeder set has a container dimensions of 0.3 m. x0.295 m. x0.55 m. It has spiral gear with 90 Watt AC motor for feeding the waste biomass from the container to the fluidized bed kiln. The feeder set consists of temperature controller, inverter with control program and AC motor. The inverter receives commands from temperature controller. Motor operates at high speed with high frequency and at low speed with low frequency. This behavior of this shows the feeding rate which various following the speed of the motor.

- Fluidized bed kiln blower is driven by AC motor with 0.5 horsepower which is controlled speed by inverter related to fluidized velocity of rice husk and feeding rice husk

rate. The inverter receives command from the temperature controller. The frequency of feeding rice husk rate is controlled at 25 Hz of high frequency and 15 Hz of low frequency. The frequency of inverter blower of fluidized bed kiln is controlled at 25 Hz of high frequency and 18 Hz of low frequency.

- Fluidized bed kiln is a vertical kiln which has 0.23 m. in diameter and 2 m. of height. The fluidized bed kiln make from steel. The bottom of fluidized bed kiln installs a distributor and joins with tube set and blower.

- Air chamber is designed in a shape as same as fluidized bed kiln and it has 0.334 m. in outlet diameter. The heat from burning biomass of rice husk in fluidized bed kiln is transferred from inside to outside of the kiln. Then, the air in chamber will be increased temperature and flows up from the hot air chamber. The outside of air chamber does not install an insulation.

- Air flow system, at the top of hot air chamber is installed blower and the bottom of hot air chamber is installed a hot air tube for other load of application.

- Cyclone, at the top of fluidized bed kiln is connected with exhaust tube and cyclone. Ash occurs while burning the rice husk in fluidized bed kiln. It has small weight and flows up into the cyclone. Then, the ash is separated at the cyclone and the smoke will be flowed out to the surrounding.

- Control box consists of two inverters, temperature controller, kWh meter and safety switch.

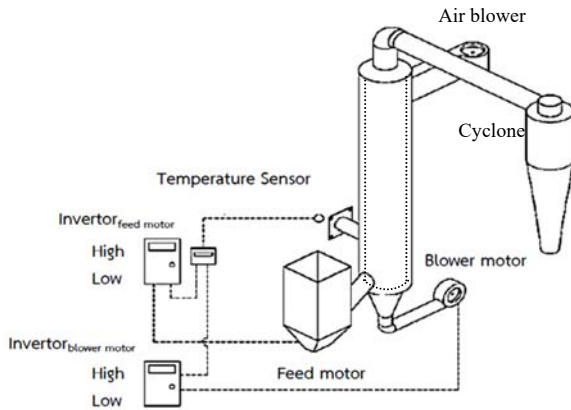


Fig.1 Apparatus of Hot air production from fluidized bed kiln with biomass of rice husk

B. Materials

Figure 2, rice husk is a fuel wood which is an agricultural waste from head rice yield production at Tak Province, Thailand. The rice husk is selected as the heat source and the black ash with small white ash is flowed out from the cyclone. The black ash with small white ash can be used in plant process.



Fig.2 Rice husk and black ash

C. Experiment set up

Experimental procedure is performed under biomass fuel of rice husk. It is tested the hot air production from fluidized bed kiln at a constant temperature of 170 °C with mass flow rate of air 0.0715 kgs⁻¹ in time period of 180 minutes. The mass flow rate is calculated by product of (cross section area) (an air velocity) (density of air). Inlet air temperature is between 27-29 °C. All experiments are tested in 3 times. 3 meters are used to record energy consumptions of fluidized bed kiln blower, feed motor and air blower. The weight of rice husk is recorded by used capacity and used to calculate energy consumption. A temperature recorder (BTM-4208SD) is used to measure several temperatures in the hot air production from fluidized bed kiln with biomass of rice husk such as kiln outside surface temperature and kiln temperature. An ambient temperature and relative humidity of ambient are recorded in order to determine humidity ratio. All data are recorded every 30 minutes.

D. Analysis methods

Thermal efficiency of hot air production from fluidized bed kiln (η_{th}) can be calculated as shown below:

$$\eta_{th} = \frac{\dot{Q}_{out}}{\dot{Q}_{in}} \quad (1)$$

when

\dot{Q}_{out} =heat transfer to the air (kW)

\dot{Q}_{in} =power input(kW)

$$\dot{Q}_{in} = \left[\frac{m_{rice\ husk} \cdot HHV}{t} \right] + 2.6(P_{feed\ motor} + P_{blower\ motor} + P_{hot\ air\ blower\ motor}) \quad (2)$$

$m_{rice\ husk}$ = mass of rice husk (kg)

t = used time (s)

HHV = high heating value of rice husk in Tak, Thailand was 13.79 MJ kg⁻¹ which was tested by bomb calorimeter in laboratory at a department of mechanical engineering, Rajamangala University of Technology LannaTak Tak, Thailand.

2.6 = factor for changing to primary energy [9]

$P_{feed\ motor}$ = power of feed motor (kW)

$P_{blower\ motor}$ = power of blower motor (kW)

$P_{hot\ air\ blower\ motor}$ = power of hot air blower motor (kW).

The dry air and vapor are fluid flow at the air chamber. The heating rate can be calculated as shown below:

$$\dot{Q}_{out} = \dot{m}_a [(C_{a2}T_2 + WC_vT_2) - (C_{a1}T_1 + WC_vT_1)] \quad (3)$$

when

\dot{Q}_{out} = heat transfer to the air (kW)

\dot{m}_a = mass flow rate of dry air ($kg\ s^{-1}$)

C_{a1} = specific heat capacity of dry air of inlet heat exchanger ($kJ\ kg^{-1}C^{-1}$)

C_{a2} = specific heat capacity of dry air of outlet heat exchanger ($kJ\ kg^{-1}C^{-1}$)

W = humidity ratio ($kg_{water}\ kg_{dry\ air}^{-1}$)

C_v = specific heat capacity of vapor ($kJ\ kg^{-1}C^{-1}$)

T_1 = temperature of inlet of dry air at heat exchanger ($^{\circ}C$)

T_2 = temperature of outlet of dry air at heat exchanger ($^{\circ}C$).

III. RESULTS AND DISCUSSIONS

Behaviors of kiln outside surface temperature, kiln temperature and biomass amount and thermal efficiency are present.

A. Behaviors of kiln outside surface temperature, kiln temperature and biomass amount

At condition of 170 °C with air flow rate of 0.0715 kg/s from 0 to 180 minutes shows that after 30 minutes has passed, an average kiln outside surface temperature is 277.23±8.33°C, an average kiln temperature is 551.27±31.45°C and a biomass amount is 25±11.85 kg as shown in Figure 3. The average feed rate of rice husk is 0.16± 0.03 kg/min and the average feed rate of ash is 0.030± 0.014 kg/min. At the period of 30 minutes has more rice husk because fluidized bed kiln is being to burn and some heat is absorbed by structure of the fluidized bed kiln. After 30 minutes has passed, the rice husk is decreased because the system of the fluidized bed kiln is beginning to stabilize.

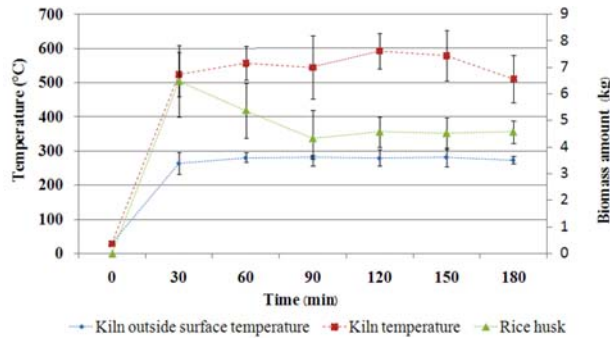


Fig.3. Behaviors of kiln outside surface temperature, kiln temperature and rice husk amount

A. Behaviors of power input, heat transfer to the air and Thermal efficiency

From equation 2, a power input consists of a power of feed motor, a power of blower motor, power of hot air blower motor and heat rate from the rice husk. It was found that behavior of power input had same behavior of feeding rice husk as shown in figure 4. The average of the power input is 38.51±6.312 kW. Behavior of heat transfer to the air, hot air production has reach 170 °C with air flow rate of 0.0715 $kg\ s^{-1}$ at 30 minutes as shown in figure 5. The average heat transfer to the air is 10.8±0.32 kW. Finally, the behavior of thermal efficiency is increased during the period of time from 0 to 90 minutes after that the thermal efficiency will be stable as shown in figure 6. The average thermal efficiency is 25.82±11.70 %.

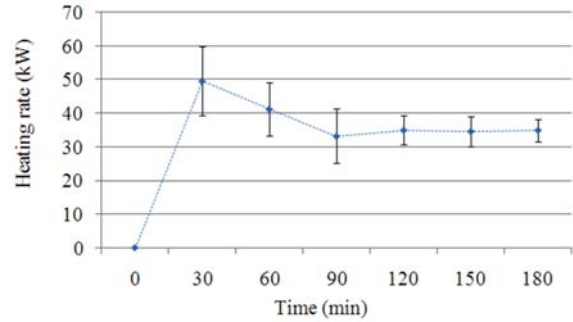


Fig.4. Behavior of power input versus time at temperature of 170 °C with mass flow rate of air 0.0715 $kg\ s^{-1}$

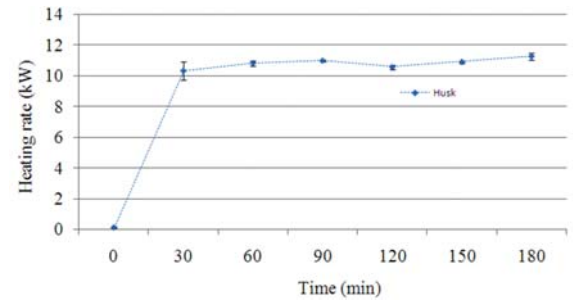


Fig.5. Behavior of heat transfer to the air versus time at temperature of 170 °C with mass flow rate of air 0.0715 $kg\ s^{-1}$

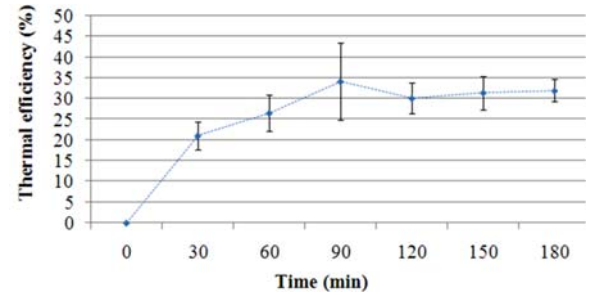


Fig.6. Behavior of thermal efficiency versus time at temperature of 170 °C with mass flow rate of air 0.0715 $kg\ s^{-1}$

Table 1 shows the calculation values of experimental results for hot air production at $170.01 \pm 3.09^\circ\text{C}$ with air flow rate of 0.0715 kg/s from 0-180 minutes. An ambient temperature and a relative humidity of ambient were $28.12 \pm 0.93^\circ\text{C}$ and $94.26 \pm 11.24 \%$, respectively. They were input air for requirement up to high temperature of 170°C . It was found that the rice husk was used amount $25 \pm 11.85 \text{ kg}$ and the thermal efficiency was calculated by equation 1 and the thermal efficiency was $25.82 \pm 11.70 \%$. Heat which was lost at the wall of fluidized bed kiln and the exhaust was about 74%.

Table 1 The calculation values of experimental results for hot air production at 170°C with air flow rate of 0.0715 kg/s from 0-180 minutes.

Descriptions	Calculation values
Rice husk (kg)	25 ± 11.85
Ash (kg)	5.83 ± 1.39
Ambient temperature ($^\circ\text{C}$)	28.12 ± 0.93
Relative humidity of ambient (%)	94.26 ± 11.24
Hot air temperature ($^\circ\text{C}$)	171.01 ± 3.09
Kiln outside surface temperature ($^\circ\text{C}$)	277.23 ± 8.33
Kiln temperature ($^\circ\text{C}$)	551.27 ± 31.45
Exhaust temperature ($^\circ\text{C}$)	412.36 ± 42.97
Heat transfer to the air (kW)	10.8 ± 0.32
Total input heating rate (kW)	38.51 ± 6.312
Thermal efficiency (%)	25.82 ± 11.70

IV. CONCLUSIONS

The hot air production from fluidized bed kiln with biomass of rice husk introduce a new concept of heat in the fluidized bed kiln which transfer from inside kiln to outside kiln. The air in chamber beside an outside kiln is flowed up. Then, the air blower produces the air flow which has temperature at the set point. The temperature controller is used to control the burning of rice husk in the fluidized bed kiln by using two inverters to control the feeder motor and blower motor of fluidized bed kiln. Experiments are performed under the condition at 170°C with air flow rate of 0.0715 kg s^{-1} which started from 0 to 180 minutes. The biomass of rice husk is selected as the heat source. All experiments were tested in 3 times. The average kiln outside surface temperature was $277.23 \pm 8.33^\circ\text{C}$. The average kiln temperature was $551.27 \pm 31.45^\circ\text{C}$. The biomass amount was $25 \pm 11.85 \text{ kg}$. The average of the power input was $38.51 \pm 6.312 \text{ kW}$. The average heat transfer to the air was $10.8 \pm 0.32 \text{ kW}$. The drying performances were analyzed a thermal efficiency. It showed that the thermal efficiency was $25.82 \pm 11.70 \%$.

REFERENCES

[1] P. Chunkaew, A. Khadwilard and Ch.Thawongamyingsakul, "Drying bananas with a modified hot air dryer using waste heat from a 200 liter kiln," RMUTI journal, Vol.10, No.3, pp. 1-12, 2017.

[2] Wikipedia, "Rice husk" https://en.wikipedia.org/wiki/Rice_hulls (accessed on 7/02/2018).

[3] M.R. Gidde and A.P. Jivani, "Waste to wealth-potential of rice husk in India a literature review," Proceedings of the International Conference on cleaner technologies and environmental management PEX, Pondicherry, India, January 4-6, 2007. PP. 586-590.

[4] M.J. Wang, Y.F. Huang, P.T. Chiueh, W.H. Kuan and S.L. Lo, "Microwave-induced torrefaction of rice husk and sugarcane residues," Energy 37, pp. 177-184, 2012.

[5] S. Muhammad, A. Bakar and J.O. Titiloye, "Catalytic pyrolysis of rice husk for biooil production," J. Anal. Appl. Pyrol. 103, pp. 362-368, 2013.

[6] M. Fang, L. Yang, G. Chen, Z. Shi, Z. Luo and K. Cen, "Experimental study on rice husk combustion in a circulating fluidized bed," Fuel Process, Technol. 85, pp. 1273-1282, 2004.

[7] G. M. Faé Gomes, C. Philipssen, E. K. Bard, L. Dalla Zen and G. de Souza, "Rice husk bubbling fluidized bed combustion for amorphous silicasynthesis," Journal of Environmental Chemical Engineering 4, pp. 2278-2290, 2016.

[8] J. Prasara-A and S. H. Gheewala, "Sustainable utilization of rice husk ash from power plants: A review," Journal of Cleaner Production, 167, pp. 1020-1028, 2017.

[9] A. Achariyaviriya, "Simulation and optimization of the drying strategy for longan drying," Doctor of Engineering Energy Technology Program School of Energy and Materials. King Mongkut's University of Technology Thonburi, 2001.

Collection of Variable Datas Affected Electricity Generation of PV Array with FIO Board STM 32F4

Akeratana Noppakant
Department of Electrical Engineering
Faculty of Engineering, Thonburi University
Nongkanplu, Nongkhame, Bangkok Thailand 10160
E-mail: eg1322@gmail.com

Jirasak Songboonkaew
Department of Electrical Engineering
Faculty of Engineering, Thonburi University
Nongkanplu, Nongkhame, Bangkok Thailand 10160
E-mail: jirasak1163@gmail.com

Abstract— This research presents a data logger of variable datas that affect the production of solar electricity. To determine the effectiveness of solar cell by record the voltage, current, temperature and light intensity of solar light.

The principle of this design using PV solar panel connected as a source, controlled by Fio2 STM32F4 Discovery with MATLAB/SIMULINK program to process. The datas was receiving the signals from the various sensors such as Hall Effect current sensor, LDR and thermistor, then saved it to a memory card(Micro SD card) and sent the measured value to a computer.

Results showed that the average error of measurement and recording is equal to 1.05% the efficiency of solar cell with an average of 50%, voltage average of panel per day is equal to 11.71 volts. The average current 0.43 amps, average power 5 watts and peak sun hour(PSH) is 4.50 hours.

Keywords— Data logger, PV array, Fio board

I. INTRODUCTION

The collection of variable datas from photovoltaic power generation plants mostly use a meter and take notes, it consumes human resources and less details of datas Other than that, it was recorded using expensive equipment. Now, the creation of a device to store variables value datas affect the electricity generated by photovoltaic [1] depending on temperature, sunlight intensity. This research is a development of instrument controllers to interface with MATLAB/SIMULINK applications, easier and more convenient using USB connection (HID) and also use SIMULINK to analyze a complex data information to simplify the operation.

II. THEORY AND IMPLEMENTATION

A. Light Dependent Resistor

[2][3] LDR is a resistance that can change the conductive when the light comes, another name call Photo resistor or Photo conductor which are made from a semiconductor cadmium sulphide that plaster on the ceramics plate. The shape of LDR consist of black small coil act as a light sensitive and they are separate into two parts, such as the electric conductor and device body.

The function of LDR was, when the light goes down, it send the energy to the plastered substance causing the hole and electron are free moving, that affect to varies resistance value. For the light intensity, if brighter of the light it will decreasing more resistance and this sensor only work in the light length between 4,000 – 10,000 angstroms.

The LDR resistance ratio between with or with out light intensity might work between 100 – 1,000 time depend on the model of device, generally the resistance when without light intensity used power at 0.5 mw. or more, then, used power more than 2 mw. when its dark and 10-20 kw. or more at the sunlight. This device can hold up 100 volts of voltage break down with power loss at 50 mw.

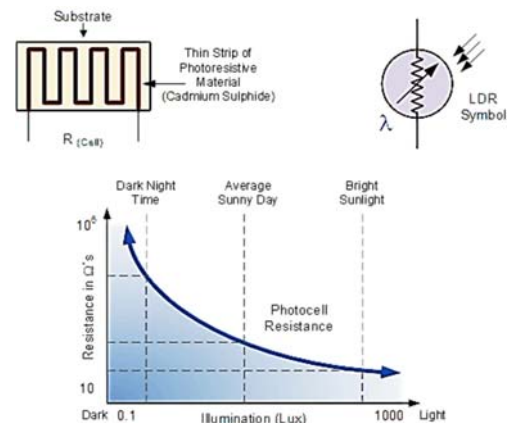


Fig 1. LDR characteristics

B. Hall Effect current sensor

Current sensor with Hall Effect type or di/dt, generally used the principle of Hall Effect theory which is made of semiconductor. The principle of this device was used the electromagnetic field flow through and then injected the current into the side of semiconductor rod. From Fig. 2 the P-type of semiconductor rod place into where of magnetic field passing through and feed the voltage to positive side of semiconductor that will push the hole of electron moving to the other side. The Hall Effect sensor will convert the magnetic field density into electric signal.

The electric field from hall electric field occurred when the flux perpendicular with the direction of electric current, which is directly proportional to the angle of carrier and the third side of hole then, form into hall electric filed and compensated to Lorentz force electric field for stop moving of carrier in the direction that perpendicular and current direction affect into the side of semiconductor to produce less voltage.

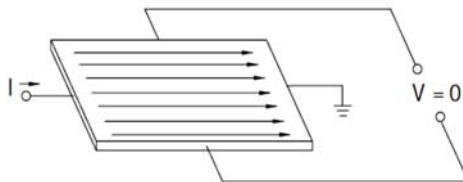


Fig 2. Hall Effect current sensor principle

C. RapidSTM32 and Fio Board

[4] Fio boards and RapidSTM32 is a blockset of developed and manufactured by Thais. Currently Fio board was in the domestic and international market, the design of this board expected to use with RapidSTM32 block set controlled by MATLAB/Simulink function.

The Fio board is a trial version of STM32TM ARM 32-bit microcontroller. The cortexTM M3 processor boards is Fio standard compatible with MATLAB/Simulink. The board is designed is designed for teaching of university student and high school in many ehgineering feature is the used such as automation control system, robot, digital signal processing(DSP), etc. Fio std board feature is the use especially for programming because of the graphical programming via Simulink. The MATLAB, whichis a module in matlab program, can understand the work of project and various device, communication between devices, algorithms, programming and more.

III. MODEL OF SYSTEM

This paper demonstrated the modelling of collection variable datas affected electricity generation of PV array. The system included RapidSTM32F4 board, current sensor, LDR and computer to stored all datas.

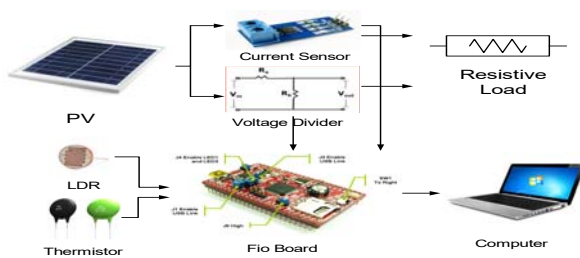


Fig 3. Block diagram of RapidSTM32F4

The block diagram of collection variable datas system is given in Fig 3. The monocrystalline PV array is used configuration as a generator, Hall Effect current sensor measure a current and voltage then LDR measured light intensity and thermistor measured temperature varies on resistance of thermistor. All datas from all sensors stored to micro SD card and computer

Base on designed by modeling of collection of variable datas system using Matlab/Simulink to control the process, the system will generate an unstable characteristic of voltage and current varies on time period in a day and temperature of PV array was affected in the system.

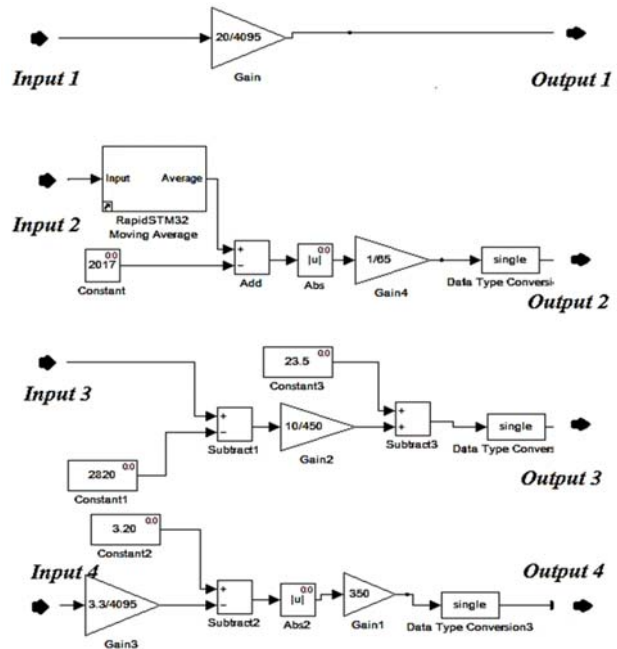


Fig 4. Analog to Digital conversion

Fig 4. Shows the order of ADC to convert analog signal separate in 4 parts such as, input 1 measured voltage receive signal from voltage divider circuit, input 2 measured current receive signal from Hall Effect sensor, input 3 measure temperature received signal from thermistor and input 4 measure light intensity received signal from LDR. The input signal has a resolution value of 12 bits or $(2^{12} - 1) = 4095$ each sensors detector needs to be set up to the appropriate threshold value and converted to get the closest to the actual value.

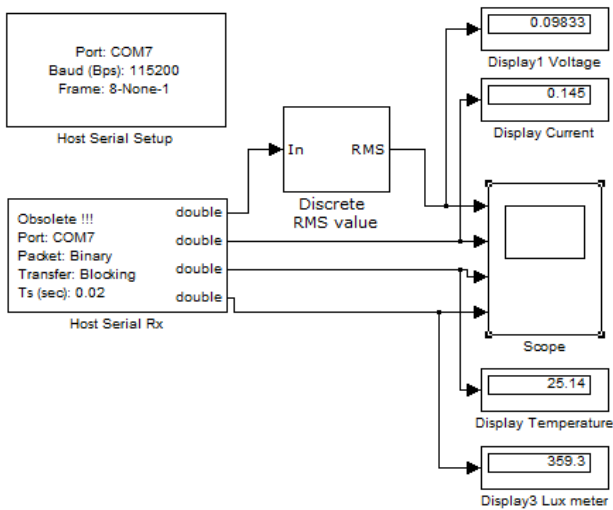


Fig 5. Block diagram of Host series port

Fig 5. Simulink programming using the computer to receive values from the RapidSTM32F4 to display on the computer screen via USB port. The data is delivered through the AMG USB Converter - N adapter which is an important toolbox that needs to be configured. The Host Serial Setup toolbox must be synchronized with the transmitter and set to Bit Data, and in the Host serial RX toolbox

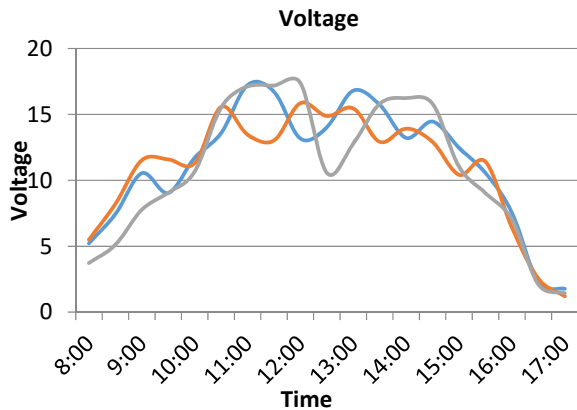


Fig 6. voltage Charging

Fig 6. Shows the difference of voltage charging of each day and state of charge of each hour. PV panel generate between 3-18 Vdc. from 8.00-17.00 pm.

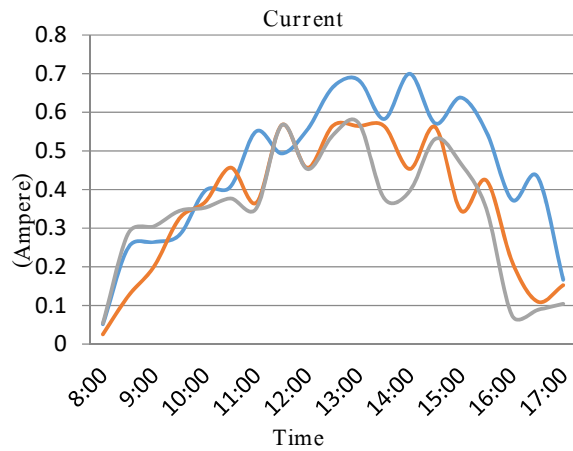


Fig 7. Charging Current

Fig 7. Shows the charging current of each hour for 3 days, each show in difference color of line. The charging current started from 0.02-0.6 A. during the time, the best performance at 12.00 pm. will generate mostly current.

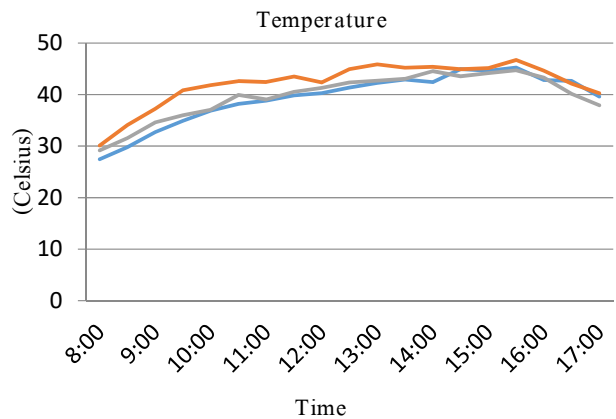


Fig 8. Temperature of PV array

Fig 8. Shows Temperature values of solar panels has higher the value of heat accumulation under the panel and the temperature rise from 30 degree Celsius in the morning to 45 degree Celsius in the evening.

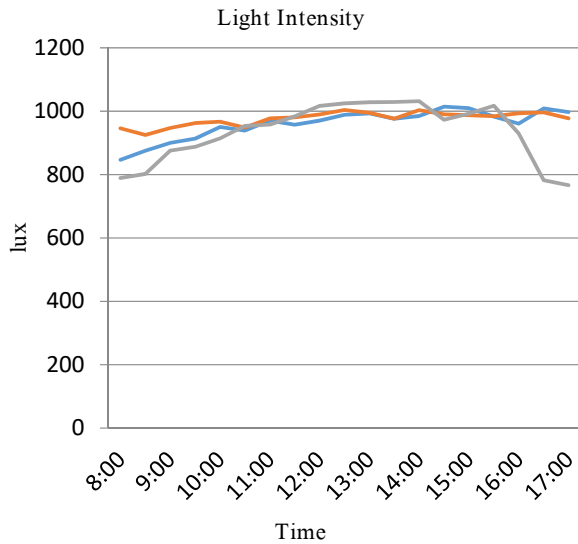


Fig 9. Lighting Intensity

Fig 9. Show the intensity of light that is stored in a 3-day period. The intensity of light is approximately 800 lux in the morning and the maximum in the daytime is about 1000 lux, which affects the production of solar cells.

Table 1. Performance results tables

Day	Avg. voltage (v)	Avg. current (A)	Power (W)	Efficiency (%) (w/10 x100)	Total Time (hr.)	Avg. Power (wh)	Total time Intensity (hr.)
1	11.89	0.50	5.95	59.5	9	53.55	5.35
2	11.43	0.41	4.69	46.9	9	42.21	4.22
3	11.80	0.37	4.37	43.7	9	39.29	3.93
Avg.	11.71	0.43	5.00	50	9	45.00	4.50

The 3 days daily average of voltage at 11.71 volts, the average current at 0.43 amps, calculate electric power was 5.00 watts, indicating that solar panels had an efficiency of 50%. The electrical power per day was 9 hours. x 5.00 watt = 45.00 watt-hours, there was one day the solar cell has a Peak sun hour = 45.00 / 10 = 4.50 hours.

Table 2. Compared results tables

Voltage		Current		Temperature		Intensity	
Multi Meter (V)	Fio Board (V)	Amp. Meter (A)	Fio Board (A)	Thermo Meter (celsius)	Fio Board (celsius)	Lux meter (Lux)	Fio Board (Lux)
20	20.03	2	2.11	22	21.12	250	254.05
20	20.08	2	2.01	22	22.35	250	255.01
20	20.09	2	2.08	22	23.01	250	254.22
20	20.01	2	2.05	22	21.05	250	254.75
20	20.01	2	2.08	22	22.05	250	254.89
20	20.02	2	2.00	22	23.04	250	252.99
20	20.02	2	2.01	22	22.08	250	253.01
20	20.01	2	2.01	22	22.12	250	254.15
20	20.02	2	2.01	22	22.11	250	253.78
20	20.03	2	2.02	22	22.11	250	254.12
Avg.	20.03	Avg.	2.04	Avg.	22.10	Avg.	253.99

Table 2. shows that results from testing of the instrument for finding of the performance and the error of from the machine. The test was separate in four sections, the results of each section compared to standard instrument used and test 10 times of each part. The first section was measured a voltage, the results of this section compared between multi-meter and STM 32F4 board was average 20.03 volts, the second section was measured current was average 2.04 Ampere, the third section was measured temperature was average 22.10 celsius and the fourth section was measured intensity was average 253.99 lux.

IV. RESULTS

The measurement error of this instrument was found to be 0.15% voltage error, the error of the current measurement was 2%, the error in the temperature measurement was 0.45% and luminance measurement error was 1.60%. The overall performance of this instrument average error for RapidSTM32F4 board was 1.05%. and can record all datas to the Micro SD Card including the voltage and current of the solar panels, daily temperature and brightness values for three days can summarize the functions of the machine and the parameters in table 2.

Table 3. Specification machine tables

Characteristic	
Input	220 V ± 10% / 50 Hz
Max Current.	5 A (DC)
Max Voltage measurement.	20 V (DC)
Max Temperature.	60 Celcius
Max Lighting Intensity.	1000 lux
Controller	Open Loop Digital Control
Display	LCD 16x4
Processor	Rapid STM32 F4 Discovery
Memory	Micro SD Card 4 Gb
Reading Data Process	1 bit data/0.01 second (varies on software)
Hub Adaptor	USB Converter - N Adapter Comport Data bit = 8, Buad rate = 115200

V. CONCLUSION

The collection of variable datas affected electricity generate of PV array with FIO board STM32F4 by using current sensor, LDR and thermistor to read signal and collect datas stored into Micro SD card and computer with Microsoft excel program. This research aims to find an efficiency of solar panel in this day. The results of this research shows the performance of this solar panel is 50% of the power generation.

REFERENCES

- [1] Anusorn sangprajuk and Thanya songkapuntanon B.E 1998, Basic of Solar Energy, bangkok, 2016, Download from http://leonics.co.th/html/th/aboutpower/solar_knowledge.php
- [2] Eakkaphob Jaisat B.E 2011 Temperature sensor, 2016 Download from <http://eakkaphob0140.blogspot.com/p/blog-page29.html>.
- [3] Siwapong Tisopha B.E. 2015 LDR Sensor, 2015 Download from http://electhai.blogspot.com/2013/08/ldr_24.html
- [4] Aimagin Co. Ltd, 2015 WaijungBlockset. [online] Avariable: <http://waijung.aimagin.com>
- [5] Sanpong Thanonk B.E 2016 Microprocessor & Interfacing, 2016 Download from <http://aimaginblog/lang-th>.

Optimal Mixture Experiment Design Using Neural Network

Dussadee Buntam

Faculty of Engineering

Pathumwan Institute of Technology (PIT)
Bangkok Thailand

Email: dussadeebuntam@gmail.com

Wachirapond Permpoonsinsup

Faculty of Engineering

Pathumwan Institute of Technology (PIT)
Bangkok Thailand

Email: wachirapond.pit@gmail.com

Prayoon Surin

Faculty of Engineering

Pathumwan Institute of Technology (PIT)
Bangkok Thailand

Email: prayoon99@gmail.com

Abstract— Forming process is essential and necessary for manufacturing system. Mixture experiments are useful in industrial situation to find the parameters in design and development process. Artificial Neural Network (ANN) is the mathematical model to approximate and predict a nonlinear function. In this study, the objective is to simulate optimal parameters mixture experiments by the ANN. The ANN architecture is widely used that is feed-forward back propagation. There are two design methods namely, integration with mixture design and factorial design. In the integration with mixture design, the input data, pellet talcum, are trained for ANN. The target data are from factorial design. Training algorithms in the experiments, Gradient descent, Gradient descent with momentum and Levenberg Maquardt algorithms are applied to optimize components. The performance of ANN model can be indicated by mean square error (MSE) and linear regression (R). As a result, ANN can predict yield of forming process of pellet talcum.

Keywords— artificial neural network; mixture design; mineral talcum

I. INTRODUCTION

Mineral talcum production is the one of important process in industry. Mineral talcum is a components in cosmetic, powder paper and lime. Uttaradit province is the original resource to produce mineral Talcum in Thailand. There are many mining industry and processing factory mineral talcum in Uttardit province. For 30 year ago, the most industry is only primary processing factory which is blending and packaging to other suppliers.



(a) Original mineral talcum



(b) Mineral talcum pellet

Fig. 1. Mineral Talcum Process

The characteristic of mineral talcum is very small pieces of powder so it spreads during package and transportation. Not

only it affects health but also it is the cause of environmental problems including carcinogens of cancer. To reduce spreading mineral talcum, the production process should be based on the environmental management standard, ISO 14000. Thus, the mineral talcum factories should develop a new process to change original mineral talcum in Fig.1 (a) to mineral talcum pellet in Fig.1 (b). According to Fig.1, mineral talcum is mixed with a few water, it is broken and isolated. In case of more water, it is flat shape. In following problems on shape of mineral talcum, the optimal mixture experiment design using ANN is applied to solve forming process of mineral talcum. ANN models are designed to predict yield forming process for reducing the defect. In this paper, the aim is to optimize the components of water and mineral talcum in forming process by artificial neural network model.

II. BACKGROUND AND LITERATURE REVIEWS

A. Literature reviews

Macleod et al. have applied ANNs and Taguchi method were used to predict hardest of cement. Taguchi methods offer potential benefits in evaluating network behavior such as the ability to examine interaction of weights within neurals a network [1]. Adroer et al. presented neural network model for predicting the honing process variables (grain size of abrasive, density of abrasive, linear speed, tangential speed and pressure) as a function of roughness parameters [2]. Yadollahi et al. have investigated the optimal mixture of RSC containing lead-slag aggregate used Taguchi method and ANN. They have also predicted component of UV-protection concrete by important factor which had three variables as slum, compressive strength and gamma linear attenuation. The coefficient were considered as the quality responses [3]. Sukru Ozsahin have studied an ANN model which was developed for predicting the effects of some production factors such as adhesive ratio, press pressure, time, wood density and moisture content on some physical properties of oriented strand board (OSB). The results showed that the prediction model was a useful, reliable and quite effective tool for predicting some physical properties of the OSB produced under different manufacturing conditions [4].

B. Artificial Neural Network

A biological neural network is a series of interconnected neural and a biological process in the human brain. The simple processing elements are connected by weighted. The forming are combined from a number of the simple processing elements. The simple processing elements compute the output by a non-linear function of weight inputs [5]. According to Fig.2, the biological neuron is demonstrated. The signals transmitted through the cell body (soma) which are from the dendrite to the axon as an electrical impulse.

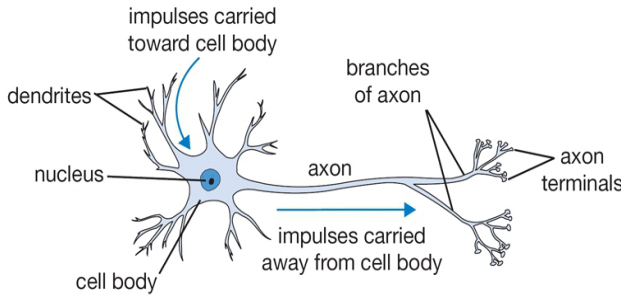


Fig. 2. A biological neuron [6]

1) Activation Function

In artificial neural network models, each neuron amount to its inputs, and then feeds the sum into a function. The activation function determines the neuron output. Commonly, the activation functions are also called as transfer functions. The net output of any node are computed by the activation function before feeding to the next layer. There are 3 typical types of activation functions; purelin, logsig and tansig [6] as shown in equation (1), (2) and (3), respectively.

Purelin function can be defined as

$$f(n) = n \quad (1)$$

Logsig function is shown as

$$f(n) = \frac{1}{1 + e^{(-n)}} \quad (2)$$

Tansig function is derived as

$$f(n) = \frac{1 - e^{(-n)}}{1 + e^{(-n)}} \quad (3)$$

where n is the net input.

f is the activation function.

2) Architectures of Neural Networks

a) Feedforward Neural Networks

Feedforward neural networks compose of a series of layers. They are the most widely used architecture of neural networks. In feedforward neural networks, the first layer has a connection from the network input to output unit which are strictly feedforward. Consequently, each subsequent layer has a connection from the previous layer and then the final layer produces the network's output. A feedforward multilayered neural network can approximate a continuous function arbitrary well. Fig. 3 shows a single layer of neuron. It consists of one input and an output layer.

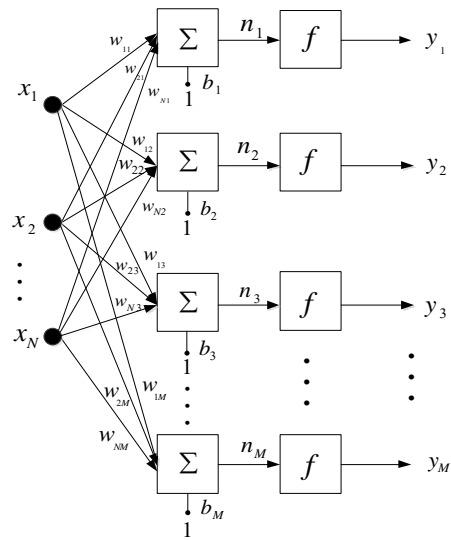


Fig. 3. Feedforward neural networks without hidden layer

Fig. 3 has the input vector, \mathbf{x} and a weight vector, \mathbf{w} in input layer. The net input vector, \mathbf{n} , a bias vector \mathbf{b} is contained.

The net input vector can be deduced as

Substituting equation (4) to an activation function, the output is calculated as

$$\mathbf{y} = \mathbf{f}(\mathbf{w}\mathbf{x} + \mathbf{b}) \quad (4)$$

b) Training algorithm

In a learning network, a procedure for modifying the weights and biases of network can be referred to as training algorithm. There are three to adjust weight namely, gradient descent algorithm (GDA), gradient descent with momentum algorithm (GDMA) and Levenberg-Marquardt algorithm (LMA).

Gradient descent algorithm is based on the first-order derivative of objective error function. Let $E(\mathbf{w})$ be objective error function. To find the minima in error space, gradient vector, \mathbf{g} of $E(\mathbf{w})$ can be defined as [7]

$$\mathbf{g} = \frac{\partial E(\mathbf{w})}{\partial \mathbf{w}} \quad (5)$$

Applying the gradient descent to the weight vector, the direction is opposite the gradient vector. GDA updates the new weight vector at iteration, k as equation (6)

$$\mathbf{w}_{k+1} = \mathbf{w}_k - \alpha \mathbf{g}_k \quad (6)$$

where k is the iterative number

α is the learning rate

\mathbf{g}_k is the gradient with respect to the weights.

In the iteration, weight may oscillate. If the oscillation is large then weight must be updated. Since the new weight, \mathbf{w}_{k+1} depends on the past weight, \mathbf{w}_k and the change ($\Delta\mathbf{w}_k$). To fulfill this requirement, $\beta\Delta\mathbf{w}_k$ is added into equation (6), it is called GDMA. \mathbf{w}_{k+1} is defined as

$$\mathbf{w}_{k+1} = \mathbf{w}_k - \alpha\mathbf{g}_k + \beta\Delta\mathbf{w}_k \quad (7)$$

where $\Delta\mathbf{w}_k$ is a weight change of the previous step
 β is the momentum parameter.

Levenberg Marquardt algorithm outperforms the gradient descent and conjugate gradient methods for medium size of non-linear least squares problems [8]. LMA finds the minimum of a function that is expressed as the sum of squares of non-linear real-valued function. LMA to update new weight vector can be obtained as follows

$$\mathbf{w}_{k+1} = \mathbf{w}_k - (\mathbf{J}_k^T \mathbf{J}_k + \mu \mathbf{I})^{-1} \mathbf{J}_k^T \mathbf{e}_k \quad (8)$$

where μ is the scalar factor
 k is the number of iteration
 \mathbf{J} is the Jacobian matrix
 \mathbf{e} is the vector of network errors.

C. Mixtures Design

Mixtures design is a one of factorial experimental design. It is different from other types of experiment design because the percentage of a component increase to 100%. The increasing level of constituent can balance the proportion of the mixtures. Following experiment design, ANOVA models are widely used based on factorial design. The regression analysis is mainly used, linear, quadratic and cubic response surfaces that are assumed in dependence on the mixture components. In a mixture experiment, the factors are different components of a blend to optimize components for example the tensile strength of stainless steel and the interesting factors which might be iron, copper, nickel and chromium in the alloy. Moreover, gasoline, soaps or detergents, beverages, cake mixes, soups and so on are optimized either [9].

III. PROPOSED METHOD

A. Mixture process

Mixture process is considered the factors that affect to talcum pellet. The components between water and mineral talcum are optimized for forming process to reduce the broken and isolated. Let input be mixtures of water and mineral talcum and output be weight of talcum pellet. The yield under two variables is defined as equation (9).

$$\text{Yield}(\%) = \frac{\text{Output}(\text{kg})}{\text{Input}(\text{kg})} \times 100 \quad (9)$$

B. Experimental component

In this paper, Table I shows the cases of the components of mineral talcum. The components are from the talcum process in the real factory in Uttardit province.

TABLE I. EXPERIMENT CASES OF MIXTURE DESIGN

Trial	Component (%)	
	Water	Mineral talcum
1	25	75
2	10	90
3	17.5	82.5
4	21.25	78.75
5	13.75	86.25
6	17.5	82.5

Table II shows trials, percentage of components which compose of talcum and water and percentage of each replication (Rep.) in yield. The collection data of talcum pellet process are shown as 1-5 trials. In trial 6, it replicates in a center.

TABLE II. RESULT OF YIELD FROM MIXTURE DESIGN

Trial	Component (%)		Yield (%)		
	talcum	water	Rep. 1	Rep. 2	Rep. 3
1	75	25	63.19	60.31	64.80
2	90	10	63.39	71.85	68.62
3	82.5	17.5	81.59	80.33	78.70
4	78.75	21.25	72.99	74.99	71.70
5	86.25	13.75	82.40	85.81	86.45
6	82.5	17.5	83.21	80.55	80.41

C. Design neural network model

In this paper, feedforward neural networks with backpropagation were designed to find the optimal components of mineral talcum and water. Supervised learning algorithm was applied that is GDA, GDAM and LM. Table III shows the experiment cases of ANN model for 18 models which have involved topology, transfer function and training algorithm.

TABLE III. EXPERIMENT CASES OF NEURAL NETWORK MODEL

Model	Topology	Transfer Function	Training Algorithm
1	2-5-1	purelin	traingd
2	2-5-1	purelin	traingdm
3	2-5-1	purelin	trainlm
4	2-5-1	logsig	traingd
5	2-5-1	logsig	traingdm
6	2-5-1	logsig	trainlm
7	2-5-1	tansig	traingd
8	2-5-1	tansig	traingdm
9	2-5-1	tansig	trainlm
10	2-10-1	purelin	traingd
11	2-10-1	purelin	traingdm

Model	Topology	Transfer Function	Training Algorithm
12	2-10-1	purelin	trainlm
13	2-10-1	logsig	traingd
14	2-10-1	logsig	traingdm
15	2-10-1	logsig	trainlm
16	2-10-1	tansig	traingd
17	2-10-1	tansig	traingdm
18	2-10-1	tansig	trainlm

TABLE IV. PARAMETERS OF NEURAL NETWORK MODEL.

Training parameter	Value
Maximum number of epochs to train	1000
Minimum value of performance function	10^{-9}
Minimum value of gradient, g	10^{-7}
Initial factor parameter, μ	0.001
Decreasing factor of μ , $\Delta^+ \mu$	0.1
Increasing factor of μ , $\Delta^- \mu$	10
Maximum value of μ , $\max \mu$	10^{10}

D. Performance of neural network model

Mean square error (MSE) is used to measure the performance of neural network model [10]. It can be define as

$$E_{MSE} = \frac{1}{N} \sum_{i=1}^N (Output_i - Observed_i)^2 \quad (10)$$

where $Output_i$ is the i -th network output
 $Observed_i$ is the i -th target data
 N is the total number of output nodes.

IV. EXPEREMENTAL RESULT

There are two topologies of neural network model were trained. In this proposed method, transfer functions, purelin, logsig and tansig, were applied to the models. Consequently, the ANN models included the training algorithms, traingd, traingdm and trainlm to adjust weights. The performance of the neural network model can be measure by MSE. The correlation between the model outputs and observed data can be represented in regression, R values. If R value of 1 means a close relationship then it 0 means a random relationship otherwise it is close to -1 which is no relationship. The experimental results are as shown in Table V.

TABLE V. EXPERIMENT RESULT OF NEURAL NETWORK MODEL

Model	Topology	Transfer Function	Training Algorithm	Regression (Training)	MSE
1	2-5-1	purelin	traingd	-0.258	0.0144
2	2-5-1	purelin	traingdm	0.617	0.0185
3	2-5-1	purelin	trainlm	0.455	0.0056
4	2-5-1	logsig	traingd	0.276	0.0069
5	2-5-1	logsig	traingdm	0.368	0.0057
6	2-5-1	logsig	trainlm	0.317	0.0155

Model	Topology	Transfer Function	Training Algorithm	Regression (Training)	MSE
7	2-5-1	tansig	traingd	-0.615	0.0101
8	2-5-1	tansig	traingdm	0.079	0.0271
9	2-5-1	tansig	trainlm	0.978	0.0007
10	2-10-1	purelin	traingd	0.413	0.0081
11	2-10-1	purelin	traingdm	0.893	0.0094
12	2-10-1	purelin	trainlm	0.491	0.0055
13	2-10-1	logsig	traingd	0.954	0.0080
14	2-10-1	logsig	traingdm	-0.432	0.0183
15	2-10-1	logsig	trainlm	0.965	0.0005
16	2-10-1	tansig	traingd	0.750	0.0061
17	2-10-1	tansig	traingdm	-0.554	0.0194
18	2-10-1	tansig	trainlm	0.882	0.0034

According to Table V, the experimental 2-5-1 topology in model number 1 to 9, was trained with traingd, traingdm and trainlm, involving transfer function that is purelin, logsig and tansig. R value of model 9 has 0.978 and MSE is 0.0007. R of model 9 are higher than other models. In addition, MSE is less than others. In model 10 to 18 based on the 2-10-1 topology, R value of model 15 is 0.965 which is higher than other models. Moreover, MSE, 0.0005, is less than others.

Figure 4 and 5 show observed yield and output yield of neural network models.

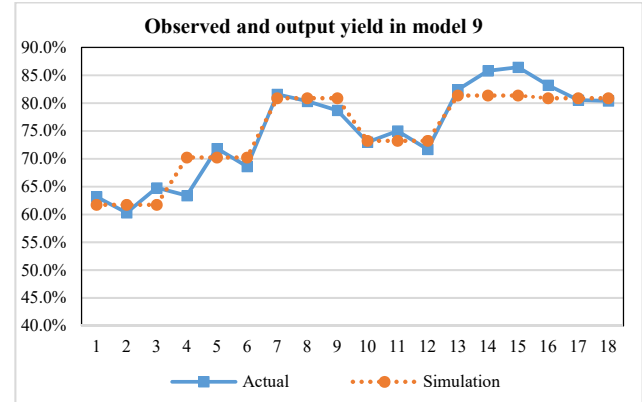


Fig. 4. Observed and output yield in model 9

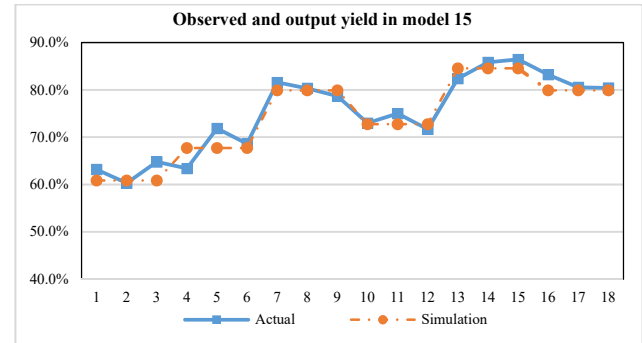


Fig. 5. Observed and output yield in model 15

V. CONCLUSIONS

In this paper, neural network models are applied to optimize the mineral talcum and water in mixture design. There are presented 18 models. Model 9 has 2-5-1 topology which is trained by Levenberg Maquardt algorithm and has transfer function in tansig function. The correlation in experimental results, model 9 and model 15 have a small difference of R value, only 0.013. It shows that model 9 has close relationship than model 15. Considering the performance of neural network models between model 9 and model 15 having a small difference MSE, however the performance of model 15 is better than model 9. As a result, the neural network models to optimize mineral talcum components for mixture design that is model 15.

Implementing the neural network model, the model 9 and model 15 can provide the optimal components for mineral talcum process that produce the mineral talcum pellet with machine in Uttaradit province. It will increase accuracy and productivity. Moreover, it helps production plan and defines standard of mixture.

REFERENCES

- [1] C. MACLEOD, G. DROR and G. MAXWELL, "Training Artificial Neural Networks Using Taguchi Methods," *Artificial Intelligence Review*, pp. 177-184, 1999.
- [2] M. S. Adroera, X. L. Parrab, I. B. Corralc and J. V. Calvetca, "Indirect model for roughness in rough honing processes based on artificial neural networks," *Precision Engineering*, pp. 1-9, 2015.
- [3] A. Yadollahi, E. Nazemi, A. Zolfaghari and A. M. Ajorloo, "Application of artificial neural network for predicting the optimal," *Progress in Nuclear Energy*, vol. 89, pp. 69-77, 2016.
- [4] S. Ozsahin, "Optimization of process parameters in oriented strand board," *Springer-Verlag Berlin Heidelberg*, vol. 71, p. 769-777, 2013.
- [5] D. J. Sarma and S. C. Sarma, "Neural Networks and their Applications in Industry," *Bulletin of Information Technology*, vol. 20, pp. 29-36, 2000.
- [6] neuralpower, "Integreat Electricity Demand and Price Forecasting," [Online]. Available: <http://www.neuralpower.com/technology>. [Accessed 7 October 2016].
- [7] P. SIB, S. A. JONES and P. SIDDARTH, "ANALYSIS OF DIFFERENT ACTIVATION FUNCTIONS USING BACK PROPAGATION NEURAL NETWORKS," *Journal of Theoretical and Applied Information Technology*, vol. 47, no. 3, pp. 1264-1268, 2013.
- [8] A. Bordes, L. Bottou and P. Gallinari, "SGD-QN: Careful Quasi-Newton Stochastic Gradient Descent," *Journal of Machine Learning Research*, vol. 10, pp. 1737-1754, 2009.
- [9] M. I. A. Lourakis, "A Brief Description of the Levenberg-Marquardt Algorithm Implemented," *Institute of Computer Science*, pp. 1-5, 2005.
- [10] D. Rasch, J. Pilz, R. Verdooren and A. Gebhardt, "Optimal Experimental Design with R," *Journal of Statistical Software*, vol. 43, 2011.
- [11] S. Prechadet and C. Luksiri, "Prediction of Silicon wafer Lapping Time by Artificial Neural network," *Engineering Journal Kasetsart*, vol. 77, pp. 1-11, 2011.

Single-carrier-based Pulsewidth Modulation Strategy for Grid-connected Three-level NPC Converter Based on Voltage-oriented Control

Watcharin Srirattanawichaikul, Suttichai Premrudeepreechacharn, Yuttana Kumsuwan

Department of Electrical Engineering,
Faculty of Engineering, Chiang Mai University
Chiang Mai, Thailand

watcharin.s@eng.cmu.ac.th, suttic@eng.cmu.ac.th, yt@eng.cmu.ac.th

Abstract—This paper presents a modified carrier-based pulsewidth modulation (PWM) strategy for the grid-connected three-level neutral-point-clamped (NPC) converter system. The gating signals are generated by comparing the single carrier signal with the modified modulating signals. The control method of the grid-connected system is applied for the voltage-oriented control scheme, which provides independent control active and reactive powers into the utility grid and maintain the dc-link voltage constant. The feasibility of the developed proposed modulation technique for the grid-connected three-level NPC converter system is confirmed by simulation and experiment results, which is validated the performance and effectiveness of the presented method.

Keywords—Three-level neutral-point-clamped voltage source converter; carrier-based pulsewidth modulation technique; grid-connected system; grid-connected control strategy; multilevel converter.

I. INTRODUCTION

Multilevel converter topologies have recently been extensively applied in high-power medium-voltage industrial applications. The advantages of these converters are higher quality output voltage waveforms, reduced output voltage and current harmonic distortions, and lower semiconductor voltage stress when compared with a standard two-level converter topology [1]. The most popular topology of multilevel converters is the three-level NPC converter. These converters play a pivotal role in high-power industrial applications such as composition of renewable energy sources, active-front-end converters for motor drive systems, grid-connected systems, and energy storage systems. Fig. 1 shows the equivalent circuit of the grid-connected three-level NPC converter. The control scheme of a grid-connected converter is usually providing control power factor, dc-link voltage regulation and low harmonic distortion of current [2]. Moreover, the modulation technique for three-level NPC converter should be designed the simple algorithm and processed very fast. Typically, the modulation technique for three-level NPC converter could be generally classified into two groups, which are carrier-based modulation technique and space vector modulation technique. Amongst these modulation techniques, the carrier-based

modulation technique has probably been the most popular due to its simplicity of implementation.

Several modulation techniques have been found in recent literatures to the grid-connected three-level NPC converter applications. In [3] was presented a novel modulation strategy for a three-level NPC converter. The proposed modulation strategy is provided by adding the minimum and maximum of the reference voltages to the output reference voltages, which is obtained from the modified modulation signals. The modulation strategy completely removes the low-frequency voltage oscillations that appear in the neutral-point voltage. In addition, this technique can be implemented with a very simple algorithm and processed very fast. Nevertheless, this technique is required two triangular carriers with modulation signals for generate the gate pulses. The single-carrier modulation technique for three-level NPC inverter in photovoltaic (PV) systems was presented in [4]. This technique can eliminate the leakage current through the common-mode voltage control system. It has a very simple structure. Although this method performs well, it requires a specific and modified modulation switching signals with analog circuits. This method increases the implementation cost and complexity. The direct power control has been developed for PV grid-connected system with three-level NPC converter [5]. In this method, the active and reactive powers are used control variables. It has demonstrated good dynamic performance of the grid-connected system.

Therefore, the main contribution of this paper is to present the superiority of modified modulation technique for the grid-connected three-level NPC converter system. This converter is operated on the voltage-oriented control to maintain a dc-link voltage constant and feed the active power into the utility grid. The paper is organized as follows. Section II gives configuration of the grid-connected three-level NPC converter system. A voltage-oriented control is used in this paper to control the grid-connected converter and the considerations required to implement the proposed modulation technique are discussed in Section III and IV, respectively. The simulation and experimental results which verify the proposed method are present in Section V. Finally, Section VI draws the conclusion.

II. CONFIGURATION OF THE GRID-CONNECTED THREE-LEVEL NPC CONVERTER SYSTEM

A. Description and Operation of Grid-connected Systems

Among the various multilevel converter topologies, the most popular topology in high power industrial applications is the three-level NPC converter. One of the advantages of this converter is that the power switches and the dc-link capacitors have to endure only one-half of the dc-link voltage. As a result, the converter can deal with double voltage and power value than in a standard two-level converter with the same switching frequency. Fig. 1 shows the simplified equivalent circuit of a grid-connected three-level NPC converter. The converter consists of twelve active switches and six anti-parallel diodes. The grid-side is connected using three inductors with loss resistor for inject current to cancel the harmonic component current. On the dc-link side of the converter, the dc-link voltage capacitor is split into two, providing a neutral point and must be regulated and balanced.

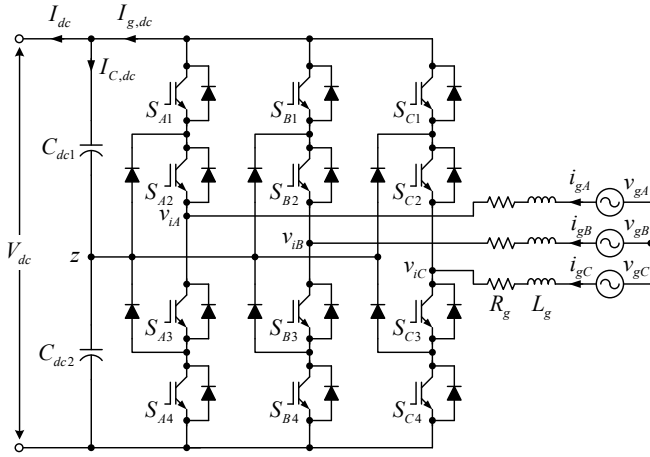


Fig. 1. Equivalent circuit of the grid-connected three-level NPC converter.

B. Dynamic Model of Grid-connected Systems

Considering the ac output from a converter in Fig. 1, assuming ideal commutation and neglecting the effect of harmonics, the voltage equations that model the grid-connected three-level NPC converter can be derived as follow:

$$\begin{cases} v_{gA} = R_g i_{gA} + L_g \frac{d}{dt} i_{gA} + v_{iA} \\ v_{gB} = R_g i_{gB} + L_g \frac{d}{dt} i_{gB} + v_{iB} \\ v_{gC} = R_g i_{gC} + L_g \frac{d}{dt} i_{gC} + v_{iC} \end{cases} \quad (1)$$

where v_{gA}, v_{gB}, v_{gC} are the phase grid voltages, v_{iA}, v_{iB}, v_{iC} are the phase grid-side converter voltages, i_{gA}, i_{gB}, i_{gC} are phase grid currents, R_g and L_g are the resistance and inductance of the utility grid.

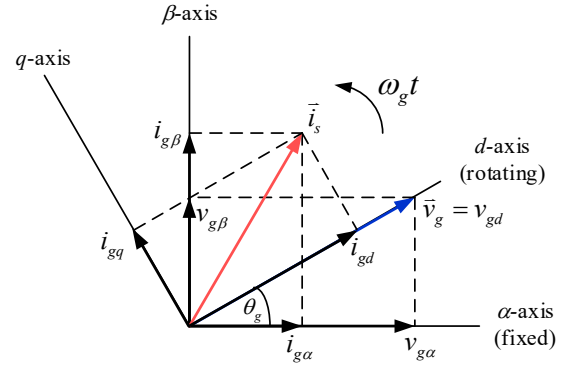


Fig. 2. Phasor diagram of the grid-connected three-level NPC converter.

A dynamic mathematical model of grid-side converter is developed in its original three-phase abc frame. This three-phase model is transformed into the dq rotating reference frame. From (1), the voltage equations of the grid-connected system on the rotating reference frame are depicted as follows:

$$\begin{cases} v_{gd} = R_g i_{gd} + L_g \frac{d}{dt} i_{gd} - \omega_g L_g i_{gq} + v_{id} \\ v_{gq} = R_g i_{gq} + L_g \frac{d}{dt} i_{gq} + \omega_g L_g i_{gd} + v_{iq} \end{cases} \quad (2)$$

where, v_{gd} and v_{gq} are the d -axis and q -axis grid voltages, v_{id} and v_{iq} are the d -axis and q -axis inverter voltages, i_{gd} and i_{gq} are the d -axis and q -axis grid currents, and ω_g is the electrical angular of the utility grid.

The phasor diagram for the vector control of the grid-connected converter is shown in Fig. 2. By placing the d -axis of the rotating reference frame on the utility grid voltage vector, v_{gq} and v_{gd} are set to zero and constant, respectively.

The equations of the active power P_g and reactive power Q_g in rotating reference frame, which is aligned in the utility grid, can be calculated as

$$\begin{cases} P_g = 1.5 v_{gd} i_{gd} \\ Q_g = -1.5 v_{gd} i_{gq} \end{cases} \quad (3)$$

From (3), the grid-connected control system can be produced active and reactive powers with the controlled d - q axis current components. The q -axis current component is set to variable for reactive power control. The dc power has to be equal to the active power flowing between the utility grid and the dc-link converter. Thus,

$$C_{dc} \frac{d}{dt} V_{dc} = I_{C,dc} = I_{g,dc} - I_{dc} \quad (4)$$

where V_{dc} is the dc-link voltage, I_{dc} is the current between the dc-link and the rotor-side converter, $I_{g,dc}$ is the current between the dc-link and the grid-side converter, and C_{dc} is the dc-link capacitor.

III. CONTROL SYSTEM OF GRID-CONNECTED THREE-LEVEL NPC CONVERTERS

To illustrate the control system of the voltage-oriented control method for the grid-connected three-level NPC converter system is presented in this section. The purpose of the grid-connected system is to present the modified modulation technique in generated the gating signals for the grid-connected three-level NPC converter system as shown in Fig. 3. The three-level NPC converter is operated on the voltage-oriented control to maintain a dc-link voltage constant and feed the active power into the utility grid. Traditionally, the grid-connected converter can be used to produce active and reactive powers with the controlled d - q axis current components, respectively.

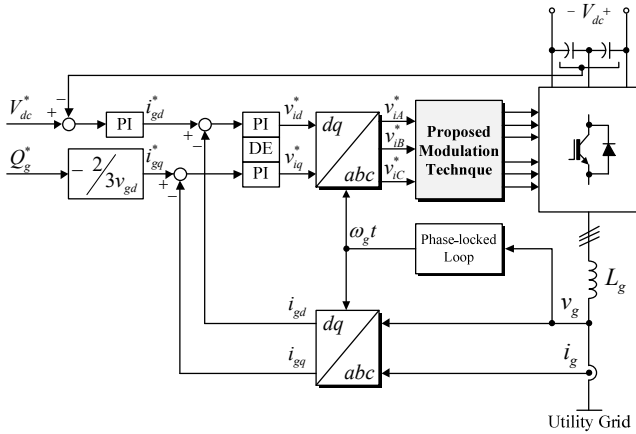


Fig. 3. Block diagram of the proposed grid-connected three-level NPC converter system and controller using the proposed modulation technique.

For the grid-connected voltage-oriented control, a complete control scheme of the grid-connected three-level NPC converter is indicated in Fig. 3. This scheme has three control loops, one external loop to control the dc-link voltage and two internal loops to regulate the d - q current components, the d -axis current component is utilized to regulate the dc-link voltage and the q -axis current component is utilized to control the reactive power. The output active power and the power factor of the utility grid can be controlled by changing d - and q -axis current components, respectively.

In the control scheme, the dc-link voltage controller is the outer loop, while the current controller is the inner loop. The main objective of the control scheme is to regulate dc-link voltage V_{dc} to follow the reference value V_{dc}^* , while the grid current is sinusoidal shape and either in-phase or out of phase with the utility grid. The dc-link voltage error is delivered to proportional-integral (PI) dc-link voltage controller, which generates the reference value of the current in d -axis component i_{gd}^* . To achieve the unity power factor condition in the grid-side converter, the referenced current value of q -axis component i_{gq}^* is set to zero, $Q_g^* = 0$ VAR.

The current errors are delivered to PI current controllers that generate the inverter voltage references. The compensations correspond to the inverter voltage references

and decoupling terms (DE) of the current components. Therefore, the inverter voltage references v_{id}^*, v_{iq}^* can be given by:

$$\begin{cases} v_{id}^* = v_{Lgd}^* + \omega_g L_g i_{gq}^* + v_{gd} \\ v_{iq}^* = v_{Lgq}^* - \omega_g L_g i_{gd}^* \end{cases} \quad (5)$$

After transformation into the three-phase reference frame, the reference voltage $v_{iA}^*, v_{iB}^*, v_{iC}^*$ are delivered to the proposed modulation technique which generates switching signals for the three-level NPC converter.

A. Design of dc-link voltage control

The dc-link voltage controller is used to generate the reference current in d -axis component for the current controller. The aim of this controller is to keep the dc voltage constant on the dc-link, which is changed according to balance of power replaced by the converter. The design of the dc-link voltage controller has been designed to achieve short settling time and fast correction of the error. The dc power has to be equal to the active power, $P_{dc} = P_g$, flowing between the utility grid and the dc-link inverter. The expression for the average dc-link grid-side current $I_{g,dc}$ is given by

$$I_{g,dc} = \frac{3}{2} \frac{v_{gd} i_{gd}}{V_{dc}} \quad (6)$$

Substituting (6) into (4), the differential equation of the dc-link voltage is expressed as

$$\frac{d}{dt} V_{dc} = \frac{3}{2} \frac{v_{gd} i_{gd}}{V_{dc} C_{dc}} - I_{dc} \quad (7)$$

By Laplace transform in (7), the closed-loop transfer function of the dc-link voltage controller, obtained from Fig. 4, can be written as

$$\frac{V_{dc}(s)}{V_{dc}^*(s)} = \frac{\frac{3}{2} \frac{V_{gd}}{V_{dc} C_{dc}} (k_{pv} s + k_{iv})}{s^2 + \frac{3}{2} \frac{V_{gd}}{V_{dc} C_{dc}} k_{pv} s + \frac{3}{2} \frac{V_{gd}}{V_{dc} C_{dc}} k_{iv}} \quad (8)$$

Therefore, the parameters of PI controller of dc-link voltage control can be calculated as

$$\begin{cases} k_{pv} = \frac{2}{3} \frac{V_{dc}}{V_{gd}} 2\xi \omega_{nv} C_{dc} \\ k_{iv} = \frac{2}{3} \frac{V_{dc}}{V_{gd}} \omega_{nv}^2 C_{dc} \end{cases} \quad (9)$$

where k_{pv} and k_{iv} are the proportional and integral parameters of the dc-link voltage control, respectively, ω_{nv} is the natural angular frequency of dc-link voltage control, and ξ is the damping ratio.

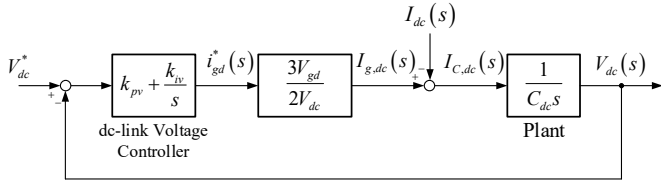


Fig. 4. Block diagram of the dc-link voltage control.

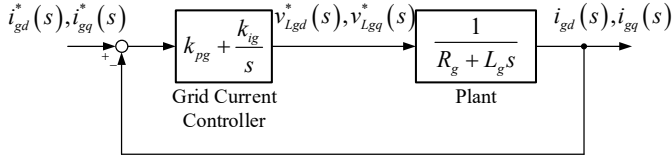


Fig. 5. Block diagram of the grid current control.

B. Design of grid-connected current control

The d -axis and q -axis current controllers have the same dynamic controls. Considering (2) with the d -axis of rotating reference frame aligned to the utility grid voltage vector, the grid-side inductance voltage references v_{Lgd}^* , v_{Lgq}^* are specified as

$$\begin{cases} v_{Lgd}^* = R_g i_{gd} + L_g \frac{d}{dt} i_{gd} \\ v_{Lgq}^* = R_g i_{gq} + L_g \frac{d}{dt} i_{gq} \end{cases} \quad (10)$$

By Laplace transform the voltage equations in (10), the transfer function of the grid current loop can be written as

$$\frac{i_{gd}(s)}{v_{Lgd}^*(s)} = \frac{i_{gq}(s)}{v_{Lgq}^*(s)} = \frac{1}{R_g + L_g s} \quad (11)$$

Equation (11) shows that the relationship between grid-side current and the grid inductance voltage is equivalent to a first order system, which is suitable for both dq current loops. The PI controller for achieving good performance of tracking the dq reference current signals can be synthesized for the desired closed-loop transfer function. Therefore, the closed-loop transfer function of the current controller in Fig. 5 can be written as

$$\frac{i_{gd}^*(s)}{i_{gd}(s)} = \frac{i_{gq}^*(s)}{i_{gq}(s)} = \frac{k_{pi}s + k_{ii}}{s^2 + \frac{R_g + k_{pi}}{L_g}s + \frac{k_{ii}}{L_g}} \quad (12)$$

From the general form of the characteristic equation in (12), the parameters of PI controller of grid current control can be calculated as

$$\begin{cases} k_{pi} = 2\xi\omega_m L_g - R_g \\ k_{ii} = \omega_m^2 L_g \end{cases} \quad (13)$$

where k_{pi} and k_{ii} are the proportional and integral parameters of the grid control, respectively, and ω_m is the natural angular frequency of grid current control.

IV. PROPOSED PULSEWIDTH MODULATION STRATEGY FOR THREE-LEVEL NPC CONVERTER

The traditional carrier-based modulation technique of the three-level NPC converter uses the sinusoidal/non-sinusoidal modulation techniques, which compared with two triangular carrier signals [6]. The three-phase sinusoidal reference signals $v_{A,B,C}^*$ can be given by

$$\begin{cases} v_A^* = m_a \cos(\omega_s t) \\ v_B^* = m_a \cos(\omega_s t - 2/3\pi) \\ v_C^* = m_a \cos(\omega_s t + 2/3\pi) \end{cases} \quad (14)$$

where m_a is the modulation index and $\omega_s t$ is the phase angle (ω_s is the angular frequency, $2\pi f_s$).

The proposed modulation technique is modified the sinusoidal modulating signal that uses the effective three-phase sinusoidal reference signal and the maximum and minimum of the three reference signals. This technique is based on only single triangular carrier signal for generated the gating pulses to the three-level converter. The general form of the modified modulation reference signal equation for the proposed modulation technique is defined as

$$\begin{cases} v_{AM}^* = v_{AP}^* + v_{AN}^* \\ v_{BM}^* = v_{BP}^* + v_{BN}^* \\ v_{CM}^* = v_{CP}^* + v_{CN}^* \end{cases} \quad (15)$$

where, $v_{ABC,M}^*$ is the modified modulation reference signals and $v_{ABC,P}^*$, $v_{ABC,N}^*$ are the positive and negative reference signals.

The positive reference signals take the minimum of the three-reference signals and subtract this value from each of the three-phase sinusoidal reference signals, which can be expressed as,

$$\begin{cases} v_{AP}^* = \frac{v_A^* - \min(v_A^*, v_B^*, v_C^*)}{2} \\ v_{BP}^* = \frac{v_B^* - \min(v_A^*, v_B^*, v_C^*)}{2} \\ v_{CP}^* = \frac{v_C^* - \min(v_A^*, v_B^*, v_C^*)}{2} \end{cases} \quad (16)$$

Similar to (16), the negative reference signals take the maximum of the three-reference voltages and subtract this value from each of the three-phase sinusoidal reference signals,

$$\begin{cases} v_{AN}^* = \frac{v_A^* - \max(v_A^*, v_B^*, v_C^*)}{2} + 1 \\ v_{BN}^* = \frac{v_B^* - \max(v_A^*, v_B^*, v_C^*)}{2} + 1 \\ v_{CN}^* = \frac{v_C^* - \max(v_A^*, v_B^*, v_C^*)}{2} + 1 \end{cases} \quad (17)$$

The proposed modulation technique is shown in block diagram of Fig. 6, where the three-phase sinusoidal reference signals v_{ABC}^* to generated the modified modulation reference signals $v_{ABC,P}^*, v_{ABC,N}^*$. It can be seen that the modified modulation reference signals are compared with the single triangular carrier signal to generate the logic 0 or 1 signals of the $S_{A,1-4}, S_{B,1-4}, S_{C,1-4}$. The logic of gate pulses is very simple as follows: if $v_{ABC,P}^* \geq v_{tri} \Rightarrow S_{ABC,1} = \text{ON}, S_{ABC,3} = \text{OFF}$ and if $v_{ABC,N}^* \geq v_{tri} \Rightarrow S_{ABC,2} = \text{ON}, S_{ABC,4} = \text{OFF}$. Since the inner gating pulses $S_{ABC,3}$ operate complementary with $S_{ABC,1}$ and $S_{ABC,4}$ operate complementary with $S_{ABC,2}$. The practical implementation method is proposed modulation technique using offset reference signal concept. The main point of the proposed technique is used only single triangular carrier signals for generated the specified gating signals for three-level NPC converter.

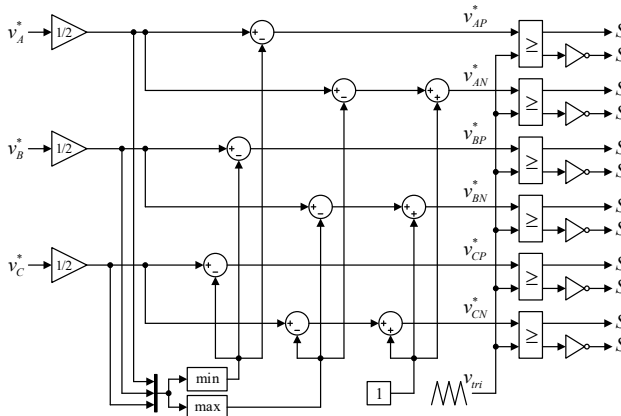


Fig. 6. Block diagram of the proposed modulation technique for three-level NPC converter.

V. RESULTS AND DISCUSSION

In this section, simulation and experimental system was built, and various results are presented. To evaluate the performance of the proposed system, simulations are performed by using Matlab/Simulink software. The operation of grid-connected three-level NPC converter is experimented to evaluate the proposed modulation technique, which is represented by the block diagram as shown in Fig. 7. The three-level NPC converter prototype is realized using SEMIKRON SKM50GB123D IGBT modules and SEMIKRON SKKD42F12 diode modules. Each leg of converter is equipped with the two switch IGBT modules and

the single clamped diode module. A three-level NPC converter is connected to utility grid with the 380V, 50Hz through the three-phase transformer (turn ratio 1:4). A dc power supply rated at 5kW is connected to the dc-link. The nominal converter dc-link voltage is controlled at 180 V, the switching frequency of the converter is 2.5 kHz, the dc-link capacitors are 3,300 μF each, and the low-pass filter of grid is 12 mH. The proposed control method is implemented in a ds1104 real-time control board, which acquires the dc and ac voltages and currents. The digital platform sends the gate signals directly to the gate driver circuit of the three-level NPC converter.

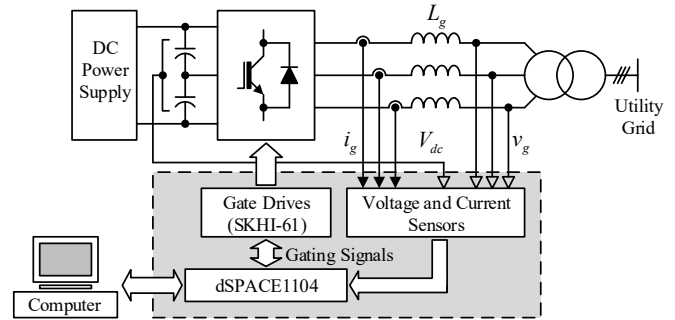


Fig. 7. Configuration of the experimental set-up.

A. Simulation results

The simulated design is carried out to verify the validity of the proposed system. The modified modulating signals of the proposed technique are given in Fig. 8. In Fig. 8 (top), the sinusoidal modulating signals v_A^*, v_B^*, v_C^* are used to generate the modified modulating signals as shown in Fig. 8 (middle). From these figures, it can be seen that the waveforms of the modified modulating signals are compared with the single triangular carrier signal where the amplitude of the modulation index is defined as the relation between the peak amplitude of triangular carrier signal. The modulated gating signals can be generated using proposed the modulation technique for three-level NPC converter as shown in Fig. 8 (bottom).

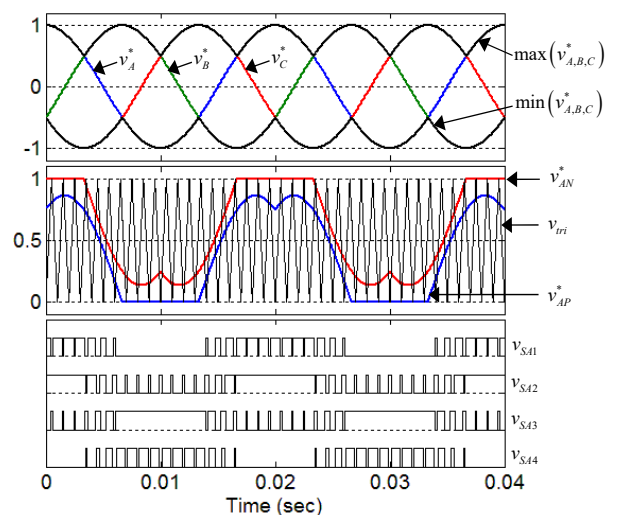


Fig. 8. Single triangular carrier-based modulation technique for generating gate signals.

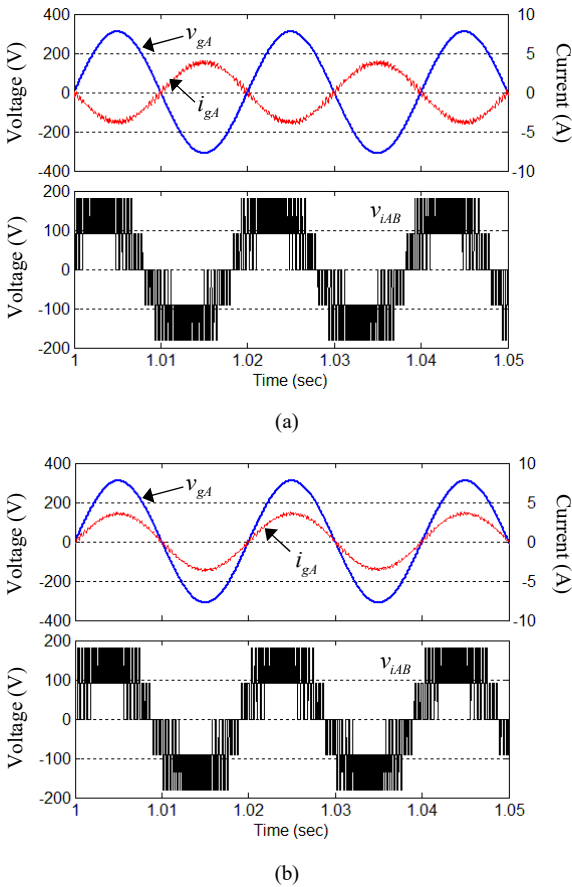


Fig. 9. Simulation results of the proposed modulation technique for grid-connected three-level NPC converter in unity power factor operation. (a) Inverting mode. (b) Rectifying mode.

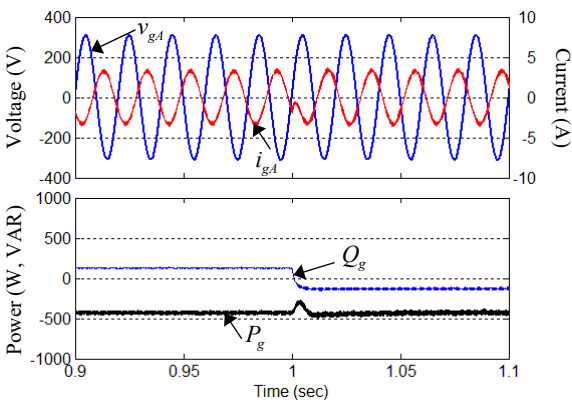


Fig. 10. Simulation results of the proposed modulation technique for grid-connected three-level NPC converter of dynamic response operation in the inverting mode.

Fig. 9 (a) also shows the voltage and the current waveforms of the converter operating in the inverting mode. In this condition, the active power flows from the dc-link side into the utility grid. The phase displacement between the grid-connected phase grid voltage and current of converter is out of phase and the dc-link voltage is kept constant. Similarly, Fig. 9 (b) shows the simulated waveform by the converter for operation in the rectifying mode. In this operation mode, the

active power flows into the dc-link, with in phase displacement between the grid-connected grid voltage and the grid current.

As discussed earlier, the power factor of the system can be controlled by adjusting the reference of the reactive power. As can be seen from Fig. 10, the dynamic response of the converter to a step changed in reactive power reference control with active power flowing from the dc-link into the grid. The reactive power is stepped from +120 VAR to -120 VAR and the active power is kept constant. It can be seen that the grid current of converter can operate under the leading and lagging power factor condition with the performance of the dc-link voltage constant.

B. Experimental results

The experimental results of the proposed prototype-based laboratory prototype have been presented to demonstrate the proposed system in practice as shown in Figs. 11 and 13. Fig. 11 (a) and (b) show measured waveforms of the proposed modified reference signals and gating signals for power switches in phase A at the modulation index of 0.8. The references can share single triangular carrier signal. Therefore, the modulation signals for the power switches located in phase B and C can be obtained by $\pm 120^\circ$ phase-shifting, respectively.

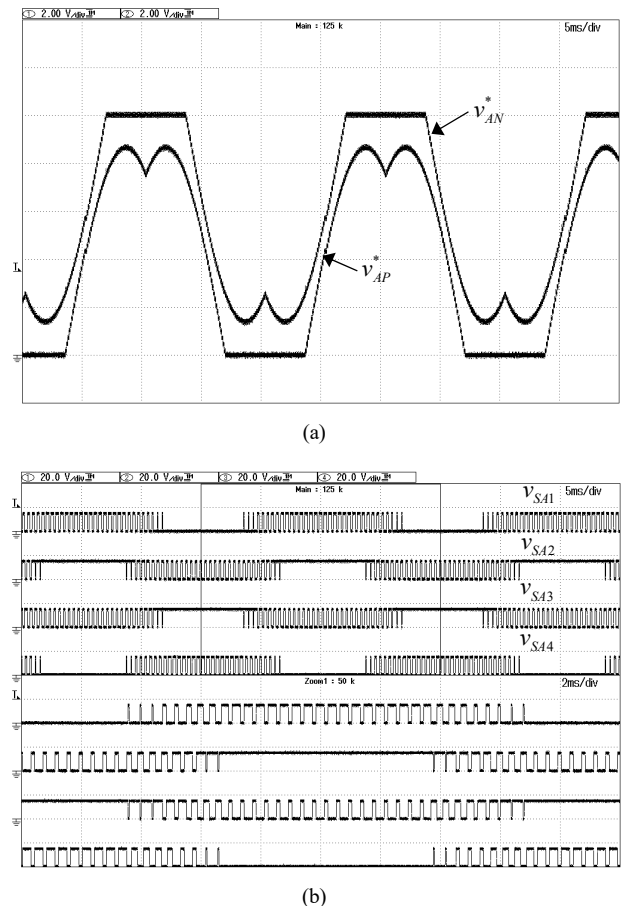
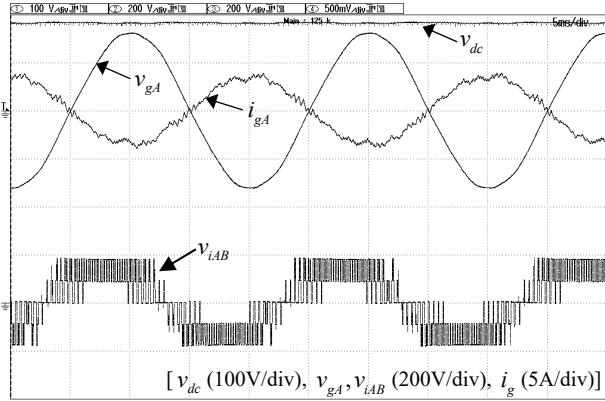
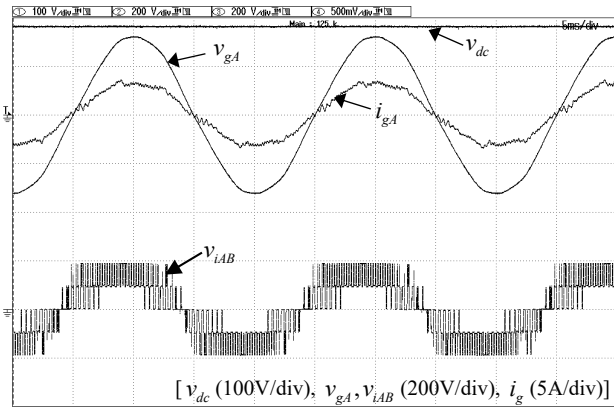


Fig. 11. Experimental results of the proposed modulation technique in phase A. (a) Modulation reference signals. (b) Gating signals.



(a)



(b)

Fig. 12. Experimental results of the proposed modulation technique for grid-connected three-level NPC converter in unity power factor operation. (a) Inverting mode. (b) Rectifying mode.

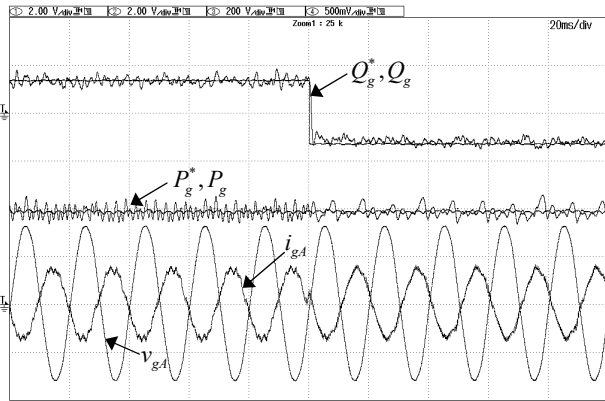


Fig. 13. Experimental results of the proposed modulation technique for grid-connected three-level NPC converter of dynamic response operation in the inverting mode.

Fig. 12 (a) shows dc-link voltage v_{dc} , the grid phase voltage v_{gA} and the current i_{gA} in phase A, and the line-to-line voltage of the three-level NPC converter v_{iAB} at unity power factor operation. In this condition, the active power flows from the dc-link into the utility grid. The reference of the reactive power Q_g^* is controlled to zero. It can be seen that the grid phase

current is out of phase with the grid phase voltage. It guarantees a null reactive power on the utility grid. Similarly, Fig. 12 (b) also shows experimented waveforms in the rectifying mode. In this operation mode, the active power flows into the dc-link, with in phase displacement between the grid-connected grid voltage and the grid current.

The dynamic response of the voltage-oriented control technique to a step change in the reactive power reference with active power flowing from the dc-link into the utility grid is shown in Fig. 13. The reactive power reference is step changed from -120 to +120 VAR and the active power is kept constant at -420 W. It can be seen that the grid-side converter can operate under the leading and lagging power factor condition with keeping the dc-link voltage constant. There are not overshoot of either the grid current or the active and reactive powers.

VI. CONCLUSION

This paper proposed a modulation strategy for the grid-connected three-level NPC converter system. The proposed technique is employed only single triangular carrier signal for generated the gating signals in the converter and significantly simplifies the modulation technique. The advantages are simple modulation algorithm, reduced capacitor voltage ripple, lower switching frequencies, and easy hardware implementation. This paper has also proposed the control method of voltage-oriented control for the grid-connected system. The objective of the grid-side converter control is to maintain the dc-link voltage and independently control active and reactive power flow. The experimental result confirms that proposed technique is able to achieve good dynamic responses and high accuracy in active and reactive power controls.

ACKNOWLEDGMENT

The authors would like to thank the Faculty of Engineering, Chiang Mai University.

REFERENCES

- [1] J. Rodríguez, J. Lai, and F. Peng, "Multilevel inverters: A survey of topologies, controls and applications," *IEEE Trans. Ind. Electron.*, vol. 49, no. 4, pp. 724-738, Aug. 2002.
- [2] F. Blaabjerg, R. Teodorescu, M. Liserre, and A. V. Timbus, "Overview of control and grid synchronization for distributed power generation systems," *IEEE Trans. Ind. Electron.*, vol. 53, no. 5, pp. 1398-1409, Oct. 2006.
- [3] J. Pou, J. Zaragoza, P. Rodriguez, S. Ceballos, V. M. Sala, R. P. Burgos, and D. Boroyevich, "Fast-Processing Modulation Strategy for the Neutral-Point-Clamped Converter with Total Elimination of Low-Frequency Voltage Oscillations in the Neutral Point," *IEEE Trans. Ind. Electron.*, vol. 54, no. 4, pp. 2288-2294, Aug. 2007.
- [4] X. Guo, M. C. Cavalcanti, A. M. Farias, and J. M. Guerrero, "Single-carrier modulation for neutral-point-clamped inverters in three-phase transformerless photovoltaic systems," *IEEE Trans. Power Electron.*, vol. 28, no. 6, pp. 2635-2637, June 2013.
- [5] J. A. Martinez, J. E. Garcia, and S. Arnaltes, "Direct power control of grid connected PV systems with three-level NPC converter," *Solar Energy*, vol. 84, pp. 1175-1186, 2010.
- [6] R. M. Tallam, R. Naik, and T. A. Nondahl, "A carrierbased PWM scheme for neutral-point voltage balancing in three-level inverters," *IEEE Trans. Ind. Appl.*, vol. 41, no. 6, pp. 1734-1743, Nov./Dec. 2007.

Design and Analysis of a Single-Phase Hybrid Renewable Energy System

Jirasak Songboonkaew
 Department of Electrical Engineering,
 Faculty of Engineering,
 Thonburi University, Thailand
 E-mail address: jirasak1163@gmail.com

Akeratana Noppakant
 Department of Electrical Engineering,
 Faculty of Engineering,
 Thonburi University, Thailand
 E-mail address: eg1322@gmail.com

Abstract— This paper presents the design and analysis the energy form a single-phase hybrid system which is connected to a commercial power system. The proposed single-phase hybrid system is used the main power to load and a commercial power system is used for stability of system. The principle of this a single-phase hybrid system was using 8 sets of 310 Watts photovoltaic (PV) panels, Control charge and synchronize the power with 4 kw hybrid inverter, the power was stored into 4 set of 12 V 200 Ah battery connected in series to supply to main distribution line form a commercial power system for 24 hours. The results of this a single-phase hybrid system, the peak period is 12 A.M.- 1 P.M. that can generate maximum power and the energy for a day from PV panels is 9.7 kWh, the all energy from system to load are 9.5 kWh, the all energy from a commercial power system is 2.3 kWh.

Keywords— Single-Phase, Hybrid System, PV panel, Renewable Energy

I. INTRODUCTION

Renewable Energy Sources are energy sources which are not destroyed when fossil energy is harnessed. Using of renewable energy requires technologies that harness natural phenomena, such as solar, wind, water flow, and biological processes. Amongst the renewable energy sources, there has been a lot of development in the technology for harnessing renewable energy from the solar energy. Many countries are pursuing the option solar energy conversion systems; in an effort to minimize their dependence on fossil-based non renewable fuels [1] Therefore, The global solar energy demand is increasing. While, The global solar energy demand is increasing. While, the photovoltaic (PV) business has strong and room for significant growth [2-3]. The PV business calls for high-reliability, high-efficiency, low-cost and small-size [4-5] for commercial solar energy systems can be employed for producing large amounts of power at a low price. Procreation of solar is an extremely unpredictable factor since at some time it can below above working-point on varying depending on the natural conditions such as shadows cast by clouds, rains, objects, trees, etc..

Thus, discontinuous solar energy make them unreliable sources of energy. Therefore, PV hybrid system and commercial power system can swell up system efficiency and reliability significantly. When one source is unavailable or insufficient in recompense the load demands, the another energy source can be compensated the load demand.

A typical PV stand-alone systems have been using for hybrid system. According, a PV stand-alone systems are consisted of battery storage, controller and PV generator. The energy of battery is used to maintaining system voltage stability and operations during night or cloudy weather. The controller is used to regulate the battery charge and the DC/AC inverter is used if the load is AC [6-7]. For hybrid system, the inverter is included of a controller and a bidirectional inverter which will be called hybrid inverter.

In this paper, the proposed single-phase hybrid system is composed of two power sources namely; a PV stand-alone system is coupled to a hybrid inverter, a battery and a selector switch, a commercial power system is coupled to Auto Transfer Switch (ATS). The control unit is acted to send control signal to individual equipment of a hybrid inverter and monitor power status via LCD display. However, manual setting of ATS operating is also possible when the PV hybrid system is problem operating, as shown in Fig 1.

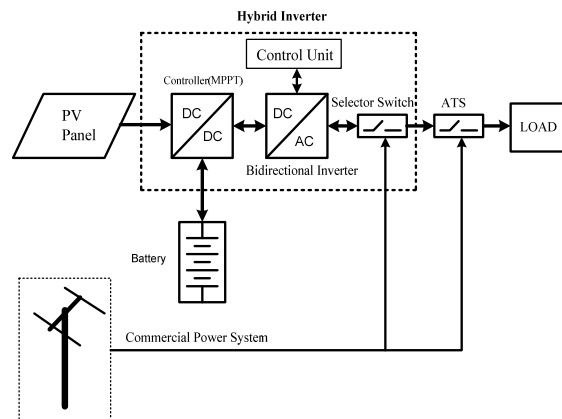


Fig. 1. Block diagram of the proposed hybrid system

II. HYBRID SYSTEM

From Fig.1, The operation steps of proposed single-phase hybrid system are as follow.

- When the battery capacity is sufficient: The power source from the PV panel will be supplied to load via a control charger, a bidirectional inverter and a selector switch. If power generated by PV panel is insufficient, Power source from the battery will be supplied to load.
- When the remaining battery capacity is insufficient: Power generated by PV panel will be supplied to load and the remaining power of PV panel is charged the battery through a control charger, following the command from the control unit.
- When power generated by PV panel and the battery capacity are insufficient: The power source from a commercial power system will be supplied to load and will be charged the battery, following the command from the control unit.

A. Design for Components of Single PhaseHybrid System

The proposed single-phase hybrid system has been designed with principles that its must have similar requirement compare to PV stand-alone systems, it was installed and test location is located at Dansingkhon School Prachuapkhirihaan province of Thailand. From test location, The PV hybrid system is supplied to maximum power as 2,437 W and maximum energy of each day as 6,479 Wh. Therefore, it has been designed for maximum load which result from calculation respectively.

From the maximum power, size of hybrid inverter can be calculated by equation (2)

$$P_{hyinverter} = P_{ac} \times 1.25 \quad (1)$$

Where: $P_{hyinverter}$ is power of hybrid inverter(W)

P_{ac} is maximum power of load(W)

From equation (1), size of hybrid inverter must be higher than 3,046 W, Thus, the proposed single-phase hybrid system contains inverter size of 4000 W, voltage system is 48 V and maximum current of charger controller is 40 A. From the characteristic of the hybrid inverter, the maximum DC voltage applied to the hybrid inverter is 145 V.

Size of PV panels are calculated by taking maximum energy of the system, efficiency of equipment and Peak Sun hour (PSH) into consideration. Efficiency has been calculated in terms of power loss and over size factor which are 1.73. Peak sun hour in area is approximate 4.54 hours. Hence, the power of PV panel can be calculated by equation (2) [8]

$$P_{pv} = \frac{W_s \times 1.73}{PHS} \quad (2)$$

Where: P_{pv} is PV panel nominal peak power (W_P)

W_s is maximum energy for a day (Wh)

PHS is peak sun hour (hr)

From equation (2), size of PV panel must not be lower than 2,460 W; Hence, the proposed single-phase hybrid system is composed of eight 310 W_P polycrystalline panels. From the characteristic of PV panel, the maximum open circuit voltage of each PV panel is 38.5 V and short circuit current is 9.43 A. Hence, the number of PV panel in series can be calculated by equation (3)

$$N_{Series} = \frac{V_{DCmaxinverter}}{V_{OCmax}} \quad (3)$$

Where: N_{Series} is number of PV panels in series (module)

$V_{DCmaxinverter}$ is maximum DC voltage of hybrid inverter(V)

V_{OCmax} is maximum open circuit voltage of PV panel (V)

From equation (3), number of modules in series must not be higher than 3 modules. Thus, the single-phase hybrid system is selected for 2 modules. The number of PV panels in parallel can be calculated by equation (4)

$$N_{Parallel} = \frac{I_{DCmaxcharger}}{I_{SC}} \quad (4)$$

Where: $N_{Parallel}$ is number of PV panels in parallel (string)

$I_{DCmaxcharger}$ is maximum DC current charger of hybrid inverter(A)

I_{SC} is short circuit current of PV panel (A)

From equation (4), number of strings in parallel must not be higher than 4 strings. Thus, the single-phase hybrid system is composed for 4 strings. Therefore, the peak power of PV panels obtain as 310 W_P .

Battery size can be obtained by calculated capacity from equation (5)

$$BC = \frac{W_s}{V_{system} \times DOD} \quad (5)$$

Where: BC is battery capacity (Ah)

DOD is depth of discharge for battery

From equation (5), capacity of battery must not be lower than 156 Ah. Thus, the single-phase hybrid system contains capacity of battery as 200 Ah (BC_{System}), voltage of battery is 12 V. From capacity of battery, it can be calculated series and parallel of batteries by equation(6) and equation(7) respectively.

$$B_{Series} = \frac{V_{System}}{V_{battery}} \quad (6)$$

Where: B_{Series} is number of batteries in series (Ah)
 $V_{battery}$ is voltage of battery(V)

$$B_{Parallel} = \frac{BC}{BC_{System}} \quad (7)$$

Where: $B_{Parallel}$ is number of batteries in parallel (Ah)
 BC_{System} is capacity of battery for system(Ah)

From calculation, number of batteries in series must be as 4 batteries and number of batteries in parallel must be as 1 battery. Hence, the proposed single-phase hybrid system is composed of 4 batteries for battery in series.

B. System wiring sizing

Cable size is peculiarly important for battery cables, PV panel cables and load cables. Voltage drops through incorrectly of cables are one of the most common reasons for low voltage (12 V/24 V/48 V) system faults. If the cables are far too small, it can be very dangerous as the cable will heat up and potentially cause a fire [9-10]. Therefore, the design of cables are important for single-phase hybrid system.

In DC side of the hybrid system, from the PV panels side to the single-phase hybrid inverter, calculate the maximum DC system voltage which will not exceed the single-phase hybrid inverter maximum DC voltage. The maximum DC system voltage can be calculated by equation (8).

$$V_{DCmax} = V_{OCmax} \times N_{Series} \times T_{factor} \quad (8)$$

Where: V_{DCmax} is maximum DC voltage (V)
 T_{factor} is temperature correction factor (is 1.14)

The maximum DC voltage from calculation by equation (8) is 88 V which is lower than 120 V. Thus, this hybrid system is considered voltage drop in cable which must not be higher than 3 %. In the PV panels circuit, the maximum DC current can be calculated by equation (9).

$$I_{DCmax} = N_{Parallel} \times I_{SC} \quad (9)$$

Where: I_{DCmax} is maximum DC current (A)

From equation (9), the maximum DC current in cable is 37.72 A. Because PV system currents are considered continuous. Thus, the maximum DC current calculated as per standard must be multiplied by 125 % to calculate the maximum continuous current. Therefore, the maximum continuous current in cable obtain as 47.15 A. From the maximum continuous current, the cable size is determined from standard as 6 sq.mm of PV-1F type. From the maximum DC voltage, the voltage drop in cable can be calculated by equation (10).

$$V_D = I_{DCmax} \times \text{Resistance of cable} \quad (10)$$

From the cable size, resistance of cable is 3.39 Ω/km which this cable is used 15 m length. So resistance of cable is determined as 0.051 Ω . From equation (10), the voltage drop in cable is 1.91 V which has lower than 3 %. For low voltage battery cables, the cable size is determined from standard as 6 sq.mm of PV-1F type. The voltage drop in cable can be calculated by equation (10).

C. Protection Equipment of Single-Phase Hybrid System

In DC side of the single-phase hybrid system, DC-Circuit Breaker size is determined from the maximum continuous current which is used as 60 AT. This hybrid system is used surge protection device (SPD) for protect electrical equipment from over-voltage transients caused by external (lightning) or internal (switching) events.

III. EXPERIMENTAL RESULTS

Experiment using designed of the prototype hybrid system has been carried out in order to evaluate the performance of photovoltaic system and energy storage system throughout the day, electric parameters such as voltage, current and power in one day with one-hour interval from 6.00 A.M. to 6.00 P.M. has been collected from two measurement points using power meter. Measurement points are depicted in Fig. 2; measurement point 1 is located after photovoltaic panels, measurement point 2 is located before batteries, measurement point 3 is located after a commercial power system and measurement point 4 is located before to load.

Results from measurement point 1 are shown in Fig. 3. It can be seen that in period of 6.00 A.M. - 7.00 A.M., solar radiation are low which resulted in low power. The peak period is 12.00 A.M that can generate maximum power and they steadily decrease until 6.00 P.M. The result has indicated that power generated from PV panels depend on solar radiation. The energy for a day from PV panels is 9.7 kWh.

Results from measurement point 2 are shown in Fig. 4. It can be seen that in period of 6.00 A.M. - 8.00 A.M.

and in period of 3.00 P.M. - 6.00 P.M. ; The power of batteries is discharged to the hybrid system for to load. The energy from batteries to the load in this period is 1.1 kWh. In period of 9.00 A.M. - 2.00 P.M., The batteries are charged from charger controller of hybrid inverter.

The energy for charger to batteries in this period is 2.4 kWh.

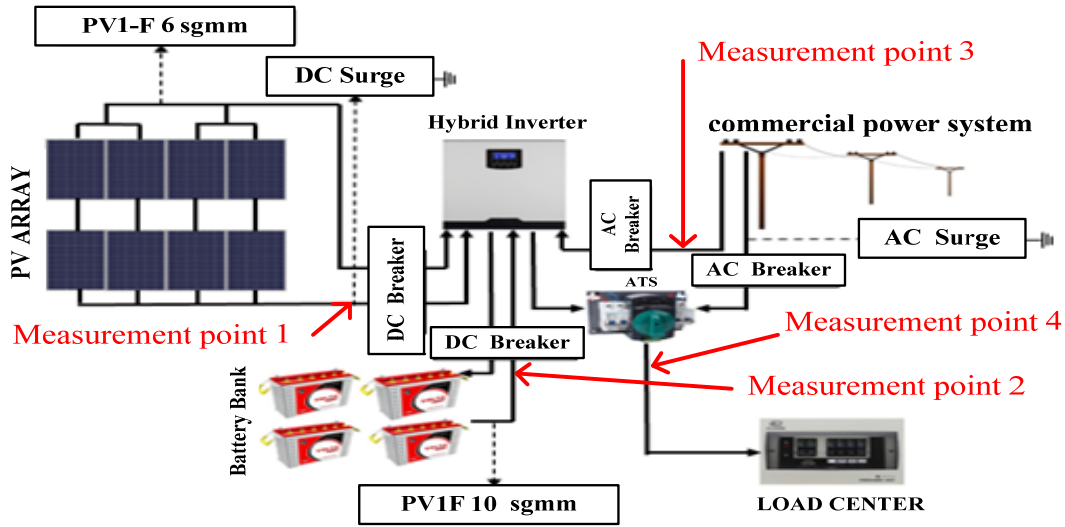


Fig. 2. The proposed hybrid system

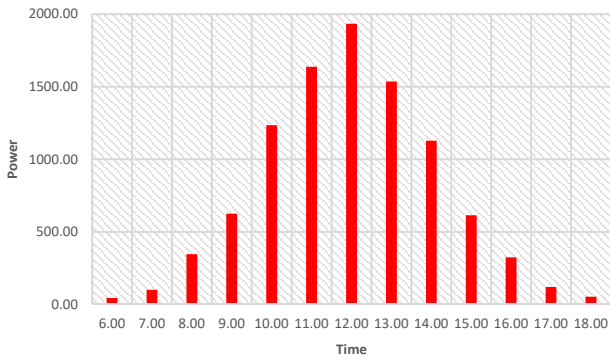


Fig. 3. The power of PV panels

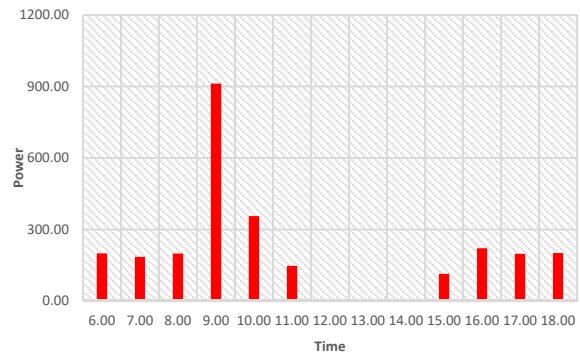


Fig. 5. The power of a commercial power system

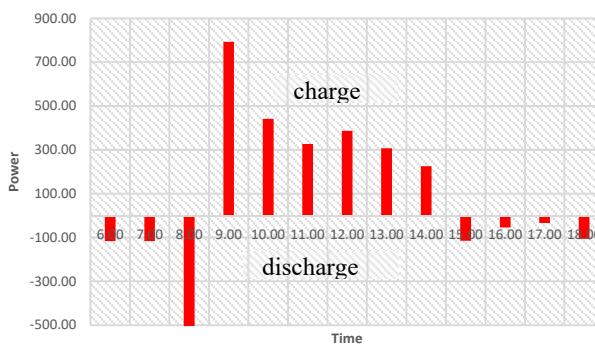


Fig. 4. The power of batteries

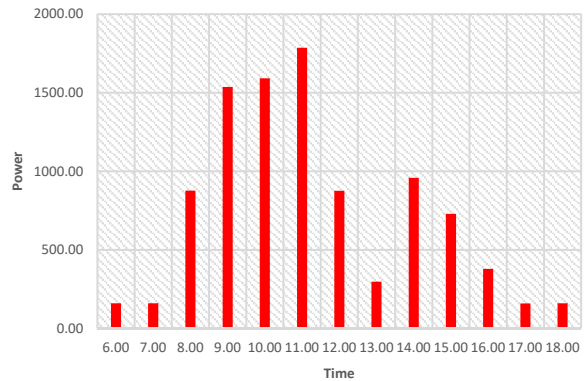


Fig. 6. The power of load

Results from measurement point 3 are shown in Fig. 5. It can be seen that in period of 6.00 A.M. - 11.00 A.M. and in period of 3.00 P.M. - 6.00 P.M. , the power source from a commercial power system is supplied to load. The all energy from a commercial power system to load are 2.3 kWh.

Results from measurement point 4 are shown in Fig. 6. It can be seen that in period of 6.00 A.M. - 6.00 P.M.: The power source is supplied to load and The all energy from system to load are 9.5 kWh.

IV CONCLUSIONS

This paper has presented design and analysis of single-phase hybrid system. The performance of proposed system has been evaluated using power from PV panels and the energy storage device throughout the day. The results have indicated that power from PV panels mainly depended on solar irradiation which the main power for system. In energy storage part, the batteries are charged and discharged the energy according period. In a commercial power system, it is used spare energy for system.

ACKNOWLEDGMENT

The authors are obtained financial support for this research from Thonburi University.

REFERENCES

- [1] Sajib Chakraborty¹, S M Salim Reza² and W ahidul Hasan³, "Design and Analysis of Hybrid Solar-Wind Energy System Using CUK & SEPIC Converters for Grid Connected Inverter Application" The 11 the IEEE International Conference on Power Electronics and Drive Systems. 2015, pp 278-283.
- [2] "Global Market Outlook for Photovoltaics 2013-2017," European Photovoltaic Industry Association, 2013.
- [3] Y. Tang, J. Wei and S. Xie, "Grid-tied photovoltaic system with series Z-source inverter," *IET Renew. Power Gener.*, vol. 7, no. 3, pp. 275-283, May. 2013.
- [4] B. Petroleum, "BP Statistical Review of World Energy 2015," ed: London, 2015.
- [5] Alternative Energy Development Plan (AEDP) 2015," Department of Alternative Energy Development and Efficiency, Ministry of Energy, 2015.
- [6] M.K.C. Marwali, N. M. Marica and S. K. Shrestha " Battery Capacity Tests Evaluation for Stand-Alone Photovoltaic System"
- [7] E. S. Gavanidou and A. G. Bakirtzis, "Design of a stand alone system with renewable energy sources using trade off methods," *IEEE Trans. Energy Convers.*, vol. 7, pp. 42-48, 1992
- [8] D.F. Al Riza, and S.I.H. Gilani, "Standalone Photovoltaic System Sizing using Peak Sun Hour Method and Evaluation by TRNSYS Simulation.," *International Journal of Renewable Energy Research (IJRER)*, vol.4, no.1, pp.109-114, 2014.
- [9] Tang Xisheng, Wu Xin, Qi Zhiping, "Study on a Stand-alone PV System with Battery/Ultracapacitor Hybrid Energy Storage," *Acta Energiae Solaris Sinica.* Vol.28, No.2, pp:178-183, Feb 2007
- [10] C.-M. Wang and C.-H. Yang, "A novel high input power factor softswitching single-stage single-phase AC/DC/AC converter," in *Proc. IEEE Conf. Veh. Power Propulsion*, Sep. 7-9, 2005, p. 5.

Illumination Control System by LDR for Energy Efficient Buildings

Sakrawee Raweekul
 School of Electrical Engineering, Faculty of Engineering
 Rajamangala University of Technology Isan, Khonkaen Campus
 150 Srichan Road, Muang, Khonkaen, 40000
 THAILAND
 mr_sakrawee@yahoo.com

Abstract— This research was aimed to present the using of the illumination zoning control system design in configuring PWM working cycle for controlling the pressure in LED light bulb to control the building’s CIE (COMMISSION INTERNATIONALE DE L’ECLAIRAGE) brightness standard average and having the energy using relevance. This research had designed the Illumination Control System for LED bulb by LDR for Energy Efficient Buildings by using micro controller as the PWM (Pulse Width Modulation) signal generator to control the MOSFET igniting that leads the current to LED that the brightness would be as the exact current as the calculation. From the system testing, the system could control the brightness from the calculation efficiently and could work with the brightness from the surround which depending in the calculated brightness that made the room had the same brightness in every area and using the building’s electricity efficiency.

the outside, if there was none brightness from the outside, the LED light bulb would be usual, so the working area would have a stable brightness which spending the building’s energy efficiency.

Keywords— Illumination; PWM; LED; building; energy

I. INTRODUCTION

In the building which contains aperture that meant to let the natural light into the building, but most of the time these apertures are covered with curtains all the time because the light is not stable and too bright to control, thus the workers feel uncomfortable to work under a high level of brightness. The basic way out for this problem is using the curtain to darker the room and turning on the light even though the light outside the building is very bright. The light bulbs that were used nowadays having only the highest brightness which don’t relevance to the energy efficient buildings.

From this problem, this research presented the illumination zoning control system design. The process was making the brightness control system for LED light bulb point-to-point connection calculation, using brightness in normal condition without the brightness from the outside evaluator as the base unit that had been designed correctly and that brightness was the brightness that need to be control every time it's used. Thus, when there was the brightness from the outside came to the area where the brightness was under control, there would be brighter, so the system would examine the bright as in Figure 1. If the brightness was higher than the brightness system unit, the brightness control system would reduce the brightness. The evaluator would adjust the PMW working cycle by control the LED light bulb energy spending, and light it as the system control. The reduce energy process depended on the natural brightness from

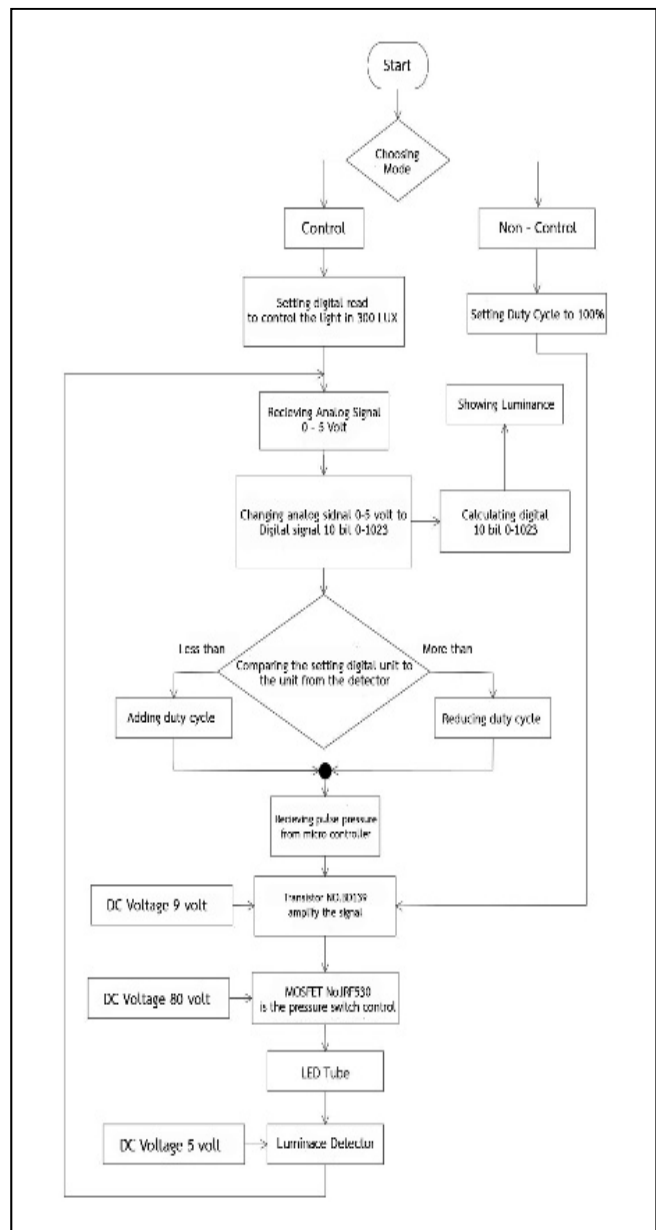


Fig. 1 : Luminance Controlling Process

II. DESIGNING BRIGHTNESS CONTROL SYSTEM

$$E = \frac{\phi}{A}$$

Designing Brightness Building Control System needed the number of the lamp that installed in the area. The type of the lamp and the light bulb was depending on the room. The natural brightness of the room data were needed to be the base data for setting the brightness in each room, and the brightness were needed to be enough and appropriate to the light bulb lifetime. The designing needed to be reserve in case of light degenerate from any incident, the equation which used in calculating this incident evaluating from these following equations

The coefficient of utilization : *CU* or the utilization factor : *UF* according to CIE, this case using *CU*

$$E = \frac{\phi.CU}{A}$$

The lamp maintenance (*MF*) according to the lamp using coefficient table.

$$E = \frac{\phi.CU.MF}{A}$$

$$\phi = \frac{E.A}{CU.MF}$$

- ϕ The room luminous flux (Lumen)
- E* The Illumination values according to IES (Lux)
- A* The area of the room (Square meter ; square foot)
- CU* The coefficient of utilization
- MF* The maintenance

After received ϕ the number of the lamp was needed, which could be found by using this following equation

$$N = \frac{\phi}{(lm / lamp)}$$

- N* The number of the lamp
- lm/lamp* The lightbulb luminous flux (Lumen)

III. ZONING THE AREA FOR CALCULATING THE LUMINOUS

Zoning the area the find the luminous flux to examine the brightness from the outside, the reflection of light and the materials in the room. For example, the one room of the building, when examine the factor, the zoning could be separate into 5 zones, in each zone have a different reflection of light and have a different material. The zone could be like Fig. 2

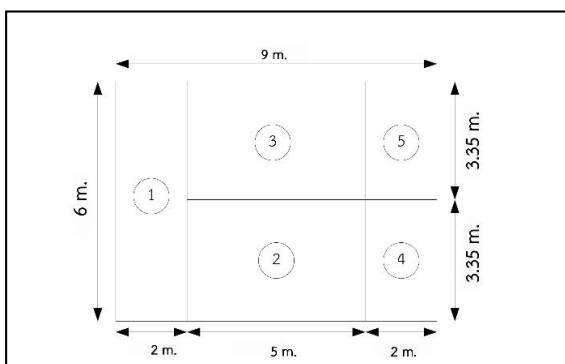


Fig. 2 : Zoning the room

The light system control design by zoning the room, there would be 26 lamps used in this room. According to Zone no.2 and no.3, from the blueprint each zone got 7 lamps. However, installing the 7 lamps wouldn't appropriate to the area, thus 6 lamps would be installed instead. The number of the lamp for this installment was 24 lamps and could be installed like Fig. 3

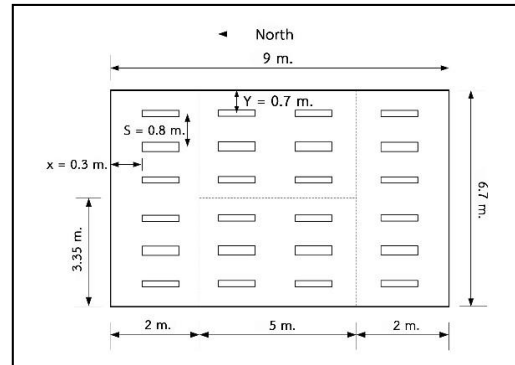


Fig. 3 The Phase for the lamps installment

IV. LDR OPTICAL DETECTOR

The Optical Detector in Fig. 4 using voltage dividing. When the light fell on the LDR, the resistance in LDR would inverse depending on the luminosity which made voltage dropout, the LDR would reverse depending on the resistance.

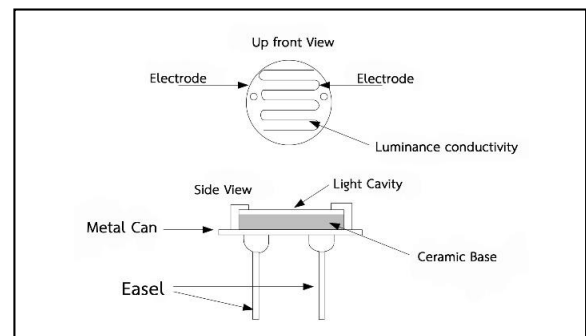


Fig. 4 LDR Structure

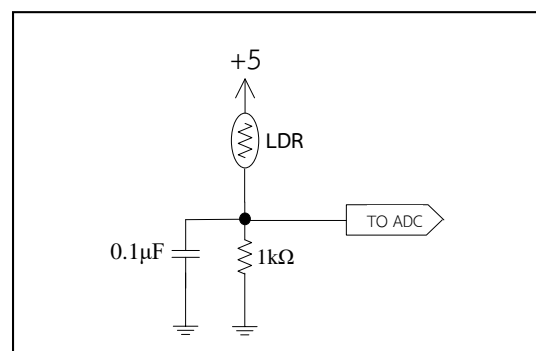


Fig. 5 Luminance Detector Circuit

The output pressure that sends the signal to Micro Controller like Fig. 5 would be separated. The Optical Detector would set the PWM working cycle system. The optical detector in this

research would detect the brightness in 2.25 meter radius according to experiment in Fig. 6

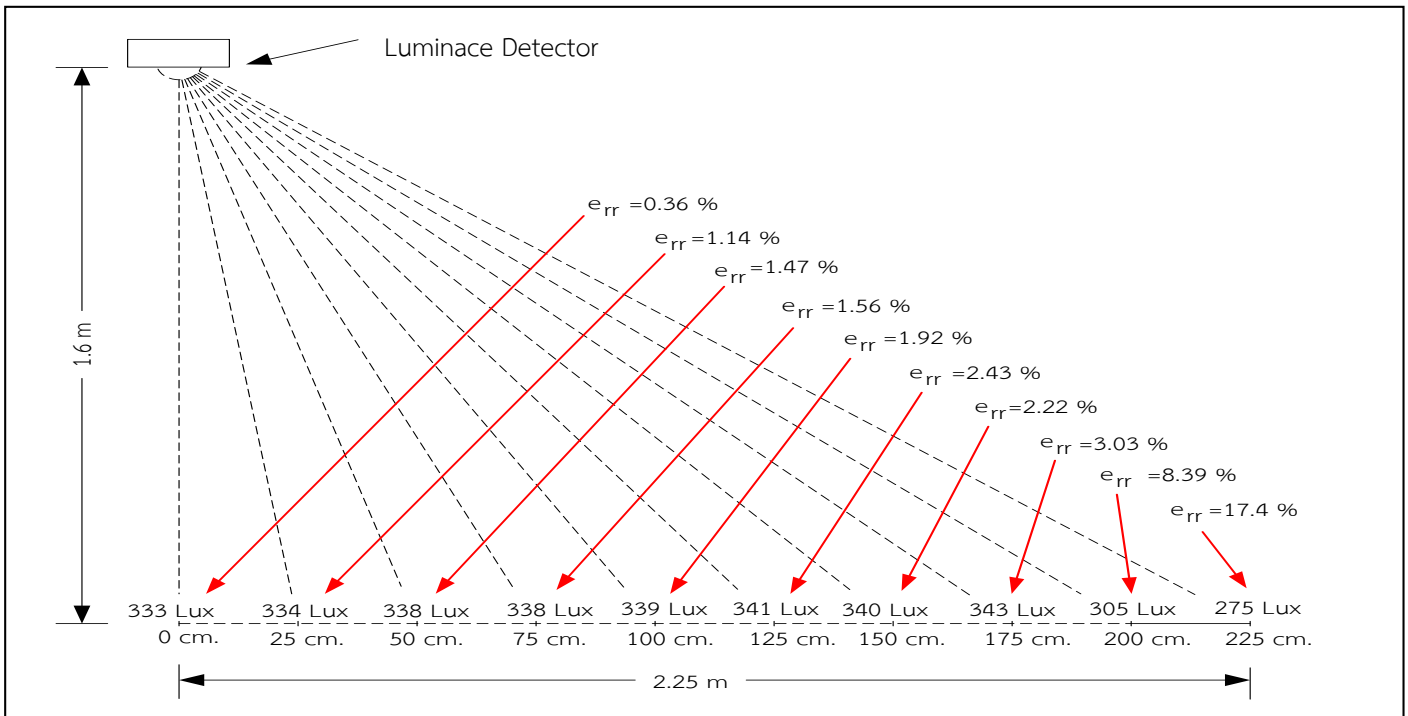


Fig. 6 LDR The LDR light detected radius

V. EXPERIMENT

By designing each material and making the zoning luminous control system into the 8 zone. Installing LDR detectors in 8 zone, using LED lamps which had an ability to disperse the light, as showing at Fig. 7, under some condition. In this topic, the experiment would examine the luminous and electrical energy in each circumstance to experiment the changing of the brightness and energy using which had the process as in Fig. 6.

This experiment, the room contained the light from the outside and the light from LED lamp. The early process of the experiment, the LED wouldn't be controlled, but the next time was.

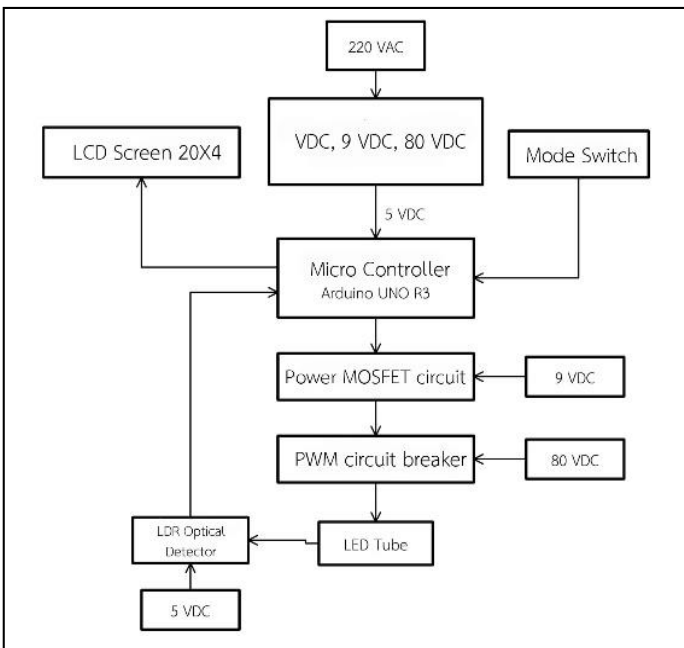


Fig. 7 The system which used in this research

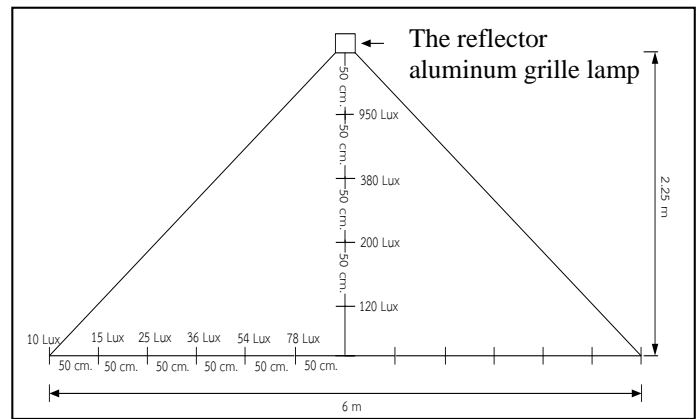


Fig. 8 The light dispersion and the aluminum grille LED lamp light dispersion

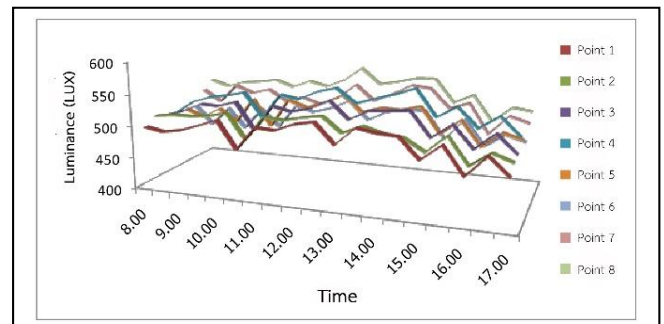


Fig. 9 the relation graph of luminous when the installing the brightness control without using the brightness control

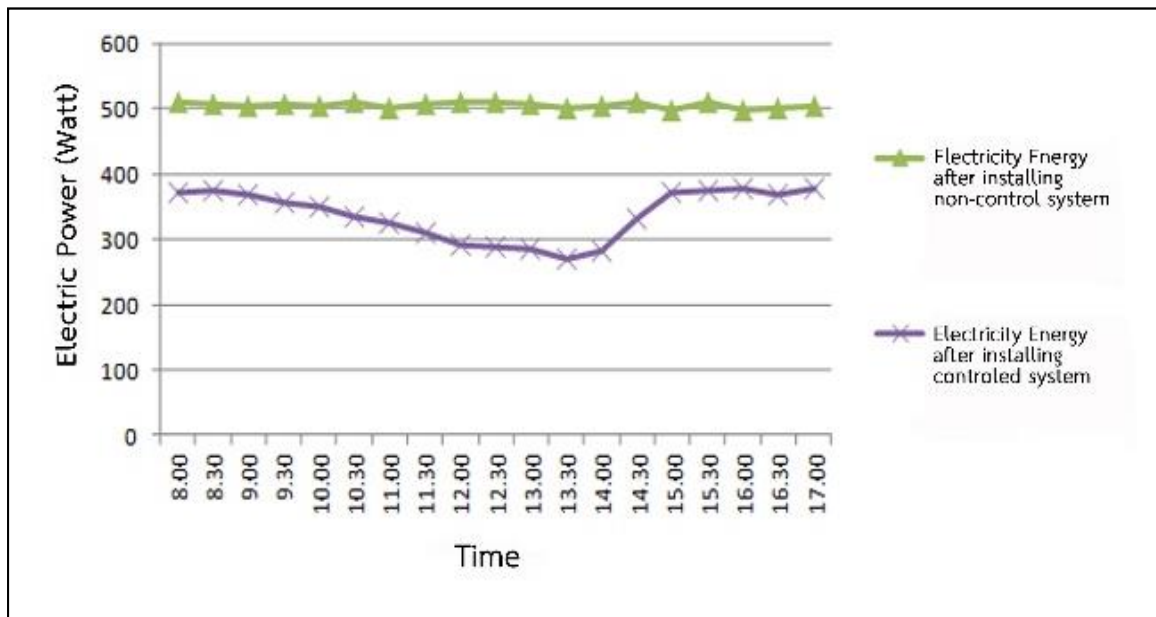


Fig. 10. The comparison of the energy using between the one with the control system and without the control system.

But in the next time, the room set in 300 Lux, in Fig. 8 and 9 as follows. From Fig. 8, the relation between the luminosity and time graph, the graph showed that the luminous that detected by the detector have a high rapidly unstable, changing because the light came from the light bulb and from the outside, and the luminous level was higher than the standard level. Point 5 and 6 had the least brightness because that area had the least brightness, on the other hand, point 7 and 8 got the highest brightness because the light from the outside.

From the experiment in this research, had found that the luminous from the outside could brighten the area the light fall than another area, but the lamps were needed to be open, the luminous level was higher than the standard. When using the LDR detector system to control PWM cycle, controlled the LED light bulbs energy using, The system reduce energy process depended on the natural brightness from the outside, if there was none brightness from the outside, the LED light bulb would be usual, so the working area would have a stable brightness which spending the building's energy efficiency.

VI. CONCLUSION

The research has been designed and built lighting control system, and designed the circuit to create DC voltage for supplying to the LED bulbs installed inside the room. Including, the microcontroller as a Pulse Width Modulation (PWM) signal generator was used to control the ignition of the MOSFET to lead the current supplied to the LED lamp.

ACKNOWLEDGMENT

Following the research was funded from Rajamangala University of Technology Isan, (RMUTI) Khon Kaen Campus. The purposes of the project are promotion and sustainable development in the industrial sector of Thailand and effective

results. I would like to express my sincere appreciation for my co-researcher and my assistant researcher for contributing enormous intellectual and emotional support which led to the project's success. Moreover, I would also like to express my gratitude to Electrical Engineering of the Faculty of Engineering for use of their equipment and instruments.

REFERENCES

1. CIE, Glare Evaluation System for Use Within Outdoor Sports and Area Lighting. TC 5-04, Sixth Draft, December 1992
2. DeCusatis, C., Handbook of Applied Photometry, American Institute of Physics, 1997
3. GE Lighting Systems, Lighting Design Guide Using ALADAN™ Computer Program, General Electric Company, 1996
4. Lindsey, J.L., Applied Illumination Engineering, Second Edition, The Fairmont Press, 1997
5. Ryer, A., Light Measurement Handbook, International Light, 1997

A Study on Conductor Loss Measurement of Microstrip Line

Yusuke Kusama, Yusuke Yokoi, and Robert Weston Johnston
Dept. of communication network and electronics system engineering
National Institute Technology, Kagawa College
551 Kouda, Takuma-cho, Mitoyo City, Kagawa, Japan
kusama@cn.kagawa-nct.ac.jp

Abstract—Many studies on the conductor loss of the copper-clad dielectric substrate have already been reported. In these proposed methods, it is adopted to obtain frequency characteristics of the conductivity from measured values by applying the concept of effective conductivity. In this report, the decrease rate of the signal line cross-sectional area due to the skin effect is estimated from the transmission characteristic measurement according to the physical law that the cross-sectional area of the signal line decreases due to the skin effect instead of the conductivity frequency characteristic.

Keywords—microwave circuit; microstrip ; conductor loss; skin effect; education

I. INTRODUCTION

It has been said human resources in microwave circuit and antenna design having expertise and practical skills are in a state of chronic shortage in Japan [1]. In order to train excellent microwave engineers, it is effective to experience theoretical calculations and experiments with the help of electromagnetic simulators to deepen both knowledge and practical skills [2]. From the viewpoint of student education, lectures are basic for acquisition of theoretical knowledge. However, microwave engineering needs the knowledge of circuits, modules, materials, antennas, measurement techniques, error analysis, etc. Then, applied mathematics, programming skills, simulation techniques are required for analysis and discussions. In order to broaden the scope for students, it is necessary to repeat the systematic arrangement and maintenance of educational contents in accordance with the progress of times and technologies. This requires extensive labor and costs, but acquisition methods of theoretical knowledge are diversifying such as reverse lectures using the web such as Open Course Ware (OCW) or remote lecture deliveries.

Meanwhile, acquisition of measurement techniques and discussion methods require repeated experience of trial and error cycles of theories, trial manufactures, measurements, and simulations. Introduction training periods in recent companies tends to increase year by year, which is considered due to the fact that specialized educational contents are fixed to a certain extent both in theories and experiments, but it is becoming impossible to keep up with changes in technology speeds. In order to cope with such situations, it is necessary to introduce and

develop practical and flexible specialized experimental programs continuously. Overseas, numerous packages related to microwave educations for universities have been developed [3], and in recent years not only experimental equipment but also teaching slides and measurement data sheets are bundled [4][5].

In such a background, we are developing engineering studies designing waveguide circuit elements and microstrip line (MSL) circuits as a microwave experiment package program combining theoretical calculation, simulation and measurement at the National Institute of Technology Kagawa College (NIT-KC) [6]-[8]. In general, low loss substrates are used in MSL circuits and practical problems are almost negligible by evaluating the conductor loss within a low frequency range. However, in order to apply to nearly disposable student experiments, it is firstly required to be lower in costs than the performance. In addition, from the viewpoint of student experiments at the undergraduate level, it is also necessary to be able to discuss at the level of general textbooks, which are widely spread across the world. Experiments on MSL basic circuit designs using FR-4 substrate have been studied so far, but it has been known that considering dielectric loss only greatly deviates from measured values when it exceeds 6 GHz [6][7]. Therefore, the conductor loss, not considered so far, has been necessary from the viewpoint of discussions in specialized student experiments.

II. METHOD FOR EVALUATING CONDUCTOR LOSS

Many studies on the conductor loss of copper-clad dielectric substrates have already been reported [9][10], most of them introduce the concept of an effective conductivity and adopt the method of finding frequency characteristics of the conductivity from measured values by using accurate resonator methods [11]-[21]. However, according to [22], the calculated frequency dependence of the electrical characteristic of copper is constant up to 4 THz of the relaxation frequency at which electrons start to invert their direction before colliding with atomic lattices. Taking this into account, it is not realistic to consider that the physical conductivity of copper changes depending on the frequency in the microwave band of several GHz. Therefore, in this paper, in accordance with the physical law that the cross sectional area of the signal line decreases due to the skin effect, a method of

estimating the reduction rate of the signal line cross sectional area from the transmission characteristic measurement value was studied instead of the conductivity frequency characteristic itself. According to the premise that the attenuation constant due to the dielectric loss is known, it is possible to estimate the attenuation constant due to the conductor loss only from the transmission characteristic. However, the basic idea is the same as the concept of the effective conductivity proposed in previous research since it is difficult to separate conductivity σ and cross-sectional area S as shown by the resistance (1).

$$R = \rho \frac{l}{S} = \frac{l}{\sigma S} \quad (1)$$

Table 1 shows the dielectric constant nominal values of the FR-4 substrate used in this experiment. It is a glass cloth based epoxy resin copper clad laminate NZ-30KR manufactured by Sunhayato Corporation. Although, high frequency characteristics are not described, the dielectric constant is almost constant $\epsilon_r = 4.4$ and $\tan\delta = 0.02$ up to about 10 GHz from the previous study [6]. This value is the same as the "FR4_epoxy" incorporated in ANSYS HFSS material library. Note that we tried dielectric constant derivation by using MSL $\lambda/2$ open resonators and $\lambda/4$ open resonators [23], but error was as large as several tens of % and good results were not obtained because of the unwanted fringing effect.

III. CALCULATION

A. Dielectric loss calculation method

Table 2 shows propagation constants α , β and the characteristic impedance Z_0 when the transmission line is treated as a lumped constant circuit element, and the propagation constants α , β and the wave impedance Z_w when treated as a guided wave. Table 3 shows the similarity between the distributed constant line and the plane wave as equivalent circuits. In order to evaluate the conductor loss by using the distributed constant line, it is necessary to derive the frequency characteristic of the resistance component R per unit length. Since the internal inductance L_e of the conductor gradually approaches zero via the skin effect, it is considered only R needs to be considered. However, except for cases of axisymmetric closed spaces such as a coaxial line, its derivation is not easy [24]-[26]. On the other hand, the transmission power in the TEM mode is the same for both the distributed constant line and the plane wave. Although the dominant mode of the MSL is the quasi-TEM mode, if the effective permittivity ϵ_e is introduced instead of the substrate dielectric constant ϵ_r , the dielectric loss can also be represented by the attenuation constant of the plane wave using (2).

$$\alpha_d = \omega \sqrt{\frac{\mu \epsilon_e}{2}} \left[\sqrt{1 + \left(\frac{\sigma}{\omega \epsilon} \right)^2} - 1 \right]^{1/2} \quad (2)$$

where σ is the loss of the substrate, not the conductivity of the conductor. And $\sigma/\omega\epsilon$ is equal to $\tan\delta$.

TABLE I. NOMINAL VALUE OF SUBSTRATE

Material	Glass epoxy (FR-4)
Dielectric constant	4.5 - 4.9 @ 1 MHz
Dissipation factor	0.013 - 0.02 @1 MHz
Copper foil thickness	35 μm
Substrate thickness	1.6 mm

TABLE II. PROPAGATION CONSTANTS

	General Loss	Dielectric Loss
Transmission Line (V, I)	α $\sqrt{\frac{\omega^2 LC - RG}{2}} \left[\sqrt{1 + \omega^2 \left(\frac{CR + LG}{\omega^2 LC - RG} \right)^2} - 1 \right]^{1/2}$	$\omega \sqrt{\frac{LC}{2}} \left[\sqrt{1 + \left(\frac{G}{\omega C} \right)^2} - 1 \right]^{1/2}$
	β $\sqrt{\frac{\omega^2 LC - RG}{2}} \left[\sqrt{1 + \omega^2 \left(\frac{CR + LG}{\omega^2 LC - RG} \right)^2} + 1 \right]^{1/2}$	$\omega \sqrt{\frac{LC}{2}} \left[\sqrt{1 + \left(\frac{G}{\omega C} \right)^2} + 1 \right]^{1/2}$
Z_0	$\frac{R + j\omega L}{\gamma} = \sqrt{\frac{R + j\omega L}{G + j\omega C}}$	$\sqrt{\frac{j\omega L}{G + j\omega C}}$
Plane Wave (E, H)	α $\sqrt{\frac{\omega^2 \mu \epsilon - \sigma^* \sigma}{2}} \left[\sqrt{1 + \omega^2 \left(\frac{\epsilon \sigma^* + \mu \sigma}{\omega^2 \mu \epsilon - \sigma^* \sigma} \right)^2} - 1 \right]^{1/2}$	$\omega \sqrt{\frac{\mu \epsilon}{2}} \left[\sqrt{1 + \left(\frac{\sigma}{\omega \epsilon} \right)^2} - 1 \right]^{1/2}$
	β $\sqrt{\frac{\omega^2 \mu \epsilon - \sigma^* \sigma}{2}} \left[\sqrt{1 + \omega^2 \left(\frac{\epsilon \sigma^* + \mu \sigma}{\omega^2 \mu \epsilon - \sigma^* \sigma} \right)^2} + 1 \right]^{1/2}$	$\omega \sqrt{\frac{\mu \epsilon}{2}} \left[\sqrt{1 + \left(\frac{\sigma}{\omega \epsilon} \right)^2} + 1 \right]^{1/2}$
Z_w	$\frac{\sigma^* + j\omega \mu}{\gamma} = \sqrt{\frac{\sigma^* + j\omega \mu}{\sigma + j\omega \epsilon}}$	$\sqrt{\frac{j\omega \mu}{\sigma + j\omega \epsilon}}$

TABLE III. EQUIVALENT CIRCUIT

	General loss	Dielectric loss	lossless
Transmission line			
Plane wave			

As an example, Fig. 1 shows $|S_{21}|$ characteristics of a $\lambda/4$ short-circuited resonator when the conductor loss is ignored. The solid line shows HFSS with no internal analysis of conductors, the dotted line shows the calculated result using the propagation constant of the plane wave with the dielectric loss in Table 2, and the broken line shows the calculated result using the dielectric loss (3) in [27]. To consider the influence of dielectric losses, it suffices to multiply the lossless $|S_{21}|$ by the attenuation coefficient $\exp[-2\alpha_d(a + l)]$. Here, α_d is the attenuation constant, a is the length of the arms, and l is the stub length. From this result, it can be seen that the dielectric losses can be evaluated by using the attenuation constant of the plane wave with dielectric loss of Table 2.

$$\alpha_d = \frac{k_0 \epsilon_r (\epsilon_e - 1) \tan \delta}{2 \sqrt{\epsilon_e} (\epsilon_r - 1)} \quad (3)$$

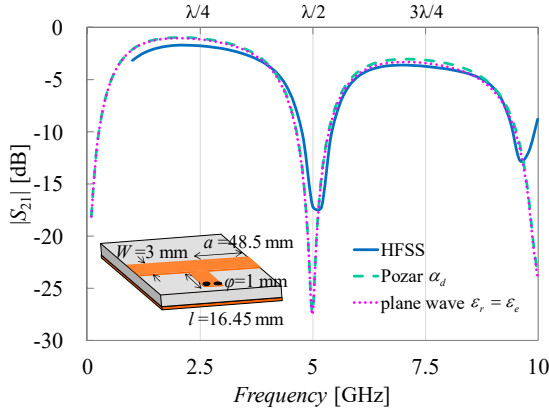


Fig. 1. Comparison of dielectric loss calculation formulas.

B. Method of calculation of conductor loss

In the cross-sectional model shown in Fig. 2, relational expressions between the conductor attenuation constant α_c and the resistance R per unit length are as follows. When the current distribution of the signal line is approximated by a rectangular cross section $S_a = W\delta_s$ by using the back surface skin depth δ_s as shown in the right side of Fig. 2, the resistance R_1 of the signal line per unit length is

$$R_1 = \rho \frac{1}{S_a} = \rho \frac{1}{W\delta_s} \quad [\Omega/\text{m}] \quad (4)$$

where $\rho = 1/\sigma$ indicates the resistivity of copper, and δ_s is the skin depth given by (5).

$$\delta_s = \sqrt{\frac{2}{\omega\mu\sigma}} \quad (5)$$

Substituting (5) to (4) and rearranging becomes

$$R_1 = \frac{1}{W} \sqrt{\frac{\omega\mu}{2\sigma}} = \frac{R_s}{W} \quad (6)$$

where R_s is the surface resistivity of the conductor. For simplicity, if the resistor R_2 of GND is equal to the resistance R_1 of the signal line ($R_1 \approx R_2$), the resistance R per unit length when approximating the current rectangle by the product of skin depth and line width becomes

$$R = R_1 + R_2 = \frac{2R_s}{W} \quad [\Omega/\text{m}] \quad (7)$$

Attenuation constant of conductor loss α_c per unit length is

$$-\alpha_c = \frac{1}{2} \ln \frac{P_{\text{out}}}{P_{\text{in}}} = \frac{1}{2} \ln \frac{P_{\text{in}} - P_{\text{Loss}}}{P_{\text{in}}} \quad [\text{Np}/\text{m}] \quad (8)$$

Here, when the following equation is used for the resistance loss power P_{Loss} and $I^2 = P/Z_0$.

$$P_{\text{Loss}} = P_{\text{in}} - P_{\text{out}} = RI^2 = R \frac{P_{\text{in}}}{Z_0} \quad (9)$$

Substituting (9) into (8) and rearranging becomes

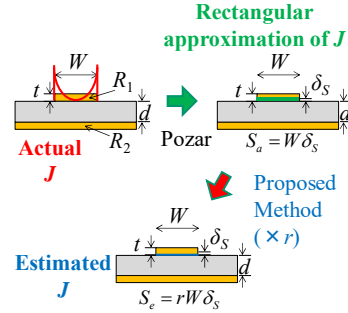


Fig. 2. Rectangular approximation of the signal line current distribution.

$$\alpha_c = -\frac{1}{2} \ln \left(1 - \frac{R}{Z_0} \right) \quad (10)$$

When $R \ll Z_0$ (condition of good conductor), (10) can be approximated by (11).

$$\alpha_c = \frac{1}{2} \frac{R}{Z_0} \quad (11)$$

Substituting (7) into (11) becomes

$$\alpha_c = \frac{R_s}{Z_0 W}, \quad R_s = \sqrt{\frac{\omega\mu_0}{2\sigma}} \quad (12)$$

Equation (12) is an approximate expression of the conductor loss described in [27]. In both (11) and (12), the resistance value increases due to the skin effect, but caution must be taken in application when the condition of good conductor is not satisfied.

It is known that conductor loss hardly occurs even when (12) is applied to the FR-4 substrate, and it deviates greatly from the measured value above 6 GHz [6]. This is considered that the skin depth δ_s calculated by (5) becomes 1 μm or less when it exceeds 4 GHz, but the signal line width W is 3,000 times of that, so the approximated rectangular cross section S_a is too large in the direction of the line width. Therefore, in this study, the attenuation constant α_c was determined so as to fit to the measured $|S_{21}|$ value to estimate the actual sectional current distribution. Specifically, we set the effective conductor cross-section S_e decreased due to the skin effect to

$$S_e = rS_a \quad (r \leq 1) \quad (13)$$

as shown in the lower side of Fig.2, and we decide the coefficient r so that it coincides with measured $|S_{21}|$. At this time, the effective resistance R_e is expressed by (14).

$$R_e = \frac{2}{\sigma S_e} = \frac{2}{\sigma r S_a} = \frac{2}{\sigma r W \delta_s} \quad (14)$$

Although the attenuation constant α_c is represented strictly by (10), in the case of the condition $R \gg Z_0$ where the effective conductor cross-sectional area S_e decreases due to the skin effect and cannot be regarded as a good conductor, it is impossible to obtain α_c directly from (10). Therefore, α_c is also derived approximately by using (11) which is the first term of Taylor's expansion of (10).

IV. MEASUREMENT

A. Measurement sample

Fig. 3 shows a schematic view of measurement samples used in the experiment. The samples are lines, $\lambda/4$ short-circuit resonators, and $\lambda/4$ open resonators. Signal line patterns are fabricated by etching with a line width $W = 3$ mm so that the characteristic impedance becomes $Z_0 = 50 \Omega$. The resonator dimension l is determined to resonate at 2.5 GHz. Other dimensions are shown in the figure. Since etching conditions are based on the manual [28] prepared for student experiments, details are omitted.

B. Measurement system

Fig. 4 shows the measurement system. 3.5 mm coaxial connector tip was set on the calibration surface, then measurement samples were inserted and the transmission characteristic S_{21} was measured in the range of 0.01 - 10 GHz. The instrument used was a vector network analyzer Agilent E8362C with the IF band of 1 kHz and measuring points of 401 points. In addition, SMA connectors RS 526-5785 were attached to both ends of the substrate for connection with coaxial calibration surfaces. As a measurement representative value, one having relatively stable characteristics from among four or more samples was adopted.

V. RESULTS

Fig. 5 shows the transmission characteristics of the line. Four kinds of data show measured value, fitting curve to the measured value, HFSS, and calculated value (hereinafter referred to as Pozar) considering both dielectric loss of (3) and conductor loss of (12). From this result, it is confirmed that HFSS with no inner conductor analysis and Pozar are almost identical.

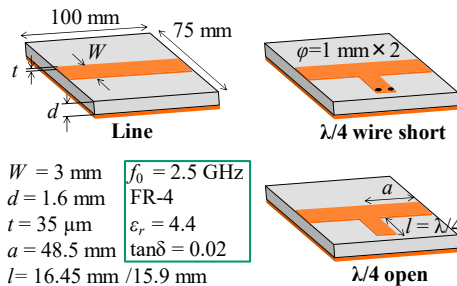


Fig. 3. Measurement samples.

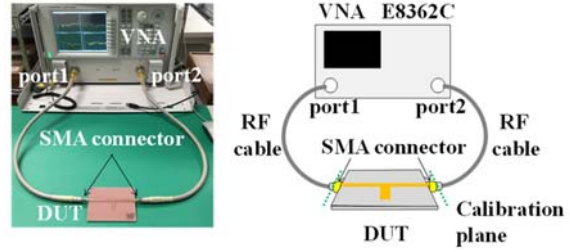


Fig. 4. Schematic view of measurement system.

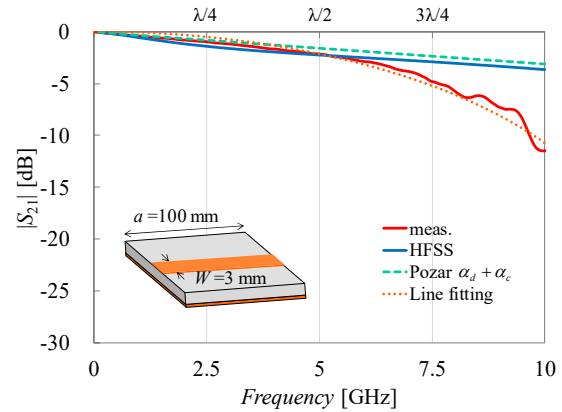


Fig. 5. Measurement result of line.

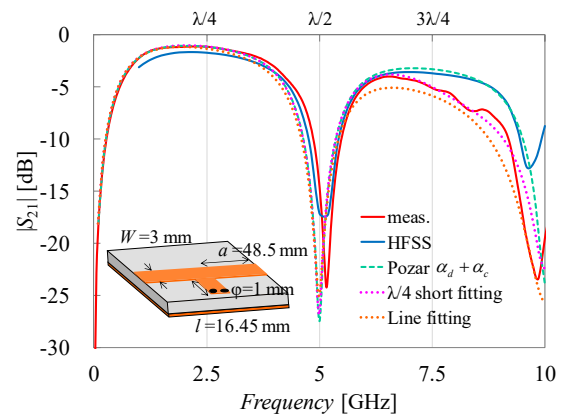


Fig. 6. Measurement result of $\lambda/4$ short resonator.

On the other hand, it is observed that the attenuation of measured value increases from around 6 GHz, and conductor loss exceeds the dielectric loss at 10 GHz. In addition, Fig. 6 shows the transmission characteristics of a $\lambda/4$ short-circuited stub. Five kinds of data show measured value, HFSS, Pozar, and two types of fitting curves to measured values. Two types of fittings show applying α_c obtained through the measured $|S_{21}|$ of the $\lambda/4$ short-circuited resonator, and fitting to the measured $|S_{21}|$ of the line of Fig. 5. When α_c of the line is applied, the attenuation is excessive by 2 dB than the measured value. The reason is considered that lossless $|S_{21}|$ is multiplied by $\exp[-2(\alpha_c + \alpha_d)(a + l)]$ as the attenuation calculation,

but the resonator length l is slightly shortened by the short-circuited wire, and T-junction shortening by the capacitive coupling [29][30]. In addition, Fig. 7 shows the frequency characteristics of the cross-sectional reduction ratio r in (13). In this figure, $r = 1$ means the estimated cross section size is equal to the rectangular approximation. The solid lines show the value determined to fit manually to the measured $|S_{21}|$, and the dotted lines show the case of function fitting. The function used for the line is shown in (15), and for the $\lambda/4$ short-circuited resonator is shown in (16). In these fitting functions, constants a , b , c were determined manually.

$$r_{\text{line}} = \sqrt{\frac{a}{\omega \times 10^{-9}} - b} \quad (15)$$

where $a = 6.3$, $b = 0.3$.

$$r_{\lambda/4} = \frac{1-b}{1 + \exp[a(\omega \times 10^{-9} - c)]} + b \quad (16)$$

where $a = 0.3$, $b = 0.05$, $c = 37.7$.

Since the influence of dielectric loss is larger than conductor loss up to 6 GHz, the difference between the line and $\lambda/4$ short does not matter. However when it exceeds 7 GHz, it can be observed that they agree with each other in 5% or less of the rectangular approximated cross section S_a . This large reduction is not negligible in transmission characteristics.

Next, the effective resistances R_e derived from (14) is shown in Fig. 8. The effective resistance per unit length rapidly increases from around 5 GHz, and becomes larger than the characteristic impedance $Z_0 = 50 \Omega$ at 6 GHz. Furthermore, when it exceeds 9 GHz, it becomes about 10 times of Z_0 . Both fitting curves are similar above 7 GHz. The reason why they disagree above 9 GHz is the fourth resonance of the $\lambda/4$ resonator. Further, Fig. 9 shows the frequency characteristics of the attenuation constant due to the conductor loss α_c derived from (10) and (12). For comparison, attenuation constants due to dielectric loss α_d derived from (2) and (3) are shown. It was found that attenuations due to conductor loss becomes dominant for both the line and $\lambda/4$ short when exceeding 7 GHz. The fact that effective resistance R_e becomes too large not to be ignored means that the characteristic impedance Z_0 becomes a complex number. Then it will be difficult to achieve the impedance matching at higher frequencies. Finally, in order to confirm the validity of the proposed method, the case where the attenuation constant due to the conductor loss obtained from the line, and $\lambda/4$ short circuit resonator are applied to the $\lambda/4$ open resonator. The results are shown in Fig. 10. Five kinds of data are the same as those in the case of the short-circuited resonator in Fig. 6. It was confirmed that by using α_c obtained from the line fitting, the attenuation characteristics agree well up to about 10 GHz with consideration of the fringing effect.

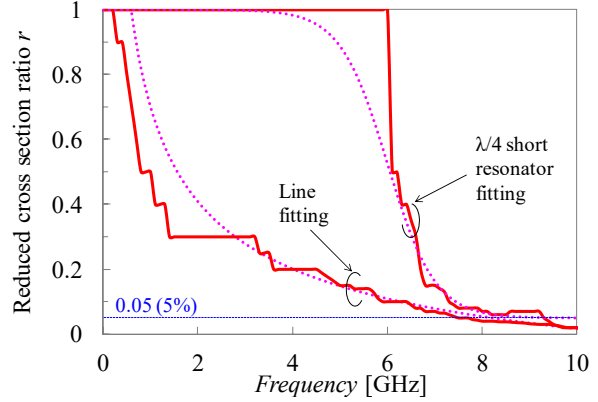


Fig. 7. Frequency characteristics of section reduction rate r .

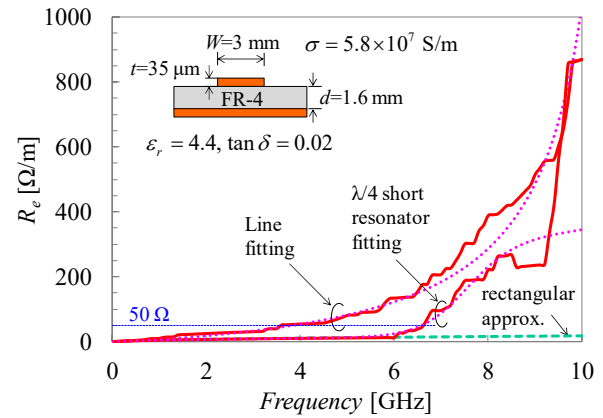


Fig. 8. Estimated resistance per unit length.

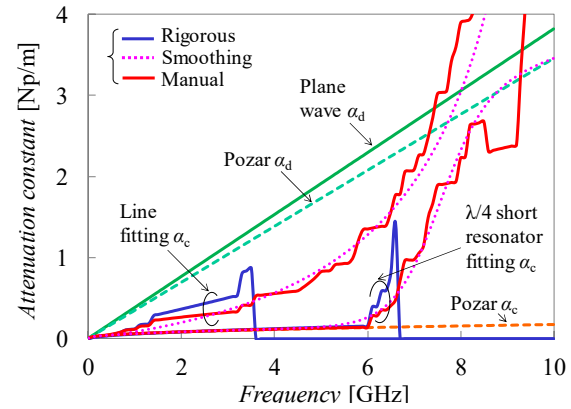


Fig. 9. Estimated attenuation constant.

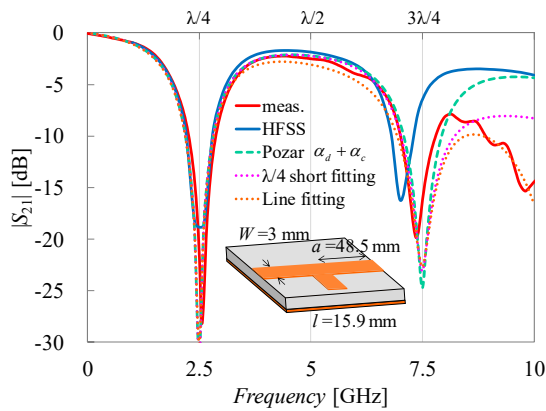


Fig. 10. Measurement result of $\lambda/4$ open resonator. (Measurement value and HFSS only have fringe effect correction, others are $l = 16.45$ mm).

VI. CONCLUSION

As a part of the development of practical program for microwave engineer training, the development of experiment themes to acquire a series of trial and error processes ranging from designs, trial manufactures, simulations, measurements and discussions has been studied. As one of them, the theme of basic MSL circuit fabrication was studied. However, when using a low cost FR-4 substrate suitable for student experiment that is close to disposable, the effect of conductor loss due to the skin effect could not be ignored in the frequencies above 6 GHz. Although, proposed method is same as the concept of effective conductivity already reported, the decrease rate of the signal line cross-sectional area was estimated from the transmission characteristic measurements under the premise of the dielectric loss is known. The attenuation characteristics of $\lambda/4$ short and open resonator were in good agreement with measured values applying the attenuation constant due to the conductor loss obtained from the line measurement. From the above, the validity of this method could be confirmed. In the future, we are planning to introduce and develop a more practical and flexible specialized experiment program by increasing variations of MSL circuit patterns.

ACKNOWLEDGMENT

This research was subsidized by the scientific research fund 26750073, "Development of RF design engineer training program," young scientists (B).

REFERENCES

- [1] S. Nobuo "The request from a microwave device company to institutions of a higher education," Digests 2008 Annual Conf. IEICE Japan, CS-2-1, pp. S29-S30, 2008.
- [23] L. F. Chen, C. K. Ong, C. P. Neo, V. V. Varadan, V. K. Varatan, Microwave Electronics, pp.302-305, Wiley, 2004.
- [24] F. Okada, Microwave Engineering - principles & applications -, p.140, Gakkensha, 1993.
- [2] S. Kawasaki, "Education in a university for microwave solid-state circuits - class and laboratory for the circuit design using a simulator -," Digests 2002 Electronics Society Conf. IEICE Japan, PC-1-3, p. 344, 2002.
- [3] D. M. Pozar "A modern course in microwave engineering," IEEE Trans. Educ, vol. 33, pp. 129-134, 1990.
- [4] <https://www.dreamcatcher.asia/cw>
- [5] <http://www.pid-control.com>
- [6] Y. Yokoi, Y. Kusama, "A study on experimental fabrication of microstrip line basic circuit - for student experiment on microwave engineering -," Technical Report of IEICE Japan, MW2015-139, pp. 35-40, 2015.
- [7] Y. Kusama, Y. Yokoi, "A study on experimental fabrication of microstrip line basic circuit - for student experiment on microwave engineering -," IEICE Trans. C, vol. J99-C, pp. 646-650, 2016.
- [8] Y. Kusama, O. Hashimoto, "Practice of waveguide standing wave experiment," JPS Japan Physics Education in University, vol. 23, pp. 163-166, 2017.
- [9] R. A. Pucel, D. J. Masse, C. P. Hartwig, "Losses in microstrip," IEEE Trans. MTT, vol. MTT-16, pp. 342-350, 1968.
- [10] T. C. Edwards, M. B. Steer, Foundations for Microstrip Circuit Design, p.165, Wiley-IEEE, 2016.
- [11] Y. Kobayashi, M. Katoh, "Microwave measurement of dielectric properties of low-loss materials by the dielectric rod resonator method," IEEE Trans. MTT, vol. MTT-33, pp. 586-592, 1985.
- [12] A. Nakayama, Y. Terashi, H. Uchimura, and A. Fukuura, "Conductivity measurements at the interface between the sintered conductor and dielectric substrate at microwave frequencies, IEEE Trans. MTT, vol. 50, pp. 1665-1674, 2002.
- [13] R. Takaichi, T. Aoki, Y. Kobayashi, "Measurement of back-side surface resistance of a copper-clad dielectric substrate using a dielectric resonator," Technical Report of IEICE Japan, MW2003-141, pp. 109-114, 2003.
- [14] Y. Kobayashi, "Microwave evaluation technique of copper-plated dielectric laminated substrate," IEICE Trans. C, vol. J89-C, pp. 210-216, 2006.
- [15] H. Yoshikawa, A. Nakayama, and Y. Kobayashi "Frequency dependence measurement of conductivity at interface between conductor and dielectric material," IEICE Trans. C, vol. J89-C, pp. 761-768, 2006.
- [16] N. Ishitobi "The measurement of dielectric loss and conductive losses of the substrate with samples by single fabrication process," Technical Report of IEICE Japan, MW2007-87, pp. 35-38, 2007.
- [17] Y. Kobayashi, "Microwave characterization of copper-clad dielectric laminate substrates," IEICE Trans. Electron., vol. E90-C, pp. 2178-2184, 2007.
- [18] S. Yoshitomi, Y. Kobayashi, Z. Ma, "Investigations for influence of gold plating on attenuation in microwave transmission lines," Digests 23rd Annual Conf. JIEP Japan, vol.23, pp. 21-22, 2009.
- [19] Y. Kobayashi, "Measurement method of latest microwave and millimeter wave dielectric material and actual measurement of millimeter wave band (part 2)," Microwave and millimeter wave measurement seminar sponsored by Agilent Corp., 2009.
- [20] Y. Kobayashi, "Microwave / millimeter wave characteristics and measured examples of copper clad printed wiring board," RF world, No. 12, pp. 57-69, CQ publisher, 2010.
- [21] Y. Ono, "from the site of prototype service for microwave / millimeter wave substrate," RF world, No. 38, pp. 123-130, CQ publisher, 2017.
- [22] R. Schmitt, / T. Kuroda (translator), Electromagnetics Explained - A Handbook for Wireless/RF, EMC, and High-Speed Electronics -, pp. 336-338, Maruzen Co., Ltd., 2005.
- [25] S. Sunagawa, Theoretical Electromagnetics 3rd ed., pp. 181-184, Kinokuniya, 1999.
- [26] K. Masu, "Electromagnetic theory for LSI engineers for IoT/IoE era," MWE 2015, TH3A-1.

- [27] D. M. Pozar, Microwave Engineering 3rd ed., pp.144-145, Wiley, 2005.
- [28] <http://www.kusamab.org/>
- [29] S. W. Wedge, R. Compton, D. Rutledge, / K. Mizuno (translator), N. Ishitobi (translator), PUFF Computer Aided Design for Microwave Integrated Circuits, p. 28, California Institute of Technology, 1991.
- [30] T. H. Lee, Planar Microwave Engineering, pp.175-176, Cambridge, 2004.

Convergence Analysis of Adaptive Reduced-Rank Affine Projection Algorithm

Suchada Sitjongsataporn

Department of Electronic Engineering

Mahanakorn Institute of Innovation (MII), Faculty of Engineering

Mahanakorn University of Technology

140 Cheumsamphan Rd., Bangkok 10530 Thailand

E-mail: ssuchada@mut.ac.th

Abstract—In this paper, a convergence analysis of adaptive reduced-rank filtering approach based on joint optimisation of adaptive filtering is proposed with the methods of projection matrix of reduced-rank filter and adaptive affine projection algorithm. We introduce an adaptive reduced-rank affine projection algorithm based on joint optimisation. The cost function is based on Lagrangian criteria. Convergence analysis of adaptive reduced-rank affine projection algorithm is introduced in terms of deviation vector between previous and present tap-weight estimated vectors. Simulation results show that the proposed algorithm can obtain both fast convergence and good tracking compared with the conventional affine projection algorithm.

I. INTRODUCTION

Adaptive filtering based on stochastic gradient scheme have been widely used in many applications on signal processing such as beamforming, system identification and adaptive prediction. The normalised least mean square algorithm is popular choice in the field of adaptive filtering due to its simple and low complexity [1]. Based on the least squares criterion, the recursive least squares algorithm has been introduced with fast convergence and high complexity [2]. This leads to suffer from high computational complexity in practical applications.

The combination on advantages of both normalised least mean square and recursive least squares algorithms, the affine projection algorithm has been proposed as the low computational complexity and fast convergence between the normalised least mean square and recursive least squares algorithms in the field of adaptive filtering [3], [4]. The performance of affine projection algorithm filters can improve the better convergence rate compared to the least mean square based filtering in the case of colored input signals [5], [6].

In [7], the evolution of affine projection algorithm and its variant has been proposed in order to get an efficient and self-reconfigurable algorithm. A simplified statistical analysis of affine projection algorithm has been simulated and theoretically calculated in terms of convergence curves that the approximations are justified for practical use as details in [8]. In [9], proposed affine projection algorithm based adaptive control scheme is verified that shows the validity of simulation results for operation of variable-speed wind generator. In [10], the performance of optimised APA for acoustic echo cancellation has been achieved a proper compromise between the fast tracking and low misadjustment. Most of

affine projection algorithm-based algorithms were developed in a context of system identification in order to optimise the system misalignment.

The idea of reduced-rank filtering is useful in the low sample support situations which has been presented in faster convergence and better tracking performance than full-rank techniques when dealing with the large number of tap-weights vector [11], [12]. In [13], the idea of reduced-rank mechanism based on the joint iterative optimisation of adaptive filtering has been introduced for performing dimensionality reduction, whereas the reduced-rank filter effectively estimates the desired signal. In [14], the semi-blind sparse channel estimation using reduced-rank filtering has been proposed in the stage based on reduced-rank multi-stage Wiener filtering with the limited number of training symbols and at much reduced computational complexity.

The purpose of this paper is two-fold as follows. First, we describe how to derive the reduced-rank approach based on joint optimisation criterion. then, we introduce an adaptive implementation that consists of reduced-rank scheme and affine projection algorithm in order to investigate how the solution of adaptive filtering can be achieved the good performance and dimensional reduction compared to the standard affine projection algorithm. Second, the convergence analysis is introduced using some approximations in expectation calculations for calculating the theoretical convergence.

The remaining part of this paper is organised as follows. In Section II, the reduced-rank approach is described briefly using a projection matrix. Proposed affine projection algorithm is proposed how to organise with orthogonal projections of adjacent gradient direction and normalisation to achieve fast convergence in Section III. And Section IV presents a detailed of adaptive reduced-rank affine projection algorithm based on joint optimisation. Section V introduces the convergence analysis of proposed algorithm. In Section VI, the simulation results of experiments are carried out with some examples. Finally, Section VII concludes this paper.

Some notation will be used throughout this paper as follows: $(\cdot)^H$, $(\cdot)^T$ and $(\cdot)^*$ denote as the Hermitian, transpose and complex conjugate operator, respectively. The operator $E\{\cdot\}$ stands for the expectation. The vectors are in bold lowercase and the matrices are in bold uppercase.

II. REDUCED-RANK APPROACH

Following [13], we describe how to define the reduced-rank approach based on adaptive filtering using a projection matrix.

Let us consider the relationship of output estimate $x(i)$ of reduced-rank mechanism as a function of the received vector $\mathbf{y}(i)$, the projection matrix $\mathbf{S}_D(i)$ and the reduced-rank weight vector $\bar{\mathbf{w}}(i)$ as follows.

The output estimate of filter $x(i)$ is given as

$$\begin{aligned} x(i) &= \bar{\mathbf{w}}^H(i) \mathbf{S}_D^H(i) \mathbf{y}(i) \\ &= \bar{\mathbf{w}}^H(i) \bar{\mathbf{y}}(i), \end{aligned} \quad (1)$$

and

$$\bar{\mathbf{y}}(i) = \mathbf{S}_D^H(i) \mathbf{y}(i), \quad (2)$$

where the dimensions of matrix $\mathbf{S}_D(i)$ is of $M \times D$ in order to process the received vector $\mathbf{y}(i)$ with dimensions $M \times 1$. The $D \times 1$ reduced-rank filter $\bar{\mathbf{w}}(i)$ and $D \times 1$ reduced-rank received vector $\bar{\mathbf{y}}(i)$ are proposed in order to estimate the filter output $x(i)$.

It is noted that the convergence behaviour of stochastic gradient estimation methods imply that their convergence speed is proportional to the M number of elements in the estimator.

Thus, a reduced-rank scheme attempts to solve this limitation by reducing the number of adaptive coefficients of tap-weight vector.

So that the matrix $\mathbf{S}_D(i)$ is to consider for a dimensionality reduction on the received data $\mathbf{y}(i)$ by projecting the received data vectors onto a lower dimensional subspace.

According to the minimum mean square error criterion, the relationship of joint optimisation of the projection matrix $\mathbf{S}_D(i)$ and reduced-rank filter $\bar{\mathbf{w}}(i)$ can be expressed through the following cost function as

$$\begin{aligned} J(i) &= E\{ |d(i) - \bar{\mathbf{w}}^H(i) \mathbf{S}_D^H(i) \mathbf{y}(i)|^2 \} \\ &= E\{ |d(i) - \bar{\mathbf{w}}^H(i) \bar{\mathbf{y}}(i)|^2 \}, \end{aligned} \quad (3)$$

where $d(i)$ is the desired signal.

By minimising the cost function in (3) and fixing the projection matrix $\mathbf{S}_D(i)$ with respect to $\bar{\mathbf{w}}(i)$, the reduced-rank tap-weight estimated vector $\bar{\mathbf{w}}(i)$ can be computed as

$$\bar{\mathbf{w}}(i) = \bar{\mathbf{R}}^{-1}(i) \bar{\mathbf{p}}(i), \quad (4)$$

where

$$\begin{aligned} \bar{\mathbf{R}}(i) &= E\{ \mathbf{S}_D^H(i) \mathbf{y}(i) \mathbf{y}^H(i) \mathbf{S}_D(i) \} \\ &= E\{ \bar{\mathbf{y}}(i) \bar{\mathbf{y}}^H(i) \}, \end{aligned} \quad (5)$$

and

$$\begin{aligned} \bar{\mathbf{p}}(i) &= E\{ d^*(i) \mathbf{S}_D^H(i) \mathbf{y}(i) \} \\ &= E\{ d^*(i) \bar{\mathbf{y}}(i) \}, \end{aligned} \quad (6)$$

where $\bar{\mathbf{y}}(i)$ is given in (2).

In a similar fashion, by fixing the reduced-rank weight vector $\bar{\mathbf{w}}(i)$ and minimising the cost function in (3) with

respect to $\mathbf{S}_D(i)$, the projection matrix $\mathbf{S}_D(i)$ at symbol i is defined as

$$\mathbf{S}_D(i) = \bar{\mathbf{R}}_{yy}^{-1}(i) \mathbf{P}_D(i) \bar{\mathbf{R}}_{yy}^{-1}(i), \quad (7)$$

where

$$\bar{\mathbf{R}}_{yy}(i) = E\{ \mathbf{y}(i) \mathbf{y}^H(i) \}, \quad (8)$$

and

$$\mathbf{P}_D(i) = E\{ d^*(i) \mathbf{y}(i) \bar{\mathbf{w}}^H(i) \}. \quad (9)$$

The associated minimum mean square error (MMSE) criterion becomes

$$\text{MMSE} = \sigma_d^2 - \bar{\mathbf{p}}^H(i) \bar{\mathbf{R}}^{-1}(i) \bar{\mathbf{p}}(i), \quad (10)$$

where $\bar{\mathbf{R}}(i)$ and $\bar{\mathbf{p}}(i)$ are defined in (5) and (6), respectively. The parameter σ_d^2 is the variance of $d(i)$.

It is noticed that the projection matrix $\mathbf{S}_D(i)$ reduces the dimension of received data $\mathbf{y}(i)$ whereas the reduced-rank weight vector $\bar{\mathbf{w}}(i)$ attempts to estimate the desired signal $d(i)$.

In order to ensure the appropriate performance, the rank D must be set by the designer for the rank selection methods, we refer the readers to [15] for more details.

III. AFFINE PROJECTION ALGORITHM

The use of affine projection algorithm (APA) combines many ideas of data reusing, orthogonal projections of M adjacent gradient directions and normalisation in order to achieve faster convergence than least mean square-based algorithms [1].

Following [1], the objective of the affine projection algorithm (APA) is to minimise as:

$$\begin{aligned} \min_{\hat{\mathbf{w}}} \quad & \frac{1}{2} \|\hat{\mathbf{w}}(i) - \hat{\mathbf{w}}(i-1)\|^2, \\ \text{subject to} \quad & \mathbf{d}(i) - \mathbf{Y}(i)^H \hat{\mathbf{w}}(i-1) = 0. \end{aligned} \quad (11)$$

where $\mathbf{d}(i)$ is the desired vector. The operator $\|\cdot\|^2$ denotes as the Euclidean norm. The matrix $\mathbf{Y}(i)$ is the received matrix and the vector $\hat{\mathbf{w}}(i)$ is the tap-weighted estimate vector at symbol i , respectively.

Then, the adaptive affine projection algorithm can obtain the next coefficient vector $\hat{\mathbf{w}}(i+1)$ as close as possible to the present coefficient vector $\hat{\mathbf{w}}(i)$, while forcing the *a posteriori* estimate error vector $\mathbf{e}(i)$ to be zero.

The *a posteriori* estimated error vector $\mathbf{e}(i)$ at symbol i is given as

$$\mathbf{e}(i) = \mathbf{d}(i) - \mathbf{Y}^H(i) \hat{\mathbf{w}}(i), \quad (12)$$

where $\mathbf{Y}(i)$ is the received matrix.

Therefore, the update tap-weight estimated vector $\hat{\mathbf{w}}(i+1)$ based on affine projection algorithm can be expressed in the recursion form as

$$\hat{\mathbf{w}}(i+1) = \hat{\mathbf{w}}(i) - \mu \mathbf{Y}(i) (\mathbf{Y}(i)^H \mathbf{Y}(i) + \gamma \mathbf{I})^{-1} \mathbf{e}(i), \quad (13)$$

where μ is the step-size parameter and \mathbf{I} is the identity matrix. The parameter γ is a small constant.

IV. ADAPTIVE REDUCED-RANK AFFINE PROJECTION ALGORITHM

In this section, we conclude how to define an adaptive reduced-rank affine projection algorithm (AR-APA) based on the proposed reduced-rank approach and joint optimisation criterion as shown in [16].

The proposed joint algorithm shown in Fig. 1 employs a projection matrix $\mathbf{S}_D(i)$ with dimension $M \times D$ to project the $M \times M$ received matrix $\mathbf{Y}(i)$ onto the reduced-rank received matrix $\bar{\mathbf{Y}}(i)$. The $D \times 1$ reduced-rank weight vector based on the proposed AR-APA $\bar{\mathbf{w}}(i)$ combines the matrix $\bar{\mathbf{Y}}(i)$ to yield an output estimate vector $\mathbf{x}(i)$.

The objective of the reduced-rank affine projection algorithm is to minimise as

$$\min_{\bar{\mathbf{w}}} \|\bar{\mathbf{w}}(i+1) - \bar{\mathbf{w}}(i)\|^2, \quad (14)$$

$$\min_{\mathbf{S}_D} \|\mathbf{S}_D(i+1) - \mathbf{S}_D(i)\|^2, \quad (15)$$

subject to

$$\mathbf{d}(i) - (\mathbf{S}_D^H(i) \mathbf{Y}(i) \mathbf{S}_D(i))^H \bar{\mathbf{w}}(i+1) = 0, \quad (16)$$

$$\mathbf{d}(i) - (\mathbf{S}_D^H(i+1) \mathbf{Y}(i) \mathbf{S}_D(i))^H \bar{\mathbf{w}}(i) = 0. \quad (17)$$

where $\mathbf{y}(i)$ is the received vector and

$$\mathbf{Y}(i) = [\mathbf{y}(i) \quad \mathbf{y}(i-1) \quad \cdots \quad \mathbf{y}(i-M+1)],$$

$$\mathbf{d}(i) = [d(i) \quad d(i-1) \quad \cdots \quad d(i-D+1)].$$

By the method of Lagrange multipliers, the constrained optimisation in (14) and (15) can be transformed into an unconstrained optimisation. Therefore, the unconstrained cost function of proposed algorithm to be minimised using the method of Lagrange multipliers.

By formulating the cost function in (14) and (15) with respect to the complex constraints in (16) and (17) that can be expressed as

$$\mathcal{L}_1(i) = \|\bar{\mathbf{w}}(i+1) - \bar{\mathbf{w}}(i)\|^2$$

$$+ \lambda_1 [\mathbf{d}(i) - (\mathbf{S}_D^H(i) \mathbf{Y}(i) \mathbf{S}_D(i))^H \bar{\mathbf{w}}(i+1)], \quad (18)$$

$$\mathcal{L}_2(i) = \|\mathbf{S}_D(i+1) - \mathbf{S}_D(i)\|^2$$

$$+ \lambda_2 [\mathbf{d}(i) - (\mathbf{S}_D^H(i+1) \mathbf{Y}(i) \mathbf{S}_D(i))^H \bar{\mathbf{w}}(i)], \quad (19)$$

where λ_1 and λ_2 are complex vector Lagrange multipliers.

By differentiating the gradient terms of (18) and (19) with respect to $\bar{\mathbf{w}}(i+1)$ and $\mathbf{S}_D(i+1)$, we arrive at

$$\nabla_{\bar{\mathbf{w}}(i+1)} \mathcal{L} = 2[\bar{\mathbf{w}}(i+1) - \bar{\mathbf{w}}(i)] - \lambda_1 (\mathbf{S}_D^H(i) \mathbf{Y}(i) \mathbf{S}_D(i)), \quad (20)$$

$$\nabla_{\mathbf{S}_D(i+1)} \mathcal{L} = 2[\mathbf{S}_D(i+1) - \mathbf{S}_D(i)] - \lambda_2 (\bar{\mathbf{w}}^H(i) \mathbf{S}_D(i) \mathbf{Y}(i)). \quad (21)$$

By setting them to zero and solving the resulting equations above, the reduced-rank tap-weight estimated vector $\bar{\mathbf{w}}(i)$ and the projection matrix $\mathbf{S}_D(i)$ can be performed with the convergence factor μ and η in the recursion form as

$$\bar{\mathbf{w}}(i+1) = \bar{\mathbf{w}}(i) - \mu \bar{\mathbf{Y}}^H(i) (\bar{\mathbf{Y}}(i) \bar{\mathbf{Y}}^H(i))^{-1} \boldsymbol{\xi}(i), \quad (22)$$

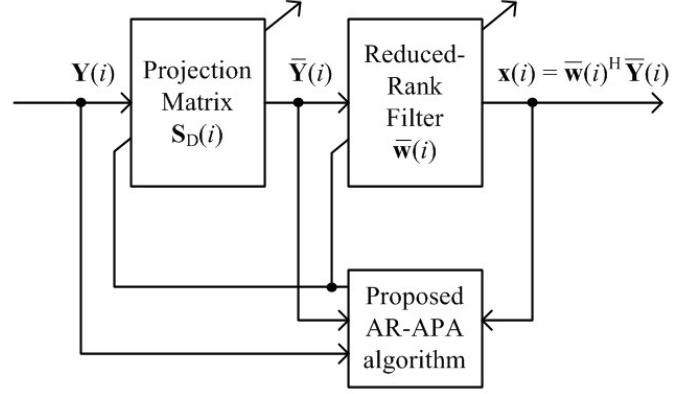


Fig. 1. Proposed joint adaptive reduced-rank affine projection algorithm (AR-APA) schematic diagram [16].

$$\mathbf{S}_D(i+1) = \mathbf{S}_D(i) - \eta \boldsymbol{\xi}(i) \bar{\boldsymbol{\Psi}}(i) (\bar{\boldsymbol{\Psi}}^H(i) \bar{\boldsymbol{\Psi}}(i))^{-1}, \quad (23)$$

and

$$\bar{\mathbf{Y}}(i) = \mathbf{S}_D^H(i) \mathbf{Y}(i) \mathbf{S}_D(i), \quad (24)$$

$$\bar{\boldsymbol{\Psi}}(i) = \bar{\mathbf{w}}^H(i) \mathbf{S}_D(i) \mathbf{Y}(i), \quad (25)$$

$$\boldsymbol{\xi}(i) = \mathbf{d}(i) - (\mathbf{S}_D^H(i) \mathbf{Y}(i) \mathbf{S}_D(i))^H \bar{\mathbf{w}}(i), \quad (26)$$

where the parameters μ and η are the step-size parameters. The vector $\boldsymbol{\xi}(i)$ is the *a posteriori* error vector.

As suggested in [1], a small constant γ multiplied to an identity matrix is added to the matrices $(\bar{\mathbf{Y}}^H(i) \bar{\mathbf{Y}}(i))$ in (22) and $(\bar{\boldsymbol{\Psi}}^H(i) \bar{\boldsymbol{\Psi}}(i))$ in (23) to avoid numerical problems in the matrix inversion.

Therefore, the reduced-rank tap-weight estimated vector $\bar{\mathbf{w}}(i)$ in (22) and the update projection matrix $\mathbf{S}_D(i)$ in (23) can be rewritten as

$$\bar{\mathbf{w}}(i+1) = \bar{\mathbf{w}}(i) - \mu \bar{\mathbf{Y}}(i) (\bar{\mathbf{Y}}^H(i) \bar{\mathbf{Y}}(i) + \gamma \bar{\mathbf{I}})^{-1} \boldsymbol{\xi}(i), \quad (27)$$

$$\mathbf{S}_D(i+1) = \mathbf{S}_D(i) - \eta \bar{\boldsymbol{\Psi}}(i) (\bar{\boldsymbol{\Psi}}^H(i) \bar{\boldsymbol{\Psi}}(i) + \gamma \bar{\mathbf{I}})^{-1} \boldsymbol{\xi}(i), \quad (28)$$

where γ is a small constant. The matrices $\bar{\mathbf{Y}}(i)$ and $\bar{\boldsymbol{\Psi}}(i)$ are defined in (24) and (25), respectively. The estimated error vectors $\boldsymbol{\xi}(i)$ is rewritten as

$$\boldsymbol{\xi}(i) = \mathbf{d}(i) - \bar{\mathbf{Y}}^H(i) \bar{\mathbf{w}}(i). \quad (29)$$

The matrix $\bar{\mathbf{I}}$ is the $M \times D$ modified identity matrix as

$$\bar{\mathbf{I}} = [\mathbf{I}_D \quad \mathbf{0}_{D, M-D}]^T$$

$$= \begin{bmatrix} 1 & 0 & \cdots & 0 & 0 \\ 0 & 1 & \cdots & 0 & 0 \\ \vdots & \vdots & \ddots & \vdots & 0 \\ 0 & 0 & \cdots & 1 & 0 \end{bmatrix}^T, \quad (30)$$

where \mathbf{I}_D is the $D \times D$ identity matrix and $D < M$.

The joint scheme using the adaptive reduced-rank approach and affine projection algorithm (AR-APA) is summarised in Table II.

TABLE I
 SUMMARY OF AFFINE PROJECTION ALGORITHM (APA)[1].

-
- Starting with these initial parameters:
 $\bar{\mathbf{w}}(0) = \mathbf{0}$ and $e(0) = \sigma_\eta^2$.
 $\hat{\mu}$ are small constant.
 $\gamma = 1 \times 10^{-7}$
 \mathbf{I} is an identity matrix.
 - Do for $i \in N; i = 1, 2, \dots$, compute.
 - 1) To arrange the matrix $\bar{\mathbf{Y}}(i)$ as:

$$\mathbf{Y}(i) = [\mathbf{y}(i) \quad \mathbf{y}(i-1) \quad \dots \quad \mathbf{y}(i-M+1)] .$$
 - 2) To calculate $\mathbf{e}(i)$ as:

$$\mathbf{e}(i) = \mathbf{d}(i) - \mathbf{Y}(i)\mathbf{w}^H(i) .$$
 - 3) To compute $\mathbf{w}(i)$ as:

$$\mathbf{w}(i+1) = \mathbf{w}(i) - \hat{\mu} \mathbf{Y}(i)(\mathbf{Y}^H(i)\mathbf{Y}(i) + \gamma \mathbf{I})^{-1} \mathbf{e}(i) .$$
 end
-

V. CONVERGENCE ANALYSIS OF AR-APA

In this framework, the deviation vector $\zeta(i)$ can be expressed following [10] as

$$\zeta(i) = \|\bar{\mathbf{w}}(i+1) - \bar{\mathbf{w}}(i)\| . \quad (31)$$

Developing (27) based on (31), we get

$$\zeta(i) = \zeta(i-1) + \mu \bar{\mathbf{Y}}(i) (\bar{\mathbf{Y}}^H(i) \bar{\mathbf{Y}}(i) + \gamma \bar{\mathbf{I}})^{-1} \xi(i) . \quad (32)$$

Let us consider the update term of proposed AR-APA in the second term of the right-hand side of (27). It is assumed that

$$E\{\bar{\mathbf{Y}}^H(i) \bar{\mathbf{Y}}(i)\} = L \bar{\mathbf{R}}_{\bar{\mathbf{Y}}}(i) , \quad (33)$$

where $\bar{\mathbf{R}}_{\bar{\mathbf{Y}}}(i)$ is the correlation of reduced-rank received matrix.

For the large values of L , it holds that

$$\bar{\mathbf{Y}}^H(i) \bar{\mathbf{Y}}(i) \approx L \bar{\mathbf{R}}_{\bar{\mathbf{Y}}} . \quad (34)$$

Let us denote that

$$\mathbf{\Upsilon}(i) = \mu (\bar{\mathbf{Y}}^H(i) \bar{\mathbf{Y}}(i) + \gamma \bar{\mathbf{I}})^{-1} , \quad (35)$$

where μ is step-size parameter and the modified identity matrix $\bar{\mathbf{I}}$ is given in (30).

Substituting (33) in (35), we arrive at

$$\mathbf{\Upsilon}(i) \simeq \mu (L \bar{\mathbf{R}}_{\bar{\mathbf{Y}}}(i) + \gamma \bar{\mathbf{I}})^{-1} . \quad (36)$$

It is noted that this matrix $\mathbf{\Upsilon}(i)$ contains both the control parameter as μ , γ and the statistical information of reduced-rank input signal.

Consequently, the squared Euclidean norm in (32) and taking expectation on both sides for removing the uncorrelated

 TABLE II
 SUMMARY OF PROPOSED ADAPTIVE REDUCED-RANK AFFINE PROJECTION ALGORITHM (AR-APA).

-
- Starting with these initial parameters:
 $\mathbf{S}_D(0) = \bar{\mathbf{\Psi}}(0) = \alpha[\mathbf{I}_D \quad \mathbf{0}_{D, M-D}]^T$.
 \mathbf{I} is an identity matrix.
 $\bar{\mathbf{w}}(0) = [1 \quad \mathbf{0}_{1, D-1}]^T$ and $\xi(0) = [\sigma_\eta^2 \quad \mathbf{0}_{1, D-1}]^T$.
 α , μ and η are small constant.
 $\gamma = 1 \times 10^{-7}$.
 - Do for $i \in N; i = 1, 2, \dots$, compute.
 - 1) To arrange the matrices $\bar{\mathbf{Y}}(i)$ and $\bar{\mathbf{\Psi}}(i)$ as:

$$\begin{aligned} \bar{\mathbf{Y}}(i) &= \mathbf{S}_D^H(i) \mathbf{Y}(i) \mathbf{S}_D(i) , \\ \bar{\mathbf{\Psi}}(i) &= \bar{\mathbf{w}}^H(i) \mathbf{S}_D(i) \mathbf{Y}(i) , \\ \mathbf{Y}(i) &= [\mathbf{y}(i) \quad \mathbf{y}(i-1) \quad \dots \quad \mathbf{y}(i-M+1)] . \end{aligned}$$
 - 2) To calculate $\mathbf{e}(i)$ as:

$$\xi(i) = \mathbf{d}(i) - \bar{\mathbf{Y}}(i)^H \bar{\mathbf{w}}(i) .$$
 - 3) To compute $\bar{\mathbf{w}}(i)$ and $\mathbf{S}_D(i)$ as:

$$\begin{aligned} \bar{\mathbf{w}}(i+1) &= \bar{\mathbf{w}}(i) - \mu \bar{\mathbf{Y}}(i) (\bar{\mathbf{Y}}^H(i) \bar{\mathbf{Y}}(i) + \gamma \bar{\mathbf{I}})^{-1} \xi(i) , \\ \mathbf{S}_D(i+1) &= \mathbf{S}_D(i) - \eta \bar{\mathbf{\Psi}}(i) (\bar{\mathbf{\Psi}}^H(i) \bar{\mathbf{\Psi}}(i) + \gamma \bar{\mathbf{I}})^{-1} \xi(i) . \end{aligned}$$
 end
-

products, we get

$$\begin{aligned} E\{\|\zeta(i)\|_2^2\} &= E\{\|\zeta(i-1)\|_2^2\} \\ &+ 2 E\{\xi^T(i) \mathbf{\Upsilon}(i) \bar{\mathbf{Y}}^H(i) \zeta(i-1)\} \\ &- E\{\xi^T(i) \mathbf{\Upsilon}(i) \bar{\mathbf{Y}}^H(i) \bar{\mathbf{Y}}(i) \mathbf{\Upsilon}(i) \xi(i)\} , \end{aligned} \quad (37)$$

or, equivalently

$$\begin{aligned} E\{\|\zeta(i)\|_2^2\} &= E\{\|\zeta(i-1)\|_2^2\} \\ &+ 2 \text{tr}[\mathbf{\Upsilon}(i) E\{\bar{\mathbf{Y}}^H(i) \zeta(i-1) \xi(i)\}] \\ &- L \text{tr}[\mathbf{\Upsilon}(i) \bar{\mathbf{R}}_{\bar{\mathbf{Y}}}(i) \mathbf{\Upsilon}(i) E\{\xi^T(i) \xi(i)\}] , \end{aligned} \quad (38)$$

where $\text{tr}[\cdot]$ denotes as the trace of a matrix.

Assuming that, the estimated error vector $\xi(i)$ can be expressed as

$$\xi(i) \simeq \bar{\mathbf{Y}}^H(i) \zeta(i-1) . \quad (39)$$

Consequently, substituting (39) in the first cross-correlation term from (38) can be developed as

$$E\{\bar{\mathbf{Y}}^H(i) \zeta(i-1) \xi(i)\} \simeq E\{\bar{\mathbf{Y}}^H(i) \zeta(i-1) \zeta^H(i-1) \bar{\mathbf{Y}}(i)\} . \quad (40)$$

Similarly, based on (39) in the second cross-correlation term from (38) can be obtained as

$$E\{\xi^T(i) \xi(i)\} \simeq E\{\bar{\mathbf{Y}}(i) \zeta(i-1) \zeta^H(i-1) \bar{\mathbf{Y}}(i)\} . \quad (41)$$

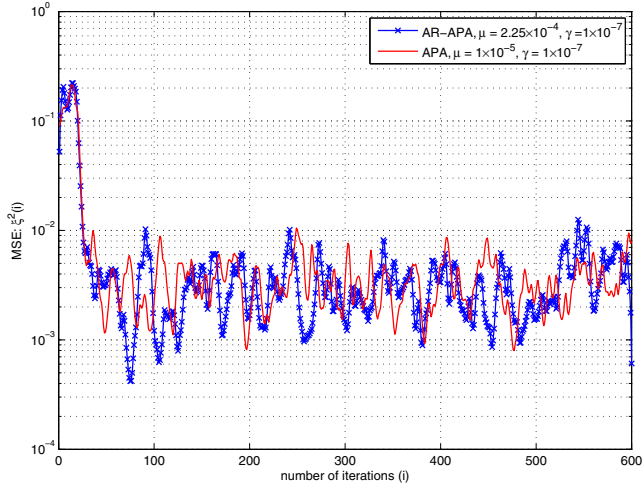


Fig. 2. Comparison of mean square error (MSE) for proposed AR-APA with $\mu = 2.25 \times 10^{-4}$, $\alpha = 1.15 \times 10^{-2}$, $\eta = 1.25 \times 10^{-4}$ and conventional APA [1] with $\mu = 1 \times 10^{-5}$ and a zero-mean white noise sequence through AR(3) process, when SNR = 20 dB.

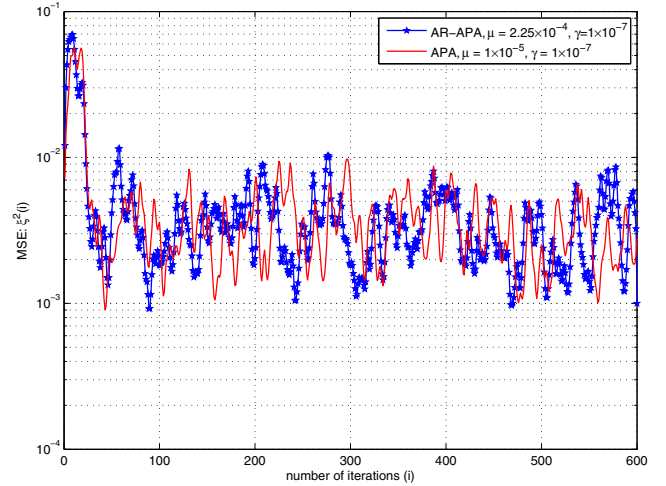


Fig. 3. Comparison of MSE for proposed AR-APA with $\mu = 2.25 \times 10^{-4}$, $\alpha = 1.15 \times 10^{-2}$, $\eta = 1.25 \times 10^{-4}$ and APA [1] with $\mu = 1 \times 10^{-5}$ and a zero-mean white noise sequence through AR(3) process, when SNR = 30dB.

Denoting

$$\delta(i) \simeq E\{\|\zeta(i)\|_2^2\}, \quad (42)$$

and introducing (40)-(42) in (38), we obtain

$$\begin{aligned} \delta(i) = & \delta(i-1) + \text{tr}[\mathbf{\Upsilon}(i)E\{\bar{\mathbf{Y}}^H(i)\zeta(i-1)\zeta^H(i-1)\bar{\mathbf{Y}}(i)\}] \\ & - L \cdot \text{tr}[\mathbf{\Upsilon}(i)\bar{\mathbf{R}}_{\bar{\mathbf{Y}}}(i)\mathbf{\Upsilon}(i)E\{\boldsymbol{\xi}^T(i)\boldsymbol{\xi}(i)\}]. \end{aligned} \quad (43)$$

In order to facilitate the analysis, let us assume that the input signal is white or weakly correlation, so that we can use the approximation as

$$\bar{\mathbf{R}}_{\bar{\mathbf{Y}}}(i) \approx \sigma_{\bar{\mathbf{Y}}}^2 \bar{\mathbf{I}}. \quad (44)$$

Introducing (44) in (36), we arrive at

$$\begin{aligned} \mathbf{\Upsilon}(i) & \simeq \mu (L\sigma_{\bar{\mathbf{Y}}}^2 \bar{\mathbf{I}} + \gamma \bar{\mathbf{I}})^{-1} \\ & \simeq \frac{\mu}{L\sigma_{\bar{\mathbf{Y}}}^2 + \gamma} \bar{\mathbf{I}} \\ & \simeq \beta \bar{\mathbf{I}}. \end{aligned} \quad (45)$$

Rewriting (34) with (44), we get

$$E\{\bar{\mathbf{Y}}^H(i)\bar{\mathbf{Y}}^H(i)\} \simeq L\sigma_{\bar{\mathbf{Y}}}^2 \bar{\mathbf{I}}. \quad (46)$$

Substituting (44)-(46) into (43), the squared Euclidean norm of a *posterior* deviation vector can be finally expressed as

$$\delta(i) = \delta(i-1) + (1 - \beta\sigma_{\bar{\mathbf{Y}}}^2 L) \cdot E\{\boldsymbol{\xi}^T(i)\boldsymbol{\xi}(i)\}, \quad (47)$$

and $\boldsymbol{\xi}(i)$ is the *a posteriori* estimated error as

$$\boldsymbol{\xi}(i) = \mathbf{d}(i) - \bar{\mathbf{Y}}^H(i)\bar{\mathbf{w}}(i), \quad (48)$$

where $\bar{\mathbf{Y}}(i)$ is given in (24).

VI. SIMULATION RESULTS

We simulate the random processes as presented in [17] by carrying out of the computer simulations. The channel is randomly generated. The adaptive filter vector and the unknown channel are assumed to have the same number of taps. The input signal is obtained by passing samples of unit variance white Gaussian noise random sequence through a third-order low-pass filter, or AR(3) as

$$H_1(z) = \frac{1}{1 - 1.5z^{-1} + z^{-2} - 0.25z^{-3}},$$

and through a fourth-order low-pass filter, or AR(4) as

$$H_2(z) = \frac{1}{1 - 1.79z^{-1} + 1.85z^{-2} - 1.27z^{-3} + 0.41z^{-4}}.$$

By filtering samples of zero-mean white noise random sequence through the following second-order system, or AR(2,2) as [6]

$$H_3(z) = \frac{1 + 0.5z^{-1} + 0.81z^{-2}}{1 - 0.59z^{-1} + 0.4z^{-2}}.$$

The initial parameters of proposed adaptive reduced-rank affine projection algorithm (AR-APA) algorithm are as follows: $D = 6$, $M = 9$, $\alpha = 1.15 \times 10^{-2}$, $\mu = 2.25 \times 10^{-4}$, $\eta = 1.25 \times 10^{-4}$. The parameters of conventional affine projection algorithm (APA) [1] is initialised at $\mu = 1 \times 10^{-5}$. The initial parameters of both algorithms are as follows: $M = 9$, $\gamma = 1 \times 10^{-7}$. The different setting of signal to noise ratio (SNR) is of 20 and 30 dB. The number of independent trials is of 300. The proposed AR-APA algorithm can be computed with the soft-constrained initialisation [18].

Fig. 2 and Fig. 3 depict the trajectories of mean square error (MSE) curves of proposed adaptive reduced-rank affine projection algorithm (AR-APA) and conventional affine

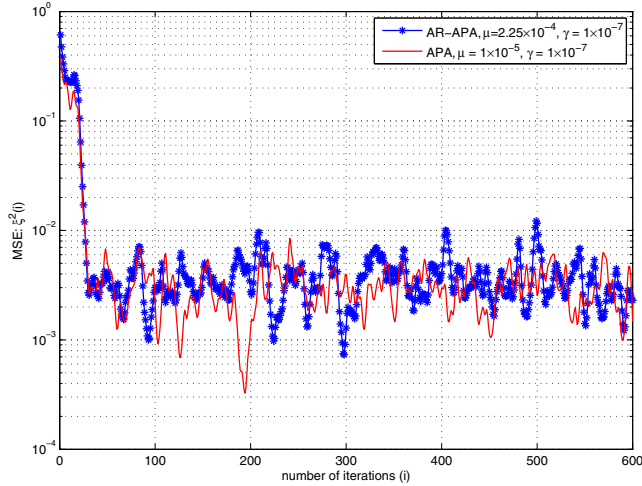


Fig. 4. Comparison of MSE for proposed AR-APA with $\mu = 2.25 \times 10^{-4}$, $\alpha = 1.15 \times 10^{-2}$, $\eta = 1.25 \times 10^{-4}$ and APA [1] with $\mu = 1 \times 10^{-5}$ and a zero-mean white noise sequence through AR(4) process, when SNR = 20dB.

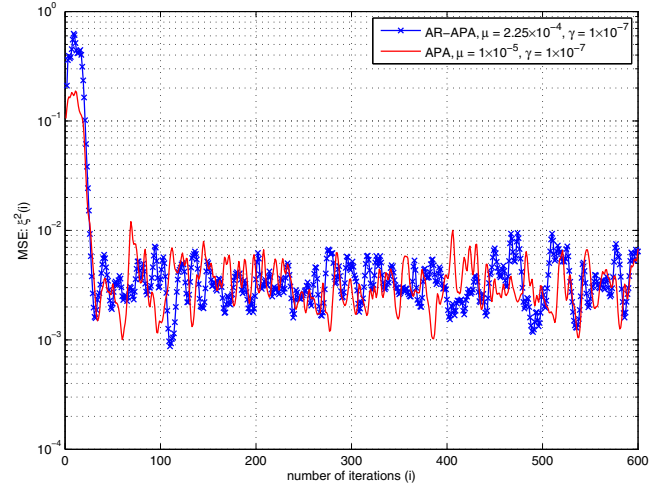


Fig. 6. Comparison of MSE for proposed AR-APA with $\mu = 2.25 \times 10^{-4}$, $\alpha = 1.15 \times 10^{-2}$, $\eta = 1.25 \times 10^{-4}$ and APA [1] with $\mu = 1 \times 10^{-5}$ and a zero-mean white noise sequence through AR(2,2) process, when SNR=20dB.

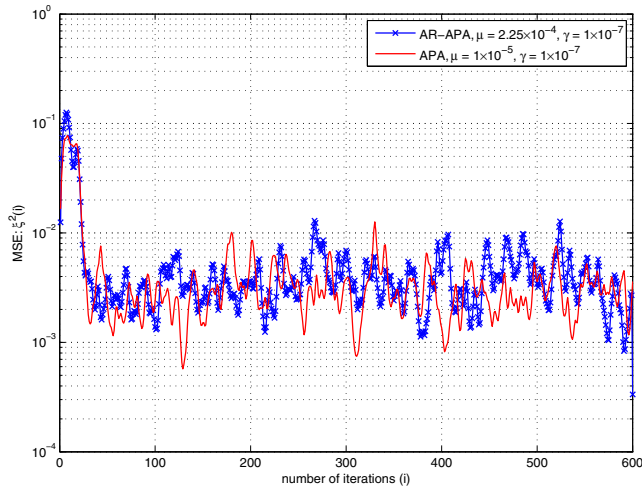


Fig. 5. Comparison of MSE for proposed AR-APA with $\mu = 2.25 \times 10^{-4}$, $\alpha = 1.15 \times 10^{-2}$, $\eta = 1.25 \times 10^{-4}$ and APA [1] with $\mu = 1 \times 10^{-5}$ and a zero-mean white noise sequence through AR(4) process, when SNR = 30dB.

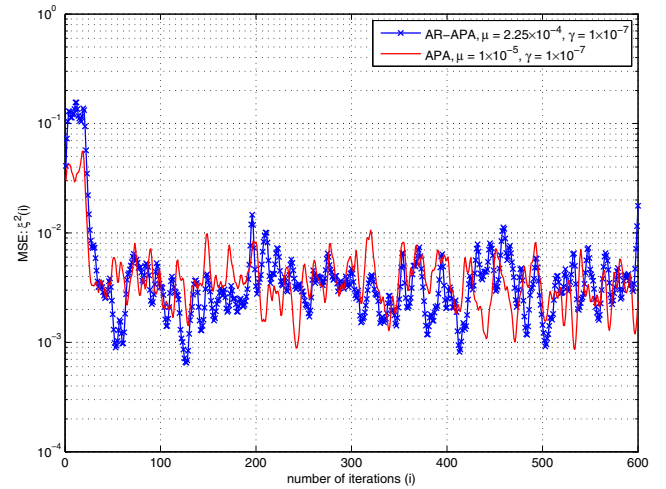


Fig. 7. Comparison of MSE for proposed AR-APA with $\mu = 2.25 \times 10^{-4}$, $\alpha = 1.15 \times 10^{-2}$, $\eta = 1.25 \times 10^{-4}$ and APA [1] with $\mu = 1 \times 10^{-5}$ and a zero-mean white noise sequence through AR(2,2) process, when SNR=30dB.

projection algorithm (APA) [1] using Gaussian and uniform white noise processes, or AR(3) process in low SNR at 20dB and high SNR at 30 dB.

The trajectories of MSE curves of proposed AR-APA and APA using Gaussian and uniform white noise processes at SNR = 20 and 30 dB and AR(4) process are shown in Fig. 4 and Fig. 5, respectively.

Fig. 6 and Fig. 7 show the trajectories of MSE curves of proposed adaptive reduced-rank affine projection algorithm and affine projection algorithm using Gaussian and uniform white noise processes in low SNR at 20dB and high SNR at 30dB and AR(2,2) process.

VII. CONCLUSIONS

In this paper, we have introduced a novel adaptive reduced-rank affine projection algorithm based on joint optimisation criterion. A reduced-rank scheme attempts to solve this limitation by reducing the number of adaptive coefficients of tap-weight vector. We have described how to derive the proposed adaptive reduced-rank affine projection algorithm with the method of complex Lagrange multipliers. Convergence analysis of proposed adaptive reduced-rank affine projection algorithm has introduced in terms of deviation vector between previous and present tap-weight estimated vectors under the assumptions and approximation. The pro-

posed adaptive reduced-rank affine projection algorithm can obtain the same performance compared with the conventional full-rank affine projection algorithm in the area of unknown channel estimation and system identification.

REFERENCES

- [1] P.S.R. Diniz, *Adaptive Filtering: Algorithms and Practical Implementation*, Springer, 2008.
- [2] S. Sitjongsataporn, *Advanced Adaptive DMT Equalisation: Algorithms and Implementation*, LAMBERT Academic Publishing, 2011.
- [3] M. Montazeri and P. Duhamel, "A Set of Algorithms Linking NLMS and Block RLS Algorithms", *IEEE Trans. on Signal Processing*, vol. 43, no. 2, pp. 444-453, 1995.
- [4] S. Werner, J.A. Apolinário, M.L.R. de Campos and P.S.R. Diniz, "Low-Complexity Constrained Affine-Projection Algorithms," *IEEE Trans. on Signal Processing*, vol. 53, no. 12, pp. 4545-4555, December 2005.
- [5] A.H. Sayed, *Fundamental of Adaptive Filtering*, Wiley, New York, USA, 2003.
- [6] Y.S. Choi, "Affine Projection Algorithm with Adaptive Error Constraint," *Electronics Letters*, vol. 48, no. 20, September 2012.
- [7] A.Gonzalez, M.Ferrer, F.Albu and M.de Diego, "Affine Projection Algorithms: Evolution to Smart and Fast algorithms and Applications," *European Signal Processing Conference (EUSIPCO)*, pp. 1965-1969, Aug. 2012.
- [8] S.Koike, "A Simplified Statistical Analysis of the Affine Projection Algorithm", *IEEE International Symposium on Intelligent Signal Processing and Communication Systems (ISPACS)*, pp. 565-569, Nov. 2015.
- [9] H.M.Hasanien and S.M. Muyeen, "Affine projection algorithm based adaptive control scheme for operation of variable-speed wind generator", *IET Generation, Transmission & Distribution*, vol. 9, issue 16, pp. 2611-2616, 2015.
- [10] S.Ciochina, C.Paleologu, J.Benesty and C.Anghel, "An Optimised Affine Projection Algorithm for Acoustic Echo Cancellation", *IEEE International Conference on Speech Technology and Human-Computer Dialogue (SpeD)*, Oct.2015.
- [11] R. Singh and L.B. Milstein, "Adaptive Interference Suppression for DS/CDMA," *IEEE Trans. Commun.*, vol. 50, no. 12, pp. 1902-1905, November 2002.
- [12] R.C. de Lamare, and R. Sampaio-Neto, "Adaptive Reduced-Rank MMSE Filtering with Interpolated FIR Filters and Adaptive Interpolators," *IEEE Signal Processing Letters*, vol. 12, no. 3, March 2005.
- [13] R.C. de Lamare, and R. Sampaio-Neto, "Reduced-Rank Adaptive Filtering Based on Joint Iterative Optimization of Adaptive Filter," *IEEE Signal Processing Letters*, vol. 14, no. 12, pp. 980-983, December 2007.
- [14] Parthaprati De, "Semi-Blind Sparse Channel Estimation Using Reduced Rank Filtering", *IEEE Transactions on Wireless Communications*, vol. 17, issue 3, pp. 1418 - 1431, 2018.
- [15] Q. Haoli and S.N. Batalama, "Data Record-based Criteria for the Selection of an Auxiliary Vector Estimator of the MMSE/MVDR Filter," *IEEE Transactions on Communications*, vol. 51, no. 10, pp. 1700-1708, October 2003.
- [16] S.Sitjongsataporn, "Adaptive Reduced-Rank Affine Projection Algorithm based on Joint Optimisation," *IEEE International Conference on Electrical Engineering/Electronics, Computer, Telecommunications and Information Technology (ECTI-CON)*, pp. 702-705, Jun. 2017.
- [17] M.H. Hayes, *Statistical Digital Signal Processing and Modeling*, John Wiley & Sons, 1996.
- [18] S. Haykin, *Adaptive Filter Theory*, Prentice Hall, 2001.

High Voltage - Pulse Electric Field of Microorganism Elimination

Sanya khunkhao, Aphichata Thongrak

Dept. of Elelectronics and Telecommunicaton
Engineering Rajamangala University of Technology
Phra Nakhon. Bangkok , Thailand.
Sanya.k@rmutp.ac.th, aphichata.t@rmutp.ac.th

Wanchai Chankaipol

Dept. of Electrical and Electronics Application Engineering
Sripatum University Bangkok , Thailand.
wanchai.ch@spu.ac.th

Abstract—The antimicrobial agent with high-voltage pulse electric field to eliminate microorganisms contained in the liquid is composed of water to disrupt cell membranes. Furthermore, the destruction of the cell membrane voltage and plum with 2-pole electrode polarity stacking in period of about 10 ns to 20μs. The voltage drop across the membrane are increasing, cause a small a lot more porous membrane of cell walls of microorganisms can be destroyed. For this reason, it is defined as a condition circuit that controls the frequency and pulse width to control high voltage output to the terminal electrodes. The high voltage direct current electric field causes a highly stable voltage range of 20-30 kV/cm, which can inhibit the growth of microbes as well. The results of the test liquid samples with a natural water. The level of stimulation at high voltage DC power at 45-50 volts, with a frequency of 20 kHz and a pulse width of 10%, 15%, and 25% were found to eliminate microorganisms. The test panels with 3M Perry's family film for the change in the number of infections that occur before and after the test has decreased significantly. The result of using a high-voltage pulse electric field which can be eliminated bacteria and tested with a sheet 3 M Petrifilm™ is finding a volume change of the number of infections that occur before and after the test has decreased significantly.

Keywords— pulse electric field, microorganisms, Duty Cycle, porous membrane

I. INTRODUCTION

The application of high voltage electric field pulses has played a significant role in human life, such as medicine, genetics and food preservation. The high voltage electric field pulse is a non-thermal process that can be performed at room temperature and is also very fast. Moreover, it can maintain the freshness and quality of food better than the sterilization process with liquid food, which causes the loss of nutrient quality. To study the inhibition of microbial growth by studying circuit design and test kit assembly with liquid sample with water composition. The electric field pulses under high voltage direct current into the sample to inhibit the growth of microorganisms by causing the cell wall to be destroyed as porous. The characteristics of the cell before pulse are used. The voltage potential of the membrane is given by the equation (1).

$$V_{cell} = fr_{cell}E_{cell} \quad (1)$$

where

V_{cell} : is the maximum voltage that drops across the membrane

f : is the constant value that depends on the shape of the cell

r_{cell} : is the Outer radius of the membrane

E_{cell} : is the electric field stress on the membrane

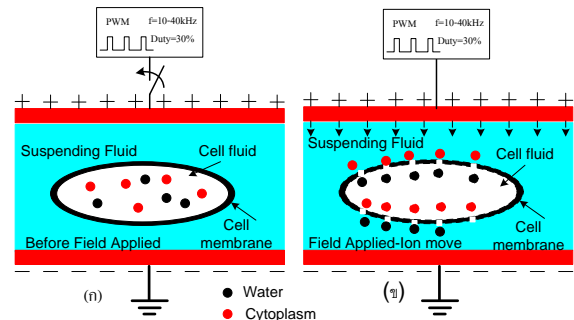


Fig.1. Structure of cell before and after pulse of high voltage electric field.

While the membrane is porous, it results in fluid transfer between the outside of the cell and the cytoplasm inside the cell as shown in Figure 1, resulting in increased cell growth[1]. The breakdown of the membrane due to the electric field stresses that the pore occurs must be large enough to lead of cell death[2]. The electric field pulses for killing microbes can be described by equation:

$$E_{cell} = \frac{V}{d} \quad (2)$$

where

E_{cell} : is the electric field stress on the cell membrane

V : is the voltage applied to the electrode

d : is the distance between electrodes.

I. DESIGN CIRCUIT FOR HIGH-FREQUENCY AND HIGH VOLTAGE PULSE ELECTRIC FIELD

The switching circuit design is a switching power source that can control pulse width frequency. The switching circuits are in the form of integrated circuits, using the voltage control mode. The design of pulse width modulation circuit with TL494 as shown in Figure 2. The internal circuit of the IC has adopted

the principle of control mode from the voltage applied to the return of the output voltage.

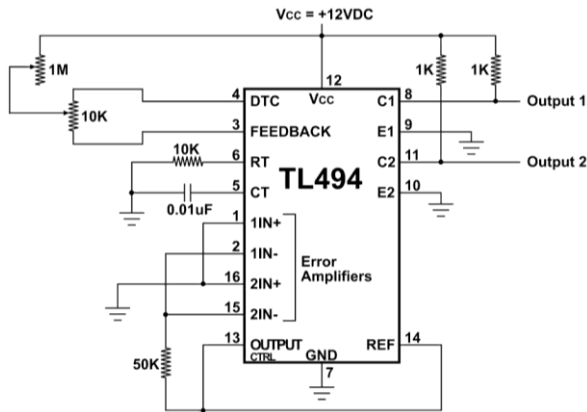


Fig.2. Schematics of PWM Pulse Generator Circuit.

The DC voltage activates the high-frequency transformer with an opto-isolated protection circuit to isolate the ground of the PWM circuit as shown in Figure 3. Out of the ground of the electronic control circuit, the power is removed from each other to prevent short circuits. By comparison with the voltage reference to the output voltage from the PWM circuit, it is characterized as a square pulse[3]. There is a constant period equal to the sawtooth momentum and is the width of the modulation of the input voltage to the PWM. In circuit use device IGBT is a high voltage and current resistant device. Also, it works well in larger areas when the switch time is the same as shown in Figure 4.

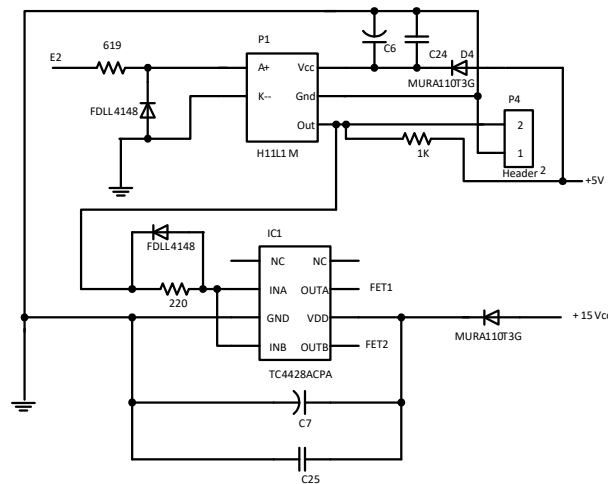


Fig.3. Schematics of Opto-isolated Circuit.

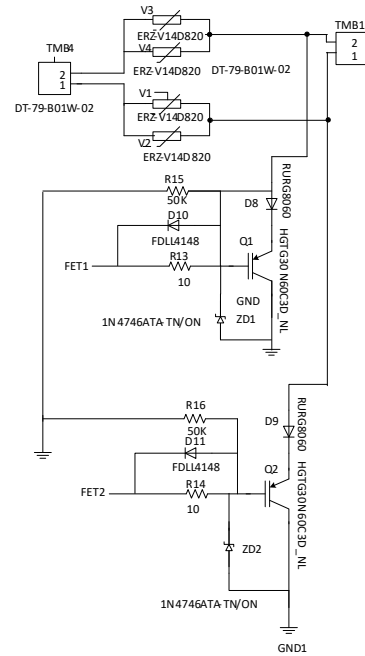


Fig.4. Schematics of power IGBT drive Circuit.

II. OSCILLATOR CIRCUIT

This pulse width modulator (PWM) is set to operate at 20 kHz. The frequency can be selected for more. Therefore, the frequency can select the value of capacitor C_T and resistance R_T as shown in Figure 5. The oscillator frequency equals to output frequency only for single-ended applications. For push-pull applications, the output frequency is one-half the oscillator frequency.

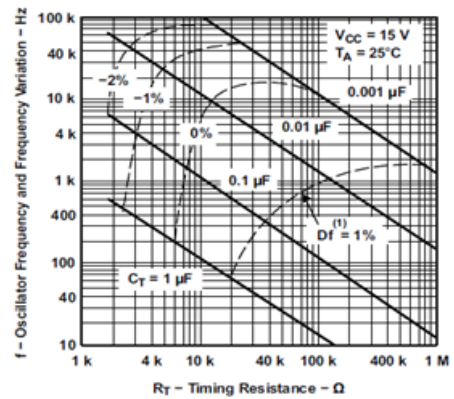


Fig.5. Oscillator Frequency and Frequency Variation vs Timing Resistance.

The oscillator is set to operate at 20 kHz, using the component values calculated by Eq. (3) and Eq.(4). The frequency of the oscillator becomes

$$f_{ocs} = \frac{1.1}{R_T C_T} \quad (3)$$

Where

R_T : is the external timing resistor

C_T : is the external timing capacitor = 0.01 μ F

f_{osc} : is the oscillator frequency.

$$R_T = \frac{1.1}{20 \times 10^3 \times 0.01 \times 10^{-6}} = 2.2k\Omega \quad (4)$$

Figure 6 shows the PWM output signal of TL 494 that can be adjusted for Duty Cycle and different frequency modulation with V_{R3} resistance. The PWM output signal needs to be adjusted for the duty cycle of the IGBT. This will make adjustments at the levels of 10%, 15% and 25% as shown in Figure 7. The duty cycle adjustment at these levels is to reduce the power of electronic devices that are capable of controlling the current flowing through the primary coil of the transformer. A fly back converter that generates sufficient flow of energy will result in a magnetic field induced by secondary windings with high voltages sufficient to kill the microbes.



Fig.6. Schematics of the PWM Controls circuit board.

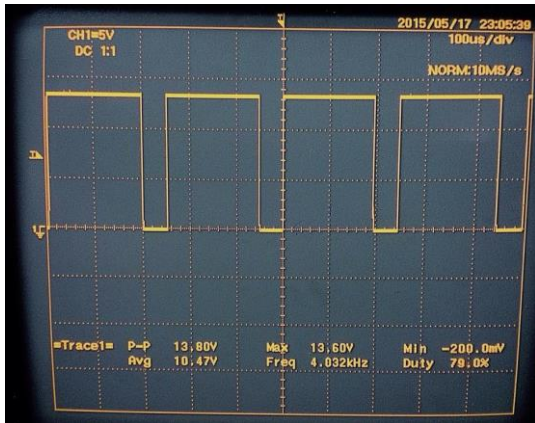


Fig.7. Signal from the PWM generator.

III. HIGH FREQUENCY TRANSFORMER DESIGN

A DC-DC converter that provides isolation between input and output is the flyback circuit which it's in fact an inductor with primary and secondary windings. The high frequency transformer acts as an inductor and increases the output voltage which the transformer rating has primary voltage: $V_p = 50$ V, and second voltage: $V_{out} = 19-30$ kV, $f = 50$ kHz, the cross section area (A_i) = 8.32 cm². The total time of 66µs at 50% is 33µs using the EE65 axis. The area of the cross section of core is $A_e = 5.33$ cm². Use a U-

axis or C-axis ferrite transformer to calculate the primary and secondary coils of coils, as shown in Figure 8. Calculate the circumference of the primary coil from the equation.

$$N_p = \frac{V_p \times 10^8}{4B_{max} f A_i} = \frac{50 \times 10^8}{4 \times 5000 \times 50 \times 10^3 \times 8.32} = 1 \text{ turn}$$

Therefore, the primary wire must be welded (number of turns / Voltage)x50 = 50 turn. For calculating the circumference of the secondary coil is determined by the formula:

$$\frac{N_s}{N_p} = \frac{V_p}{V_s} = \frac{I_p}{I_s};$$

$$N_s = \frac{V_p}{V_s} \times N_p = \frac{40 \times 10^3}{50} \times 1 = 800 \text{ turn}$$

As describe, the size of the inductance coil used for the secondary transformer at frequency 50kHz is AWG # 23.



Fig.8. Fly back transformer

IV. PROCEDURAL FOR EXPERIMENTAL

High voltage electric field tests are performed by pulse generator circuits. For driving the transformer at the polarity of two polarized electrodes, anode and cathode. In addition, the microbial in liquid and natural waters was tested with a 20 kHz frequency test at Duty Cycle 10%, 15% and 25%, respectively as shown in Figure 9. As well as the vacuum from the inside, the vacuum pressure is equal to zero Pascal. Then slightly aerate the gas to produce a thin atmosphere of nitrogen gas, which is a high voltage electric field pulse, causing the gas to dissolve into plasma atmosphere. By adjusting the input voltage from 10-50 volts, the values shown in Table. 1.

Take the liquid test specimen inside the vacuum chamber for test measurement at frequency 20 kHz and Duty Cycle at a 10% which increases the output voltage and the current flowing through the wire is very high, as shown in Figure 10.

Table 1: Test measurement of liquid natural water at 20 kHz with Duty cycle 10%, 15% and 25%

Vin (V)	Duty cycle					
	10%		15%		25%	
	Vout (kV)	Iout (mA)	Vout (kV)	Iout (mA)	Vout (kV)	Iout (mA)
10	10.13	100	19.5	100	19.86	100
20	22.03	300	24.17	500	23.16	500
30	26.16	500	28.2	500	26.31	500
40	27.22	600	29.26	600	28.39	600
50	28.1	700	30.12	650	29.12	700

The plasma at the high intensity electric field is expressed in purple at the glass Pyrex between the two electrodes, as shown in Figure 10.

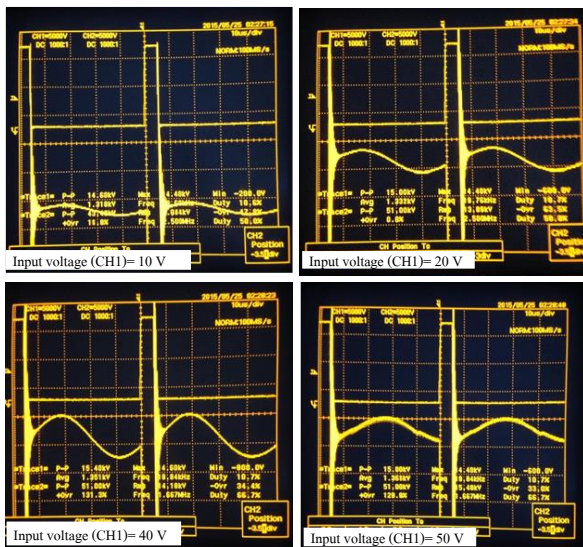


Fig.9. (a) PWM signal at 20 kHz, Duty 10%, CH I input level 10-50V and CH II output signal.

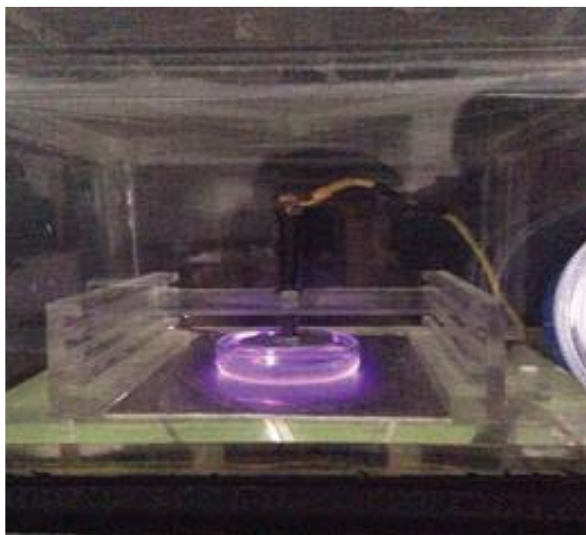


Fig.10. Plasma generation during testing with fluid samples.

A. Test measurement

Sampling with 3M Petrifilm-E. Count Plate as shown in Figure 11 with natural water has the following sequence of tests:

1) Take 1 ml of the liquid test specimen from natural water drop onto the test plate before disinfection at an electric field, then incubated at a temperature of about 32-35 ° C for one day and then read the results as shown in Figure 12.



Fig.11. (a) 3M Petrifilm-E.coli Count Plate Sheet and Liquid droplet test.



Fig.12. Number of microorganisms from the test sample before applied high electric field.

2) Take the same natural water through Electroporation or Plasma Disposal at 20 kHz and 15% Duty and 25% for 5 minutes and 10 minutes respectively. Then, test with 3M Petrifilm-E.coli Count Plate with droplets on 1 ml test plate, then incubated for 1 day and then 3M plates passed before and after treatment. As shown in Figures 13 and 14.

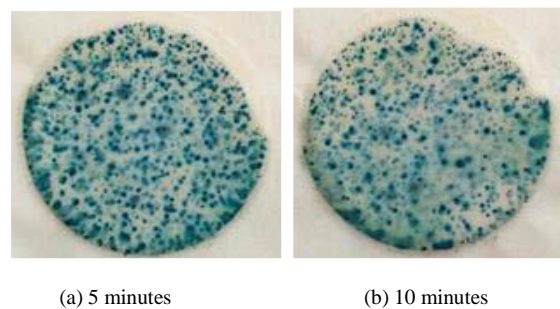


Fig.13. Number of microorganisms tested at 20 kHz Duty Cycle 15% for 5 and 10 minutes.

By counting points on test sample under effective of high intensity field as shown in Figure 15 as follows.

1) Test results at 20 kHz, 15% Duty Cycle at 5 minutes and 10 minutes were displayed on 3M Petrifilm-E.coli Count Plate as shown in Figures 13 (a) and (b), respectively. After passing the test 5 minutes by natural water the Microbial counts are approximately $21 \times 30 = 630$ Colonies Per Plate and 10 minutes after the test. Microbial counts are approximately $15 \times 30 = 450$ Colonies Per Plate.

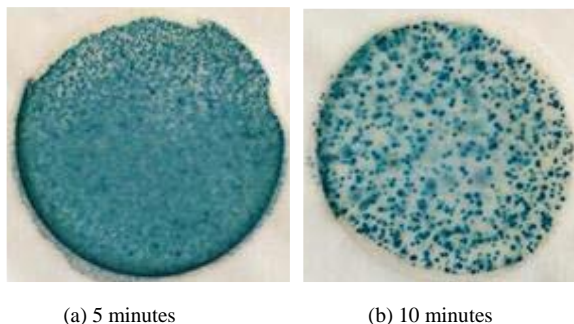


Fig.14. Number of microorganisms tested at 20 kHz and Duty Cycle 25% for 5 and 10 minutes.

2) Test results at 20 kHz, 25% Duty Cycle in 5 minutes and 10 minutes on 3M Petrifilm-E.coli Count Plate is shown in Figure 14 (a) and (b), respectively. After applied the high intensity electric field test passed 5 minutes, using national water, it was found that the microbial counts were not due to excessive amount. After 10 minutes of testing Microbial counts are approximately $23 \times 30 = 690$ Colonies Per Plate.

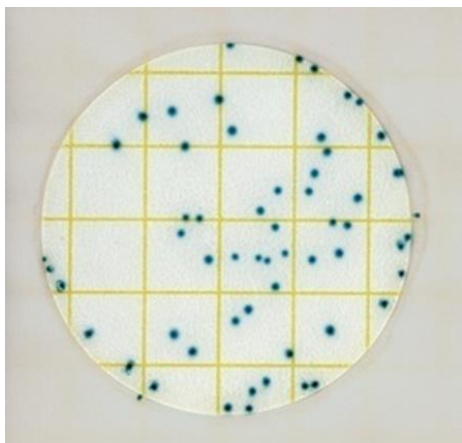


Fig.15 Show microorganisms after incubation and the number of Corona is based on a square test.

An applied of high voltage pulse electric field has been effected with the liquid natural water, It was found that, the best performance change is at approximately 20 kHz at a 25% duty cycle with a DC input of approximately 50V_{DC}. The test results for 5 minutes and 10 minutes to find differences in the number of colonies that were stored in the same place for 24 hours. It was found that the 3M Petri-film

E.coli Count Plate showed significant decrease in microbial counts under high intensity electric field for a period of time as shown in Figure 16.

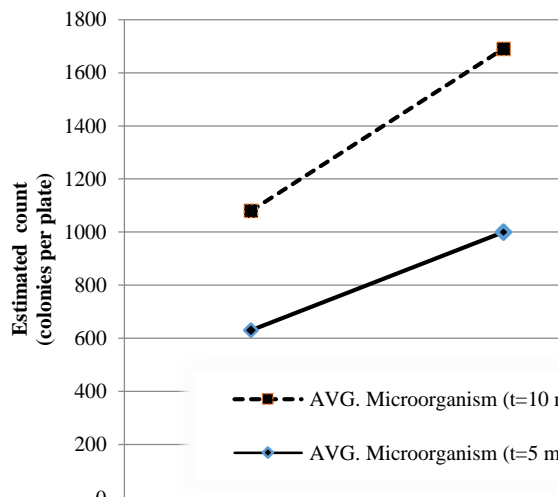


Fig.15. Show the number of microorganisms tested at the Duty cycle (%) versus the time of the test.

CONCLUSION

Experimenting the use of high-voltage field pulses for microbial testing showed that the change in the colonies was reduced. The best test results will be at approximately 20kHz at a duty cycle of 25% with a voltage of about 50VDC. Over time, the difference in the number of tested and untested colonies stored in the ambient air temperature was significantly reduced by experimenting with 3M Petri-film E.coli Count Plate. This test can be used to test the number of microorganisms that pass through the plasma at high pressure for a specified period of time.

ACKNOWLEDGMENT

The authors thank the Prof.Dr.Kazunori Sato for advice and recommend gratefully acknowledged.

REFERENCES

- [1] H. Hulsheger, J. Potel, and E.G. Niemann, "Killing of bacteria with electric pulses of high field strength," *Radiat. Environ. Biophys*, vol.20, pp. 53-65, 1981.
- [2] H. Vega-Mercado, U.R. Pothakamury, F.J. Chang, G.V. Barbosacanovas, and B.G. Swanson, "Inactivation of Escherichiu coli by combining pH, ionic strength and pulsed field strength," *Radiat. Environ. Biophys*, vol.20, pp. 53-65, 1981.
- [3] V. Heinz, S. Toepfl, D. Knorr, "Impact of temperature on lethality and energy efficiency of apple juice pasteurization by pulsed electric fields treatment," *Innovative Food Science and Emerging Technologies*, vol. 4, no. 2, pp. 167- 175, 2003.
- [4] Jayaram, Shesha H. "Sterilization of Liquid Foods by Pulsed Electric Fields," *Electrical Insulation Magazine*, vol. 6, pp. 17-25, 2000.

IEET Editorial Office

EAAAT - Electrical Engineering Academic Association (Thailand)
Room 409, F-Building
140 Cheum-Sampan Rd.
Nong Chok, Bangkok, Thailand 10530
Tel: +662-988-3655 ext 2216 Fax: +662-988-4026

www.journal.eaat.or.th

